I

STOPPING CROSS SECTION ADDITIVITY FOR 0-2 MeV ^{4}He IONS IN SOLIDS

II

MAGNETITE THIN FILMS: FABRICATION AND ELECTRICAL PROPERTIES

Thesis by

Joseph Shao-Ying Feng

In Partial Fulfillment of the Requirements

for the Degree of

Doctor of Philosophy

California Institute of Technology

Pasadena, California

1975

(Submitted September 12, 1974)

ACKNOWLEDGMENTS

I wish to express my gratitude and profound appreciation to Professors Marc-Aurele Nicolet and James W. Mayer for their patience and understanding during the course of this work. Their thoughtfully tempered supervision and scrupulous and conscientious criticism of my work provided me with the ideal environment for executing my research.

I am also deeply indebted to Professors Floyd Humphrey and Charles Wilts for allowing me unlimited access to their laboratory facilities. Much of the work presented here would have been difficult, if not impossible, had it not been for their generosity. I would also like to thank Professor Charles Barnes and the Kellogg Radiation Laboratory for guidance and access to the Kellogg 3 MV van de Graaf. I also thank Professor Jesse Beauchamp for permitting me the use of his electromagnet.

I would like to thank Dr. Wei-Kan Chu for his contributions to my understanding of the problem of the energy loss of charged particles in matter and for his collaboration in the Bragg-rule studies. I also thank Dr. Christopher Bajorek for stimulating my interest in magnetite and for his continuing support in these investigations. Thanks go to Dr. Richard Pashley for several stimulating discussions and for his collaboration in the galvanomagnetic investigations in Fe_3O_4. Much of this work was raised to the level of scientific respectability through discussions on magnetics and magnetic materials with Professors Wilts and Humphrey and in discussions on the electrical transport properties of semiconductors with Professor Thomas McGill.

Special thanks go to Mrs. Karen B. Current, Mrs. Kathleen M. Ellison and Mrs. Carol Norris. In addition to providing excellent secretarial work, they are treasured friends who have shown me great kindness during my association with the Electrical Engineering Department.

Thanks are also due to Mr. Rob Gorris and Mr. Don McGrath. In addition to continually providing valuable technical assistance, they are also responsible for having provided a significant part of my practical laboratory training.

The financial assistance of the National Science Foundation Traineeships, both at the California Institute of Technology and at Northwestern University, is gratefully acknowledged. I am also indebted to the Institute and the Electrical Engineering Department for providing me with a priceless educational experience and financial support in the form of several teaching assistantships and the concomitant tuition waivers. The work reported here was supported in part by the Office of Naval Research, the NASA Langley Research Center, and the Hoegsted Phim Memorial Fund.

Finally, I would like to express my appreciation to the Executive Officer for Electrical Engineering for this opportunity to improve my typing proficiency. The courageous way in which he informed the students of the impending implementation of this new policy on the typing of theses is to be universally admired and commended. The timing is especially noteworthy. Not only had I just successfully solicited a donation of about $3000 worth of electronic parts for the department's instruction program, but there were also two other students from the

the same group who were also in the midst of having their theses prepared. A casual observer might suspect some personal motivations for this excellent timing, but I believe that all this circumstantial evidence is not sufficient to be unimpeachably convincing. At any rate, in these days of women's liberation, my typing proficiency may prove to be the only marketable skill that the Electrical Engineering Department has been able to bestow upon me.

Inasmuch as this manuscript was prepared by the best typist I know(myself), every effort has been made to make this dissertation as mercifully brief as possible.

ABSTRACT

Part I

Rutherford backscattering can be used to determine the depth distribution of the constituent elements in the first micron of a sample. The interpretation of the spectra requires an accurate knowledge of the rate at which the probe ions lose their kinetic energy. The microscopic rate of energy loss, the stopping cross section, has been fairly intensively investigated, both experimentally and theoretically, in elemental targets.

In 1905, Bragg and Kleeman proposed that the rate of energy loss in a compound is a linear superposition of the atomic stopping powers. Because of the experimental difficulties, the uncertainties in the tests of this assumption have been 5-10%. Within the sensitivities of these experiments, Bragg's rule has usually been reported to be valid at high ion velocities($E \gtrsim 1$ MeV/amu). We describe two new methods of testing Bragg's rule in which the apparent sensitivity limit is below 1%.

The first test requires that Bragg's rule be extended in the obvious way to include alloys and non-stoichiometric compounds. This experiment requires a multi-layered sample in which the components of these layers can somehow be redistributed. If there is no chemical interaction with the ambient, including the substrate, the total energy loss in this multi-layered structure should be independent of the distribution of the constituent elements. This test was applied to two-layered structures of Au-Ag, Au-Cu, Au-Al, and their alloys or compounds. The total energy loss before and after the two layers were

mixed was reproducible to within 1%, as predicted by Bragg's rule.

The second test is particularly useful in those targets in which one of the component elements(or chemical radicals) is not readily available as a separate layer. Some examples that were included in this experiment are the oxides, SiO_2 and Al_2O_3. The analytical procedure required that three assumptions in addition to Bragg's rule be invoked. When this procedure was applied to MgO, SiO_2, Al_2O_3, Fe_2O_3 and Fe_3O_4, it was possible to demonstrate that there is a unique contribution by oxygen to the molecular stopping cross sections of these compounds. However, this value is apparently 6-22% lower than the value expected from the measured stopping cross section of molecular O_2 in the gas phase.

Part II

A low-temperature process for manufacturing magnetite(Fe_3O_4) thin films by converting hematite(α-Fe_2O_3) thin films is described. The films produced are unambiguously identified as magnetite.

Resistivity, dc Hall effect and transverse magnetoresistance measurements were performed on these films from 104°K to room temperature. The Verwey transition is observed at 123°K, about 4°K higher than reported for stoichiometric bulk magnetite. The ordinary and extraordinary Hall coefficients are both negative over the entire temperature range, consistent with negatively charged carriers. The extraordinary Hall coefficient exhibits a $\rho^{1/3}$ dependence on the resistivity above T_V and a $\rho^{2/3}$ dependence below T_V. The magnetoresistance is negative at all temperatures and field strengths and its magnitude increases monotonically with the magnetic field at all temperatures.

The planar Hall effect signal was below the sensitivity of the present experiment.

One particular anomalous result observed in these measurements is the elevated Verwey transition temperature. To account for this unusual behavior, the Verwey transition in magnetite thin films was investigated by measuring the temperature dependence of the sheet resistivity. It was demonstrated that substrate-induced stresses are responsible for the elevated Verwey transition temperature. The ratio of the resistances in the two states, as evaluated at the transition temperature, is apparently proportional to the thickness of the film and independent of the substrate. The combination of these two results suggests that there is a 600-1200 Å layer that remains in the high conductivity state at all temperatures and that it is probably at the free surface of the magnetite film.

TABLE OF CONTENTS

	Page
Acknowledgments	ii
Abstract	v
Table of Contents	viii
PART I: STOPPING CROSS SECTION ADDITIVITY FOR 0-2 MeV ^{4}He IONS IN SOLIDS	1
Chapter 1 Introduction	2
References to Chapter 1	7
Chapter 2 Bragg's Rule in Binary Alloys	9
2.1 Introduction	9
2.2 Formulas for Applying Bragg's Rule	10
2.3 Concepts and Calculations	13
2.4 Experimental Procedure	26
2.5 Experimental Results	30
2.6 Discussion	39
References to Chapter 2	41
Chapter 3 Stoichiometric Compounds	42
3.1 Introduction	42
3.2 Basic Concepts(Thick Target Yield Formulas)	44
3.3 Two-Layered Structures (corrections to the formulas in 3.2)	49
3.4 Bragg's Rule in Solid Compounds	72
3.5 Discussion	105
References to Chapter 3	113

Chapter 4 Summary 116

Appendix A A Computer Program to Simulate Backscattering Spectra 118

A.1 General Description 118

A.2 Using the Program 120

A.3 Listing of the Program 126

A.4 Example of a DATA Deck 151

Appendix B Measurements of the Absolute Energy Loss in Fe and Al 158

B.1 Thickness Measurements 158

B.2 Results and Discussion 159

References to Appendix B 166

PART II: MAGNETITE THIN FILMS: FABRICATION AND ELECTRICAL PROPERTIES 167

Chapter 1 Introduction 168

References to Chapter 1 175

Chapter 2 Making the Films 176

2.1 Introduction 176

2.2 The Manufacturing Process 178

2.3 Evidence for Magnetite Formation 182

References to Chapter 1 189

Chapter 3 Galvanomagnetic Properties 190

3.1 Introduction 190

3.2 Results 192

Preprint: "Magnetoelectric Properties of Magnetite Thin Films" 193

3.3 Additional Discussion 225

Additional References to Chapter 3 228

Chapter 4 The Verwey Transition in Thin Films 229

4.1 Introduction 229

4.2 Results 231

Preprint: "Substrate Effects on Magnetite Thin Films" 232

4.3 Additional Discussion 248

Additional References to Chapter 4 250

Chapter 5 Summary 251

PART I

STOPPING CROSS SECTION ADDITIVITY FOR 0-2 MeV ^{4}He IONS IN SOLIDS

Chapter I

INTRODUCTION

In recent years, much effort has been expended in studying the motion of energetic charged particles into the first few surface micrometers of a solid target. One particularly fruitful application has been the development of Rutherford backscattering of MeV helium ions to study the atomic composition in those first few microns. Encouraged by the availability of low energy accelerators and the associated instrumentation, a hardy band of solid state experimentalists has actively applied this powerful new tool to a host of modern technological problems. The impact of the development of this new analytical technique and the rapidity with which this field has advanced can be gauged by the large number of recent review articles on the application of nuclear techniques to solid state problems(Gyulai et al, 1970; Gyulai et al, 1971; Mayer and Phim, 1971; Mayer, 1972; Nicolet et al, 1972; Chu et al, 1973a; Chu et al, 1973b; Mayer and Turos, 1973; Mayer, 1973a; Mayer, 1973b; Nicolet and Mayer, 1973; Nicolet and Mayer, 1974; Mayer and Tu, 1974; and Mackintosh, 1974).

One of the unique features of α-particle backscattering is that it provides a non-destructive measurement of the depth distribution of the different constituent elements. This depth perception is a result of the energy lost by the probe ion as it penetrates the sample. The conversion from the amount of energy lost by the particle, the experimentally measured quantity, to the corresponding depth in the target implies the rate of energy loss is known. This parameter has been exten-

sively characterized both experimentally and theoretically for the pure elements(for an extended discussion, see Ziegler and Chu, 1973). However, some of the most interesting applications of backscattering involve targets of intermediate compositions such as alloys or compounds. The energy loss in these targets has almost always been estimated by applying linear superposition, or Bragg's rule, to the rates in the constituent elements.

This assumption was first made by Bragg and Kleeman(1905) during their studies of the range of natural α-particles. Since knowing the amount of energy deposited in organic material, such as a human being, by a radioactive decay particle is important in the fields of radiation safety and health physics, the validity of this rule has been most extensively investigated in range-energy studies of natural α-particles in air, water, and several organic compounds(the most complete recent compilation of these experiments are listed as references 2-16 in Bourland and Powers, 1971). The most precise experiments for 0-2 MeV ^{4}He ions have been those performed by the Baylor University(Waco, Texas) group in their measurements of the atomic and molecular stopping cross sections of several gases(Bourland, Chu and Powers, 1971; Bourland and Powers, 1971; and Powers et al, 1972).

Despite the availability of solid targets, there exist few reports of tests of Bragg's rule in solids. Those that do exist usually apply either to protons or higher energy α-particles. In general, no serious violations of Bragg's rule, within the sensitivity of the experiments, were observed. One recent exception has been an apparent departure from Bragg's rule in SiO_2 that was reported by Thompson and Mackintosh(1971).

In attempting to perform a Bragg-rule experiment, it appears that a measurement of the differential energy loss should be more sensitive than attempting to measure the 10-100 μm range of an MeV α-particle in a solid. The accuracy of a differential measurement is usually limited by the errors inherent in determining the thickness of the target. In this energy range, convenient targets are typically 100-500 $\mu g/cm^2$ thick and the random errors in almost any measurement of the thickness will be about 3-5%(see Chu and Powers, 1969). The sensitivity of a Bragg-rule experiment that utilized this approach would be limited to 5-8%. In contrast, the reported precision of an energy loss measurement in a gas is typically about 1%(see Bourland, Chu and Powers, 1971).

The discussion of sensitivity raises the question of whether or not Bragg's rule should be valid, and how large the deviations will be if it is not applicable. One possible answer is that it depends on the particle velocity. At these energies, the stopping is almost entirely due to interactions with the electrons in the stopping medium. At extremely high, but non-relativistic, velocities, the electrons appear to the ion as a plasma and Bragg's rule should be obeyed. At very low velocities, the ion-electron interactions are affected significantly by the details of the electronic states since the valence shell electrons contribute a larger fraction of the stopping than at high velocities. Since the valence electrons are those most significantly affected by any chemical or physical changes, deviations from Bragg's rule would be expected to be largest at low energies. The magnitude of these deviations has been estimated to be as high as 30%(Brynjolfsson, 1973; Ziegler, Chu, and Feng, unpublished).

High energy α-particle backscattering is usually performed with incident energies of 1-2 MeV; the detected particle energies can be as low as 0.3 MeV. This just spans the transition between the high and low velocity regimes described above. In measurements on gaseous hydrocarbons over the same velocity range, chemical binding and physical state effects up to 5% have been observed using both protons and helium ions (Jorgensen, 1958; Bourland and Powers, 1971). The present study was undertaken to test the validity of Bragg's rule in solid targets over this same energy range and to improve on the sensitivity of the previous tests. A particularly elegant test is described in Chapter 2 in which the fundamental limit of the sensitivity is believed to be below 0.1%. A more circuitous approach, that is used when the method of Chapter 2 is inapplicable, is described in Chapter 3. The sensitivity of this second test is at least 1% and it may be even better.

This work has been described previously in a number of publications. These include:

"Relative Measurements of Stopping Cross Section Factors by Back-Scattering," J. S.-Y. Feng, W. K. Chu, M-A. Nicolet and J. W. Mayer, 1973, Thin Solid Films, vol. 19, p. 195.

"Bragg's Rule Study in Binary Metal Alloys and Metal Oxides for MeV $^4He^+$ Ions," J. S.-Y. Feng, W. K. Chu and M-A. Nicolet, 1973, Thin Solid Films, vol. 19, p. 227.

"Stopping Cross Section Additivity for 1-2 MeV $^4He^+$ in Solid Oxides," J. S.-Y. Feng, W. K. Chu and M-A. Nicolet, 1974, to be published in the Physical Review B, November 1974.

The results of a related experiment, stimulated by an inconsistency in

the present results, may be found in Appendix B. It has been submitted in part for publication as:

"Energy Loss of 0.3-2.0 MeV ^{4}He Ions in Aluminum," J. S.-Y. Feng, submitted to the Communications of the Journal of Applied Physics.

The results of a totally unrelated experiment that will not be reported here can be found in:

"Iron Silicide Thin Film Formation at Low Temperatures," S. S. Lau, J. S.-Y. Feng, J. O. Olowolafe and M-A. Nicolet, 1974, presented at the International Conference on Low Temperature Diffusion and Application to Thin Films, Yorktown Heights, New York, 12-14 August 1974.

Finally, at the time of this writing, there is a manuscript in preparation. This discusses the theoretical origins of physical state effect and estimates the magnitude of this effect for MeV helium ions from theoretical and experimental considerations. The contribution of the present author to this work is limited to having provided the experimental supporting evidence for this effect. This is being cited in this manuscript as J. F. Ziegler, W. K. Chu and J. S.-Y. Feng, 1974, unpublished. It is the intention of the first two authors to submit the manuscript to the Physical Review Letters.

REFERENCES

Chapter I

N. Bohr, 1948, Kgl. Danske Videnskab Selskab Mat.-Fys. Medd., vol. 18, no. 8.

P. D. Bourland, W. K. Chu and D. Powers, 1971, Phys. Rev. B, vol. 3, p. 3625.

P. D. Bourland and D. Powers, 1971, Phys. Rev. B, vol. 3, p. 3635.

W. H. Bragg and R. Kleeman, 1905, Phil. Mag, vol. 10, p. S 318.

Ari Brynjolfsson, 1973, thesis, The Niels Bohr Institute, Kϕbenhavns universitet(unpublished).

W. K. Chu, J. W. Mayer, M-A. Nicolet, T. M. Buck, G. Amsel and F. H. Eisen, 1973a, Semiconductor Silicon 1973(Princeton) p. 416.

W. K. Chu, J. W. Mayer, M-A. Nicolet, T. M. Buck, G. Amsel and F. H. Eisen, 1973b, Thin Solid Films, vol. 17, p. 1.

W. K. Chu and D. Powers, 1969, Phys. Rev., vol. 187, p. 478.

J. Gyulai, I. V. Mitchell, J. W. Mayer and V. Rodriguez, 1970, Proceedings of the International Conference on the Physics and Chemistry of Semiconductor Heterojunctions and Layered Structures, Budapest, Hungary.

J. Gyulai, I. V. Mitchell and J. W. Mayer, 1971, Proceedings of the International Conference on the Physics and Chemistry of Semiconductor Heterojunctions and Layered Structures, Budapest, Hungary.

Theodore Jorgensen, 1958, National Academy of Sciences-National Research Council Publication 752, page 20.

W. D. Mackintosh, 1974, Characterization of Solid Surfaces(Plenum Press), P. F. Kane and G. B. Larrabee, editors(still in press at the time of this writing).

J. W. Mayer, 1972, Radiation Effects, vol. 12, p. 183.

J. W. Mayer, 1973a, Proceedings of the International Conference on Applications of Ion Beams to Metals(Plenum Press), p. 141.

J. W. Mayer, 1973b, Channeling(Wiley), Chapter XVI, p. 453.

J. W. Mayer and H. Phim, 1971, Ion Implantation in Semiconductors (Japanese Society for the Promotion of Science), p. 137.

J. W. Mayer and K. N. Tu, 1974, J. Vac. Sci. Technol., vol. 11, p. 86.

J. W. Mayer and A. Turos, 1973, Thin Solid Films, vol. 19, p. 1.

M-A. Nicolet and J. W. Mayer, 1973, Proceedings of the Workshop on Photovoltaic Conversion of Solar Energy for Terrestrial Applications.

M-A. Nicolet and J. W. Mayer, 1974, Proceedings of the Symposium on the Materials Science Aspects of Thin Films for Solar Energy Conversion.

M-A. Nicolet, I. V. Mitchell and J. W. Mayer, 1972, Science, vol. 177, p. 841.

D. Powers, W. K. Chu, R. J. Robinson and A. Lodhi, 1972, Phys. Rev. A, vol. 6, p. 1425.

D. A. Thompson and W. D. Mackintosh, 1971, J. Appl. Phys., vol. 42, p. 3969.

J. F. Ziegler and W. K. Chu, 1973, IBM Research Report RC4288(#19193).

J. F. Ziegler, W. K. Chu and J. S.-Y. Feng, 1974, unpublished.

Chapter 2

BRAGG'S RULE IN BINARY ALLOYS

2.1 Introduction

Ion backscattering is particularly well-suited for determining the atomic composition of the first few surface micrometers. One of the most common examples of the use of MeV helium ions has been to study the metallurgical reactions between two thin films or between a thin film and its substrate(see, for example, Bower, 1973).

Since the rate at which energetic helium ions dissipate their kinetic energy in an elemental medium is an intensively studied topic, the conversion of the scattered particle energy to the corresponding depth is straightforward when the sample contains only one element. The extension to the case of laminar layers of single elements is only slightly more difficult. Once the contents of the layers begin intermixing, the conversion from energy to depth assumes that the stopping power and the density of the mixture are also known. Although Bragg's rule has traditionally been considered applicable only to stoichiometric compounds(see, for example, Bourland and Powers(1971) where this is implicitly assumed), a natural and useful extension would be to apply the concept of linear additivity of stopping cross sections to alloys of arbitrary composition and non-stoichiometric compounds.

This chapter describes a self-consistent procedure for testing Bragg's rule in solid alloys that is both elegant and facile. The results of the tests on three binary metal alloy systems indicate that any deviations from Bragg's rule are below the 1% sensitivity of the

test.

This test can be readily applied in several types of thin film reaction studies. By assuming, a priori, that Bragg's rule is valid, it can be used to verify the consistency of the experimental results obtained in the different stages of a reaction.

2.2 Formulas for Applying Bragg's Rule

Stopping cross section additivity, or Bragg's rule, is given by the formula

$$\varepsilon_{A_mB_n} = m \cdot \varepsilon_A + n \cdot \varepsilon_B \qquad (2.1)$$

where ε_A and ε_B are the atomic stopping cross sections of elements A and B, respectively, and $\varepsilon_{A_mB_n}$ is the molecular stopping cross section of a compound with the chemical formula A_mB_n (Bourland and Powers, 1971). The stopping cross section is given by

$$\varepsilon_A = \frac{1}{N_A}\frac{dE}{dx} \qquad (2.2)$$

where N_A is the number density of atom A (atoms/cm^3).

Sometimes the energy loss is available in experimental units of dE/pdx. A defining equation for Bragg's rule in this form can be derived by taking the definition of Bragg's rule in Eq. 2.1 and multiplying both sides by N_o, Avogadro's number, and substituting according to Eq. 2.2 to give

$$\frac{N_o}{N_{A_mB_n}}\left.\frac{dE}{dx}\right|_{A_mB_n} = m\cdot\frac{N_o}{N_A}\left.\frac{dE}{dx}\right|_A + n\cdot\frac{N_o}{N_B}\left.\frac{dE}{dx}\right|_B \qquad (2.3)$$

from which it follows directly that

$$M_{A_mB_n}\cdot\frac{N_o}{M_{A_mB_n}N_{A_mB_n}}\left.\frac{dE}{dx}\right|_{A_mB_n} = m\cdot M_A\cdot\frac{N_o}{M_AN_A}\left.\frac{dE}{dx}\right|_A + n\cdot M_B\cdot\frac{N_o}{M_BN_B}\left.\frac{dE}{dx}\right|_B \qquad (2.4)$$

where M_A and M_B are the atomic weights of A and B, respectively, and $M_{A_mB_n}$ is the molecular weight of A_mB_n. Since the molar density of A is given by N_A/N_o, it follows that

$$\rho_A = \frac{M_AN_A}{N_o} \qquad (2.5)$$

and equation 2.4 can be simplified to

$$\frac{M_{A_mB_n}}{\rho_{A_mB_n}}\left.\frac{dE}{dx}\right|_{A_mB_n} = m\cdot M_A\cdot\left.\frac{dE}{\rho dx}\right|_A + n\cdot M_B\cdot\left.\frac{dE}{\rho dx}\right|_B \qquad (2.6)$$

and since $M_{A_mB_n} = m\cdot M_A + n\cdot M_B$, it follows that

$$\frac{1}{\rho_{A_mB_n}}\left.\frac{dE}{dx}\right|_{A_mB_n} = \frac{mM_A}{mM_A + nM_B}\left.\frac{dE}{\rho dx}\right|_A + \frac{nM_B}{mM_A + nM_B}\left.\frac{dE}{\rho dx}\right|_B \qquad (2.7)$$

This is a form of Bragg's rule that is useful when analyzing the back-scattering spectra of samples of known composition and it can be extended to ternary compounds in the obvious way.

The following formulas for homogeneous, binary alloys of arbitrary composition assume that the mixture was produced by two layers of known thicknesses and that the volume of the alloys is the same as the volume of the two original layers. If the original bimetal structure had a film of A of thickness T_A and with a density ρ_A, and a layer of B of thickness T_B and density ρ_B, the density of the alloy ρ_{AB} will be

$$\rho_{AB} = \frac{\rho_A \cdot T_A + \rho_B \cdot T_B}{T_A + T_B} \qquad (2.8)$$

The partial density of A in the alloy, ρ_{AB}^{A}, will be

$$\rho_{AB}^{A} = \frac{\rho_A \cdot T_A}{T_A + T_B} \qquad (2.9)$$

with the partial density of B given by the obvious modification of Eq. 2.9. A closer inspection of Eq. 2.7 reveals that the partial density of A is also given by

$$\rho_{AB}^{A} = \frac{mM_A}{mM_A + nM_B} \cdot \rho_{AB} \qquad (2.10)$$

so Bragg's rule can also be stated as

$$\frac{1}{\rho_{AB}}\left.\frac{dE}{dx}\right|_{AB} = \frac{\rho^{A}_{AB}}{\rho_{AB}}\left.\frac{dE}{\rho dx}\right|_{A} + \frac{\rho^{B}_{AB}}{\rho_{AB}}\left.\frac{dE}{\rho dx}\right|_{B} \qquad (2.11)$$

This form of Bragg's rule is particularly useful for the test procedure described in part 2.3 when the stopping power is given in the experimental units of $dE/\rho dx$.

2.3 Concepts and Calculations

This test of Bragg's rule is based on the observation that the velocity dependence of the energy loss is similar in all stopping media. That is, the total stopping power of a layer of one element is about equal, at all particle energies, to the total stopping power of a layer of a different thickness of some other element.

It follows that in a two-layered structure, the total energy lost in penetrating both layers should be independent of the order of the two layers. For example, consider the case of of a layer of material A of thickness T_A on a layer of material B of thickness T_B . If the energy dependence of the stopping powers of A and B are related at all energies by the same proportionality factor, it follows that these two layers can be reversed without changing the total energy lost through the two layers.

The test of Bragg's rule consists of showing that an intermediate redistribution also produces no net change in the total energy loss. Bragg's rule must be invoked because these intermediate distributions

contain mixtures of the two originally separate species. This allows the substitution of A for B and vice versa to be performed at any depth and in any amount within the sample without changing the total energy loss. Bragg's rule therefore predicts that the total energy lost in penetrating a two-layered sample will be independent of the degree of mixing between the two layers, from the extremes of two separate layers to complete and uniform mixing between the two layers.

The application of this concept in a backscattering geometry is illustrated schematically in Figure 2.0. A backscattered particle obviously loses energy on both the incoming and outgoing paths. The similar energy dependence implies that the calculation of the substitution described above to simulate mixing will require nearly the same proportionality factor for the substitution on both the inward and outward trajectories.

In the backscattering experiment, the total energy lost by a particle that reaches the film-substrate interface and then scatters to emerge from the target should be the same before and after the layers are mixed. In measuring the total energy loss, it is convenient to compare the energy of a particle scattered from a particular element at the surface of the sample with the energy of a particle scattered from the same element at the sample-substrate interface. In the case of A on B, this energy width is defined as the difference between the energy of the signal produced by B at the surface $E_B = K_B \cdot E_{in}$ (see Equation 3.2) and the energy of the signal produced by the B at the substrate. The energy width of the B signal in the AB alloy is defined in exactly the same way.

Figure 2.0 Total energy loss in binary films before and after mixing. The contribution of a two-layered structure to the total energy loss in a backscattering experiment is illustrated by the figure on the left. The ion initially has an energy of E_{in}. As it penetrates the layer of A, it loses energy according to the stopping power of the A (••••). Similarly, the particle loses energy as it penetrates the B layer (----). After scattering at the B-substrate interface, the particle then exits while losing energy in the B layer(•-•-) and the A layer(-••-••) before finally emerging with a detected energy of E'.

The case after mixing the A and B layers is shown on the illustration on the right. The particle now loses energy going into the alloy(- - -) and coming out of the alloy sample(•-•-•-) to be finally detected with an energy of E".

Bragg's rule predicts that the energy loss going in and coming out, separately considered, should be the same in both cases. The similarity in the energy dependence of the stopping powers guarantees that the same calculations apply to both trajectories.

ENERGY LOSS REPRODUCIBILITY IN MIXED BINARY FILMS

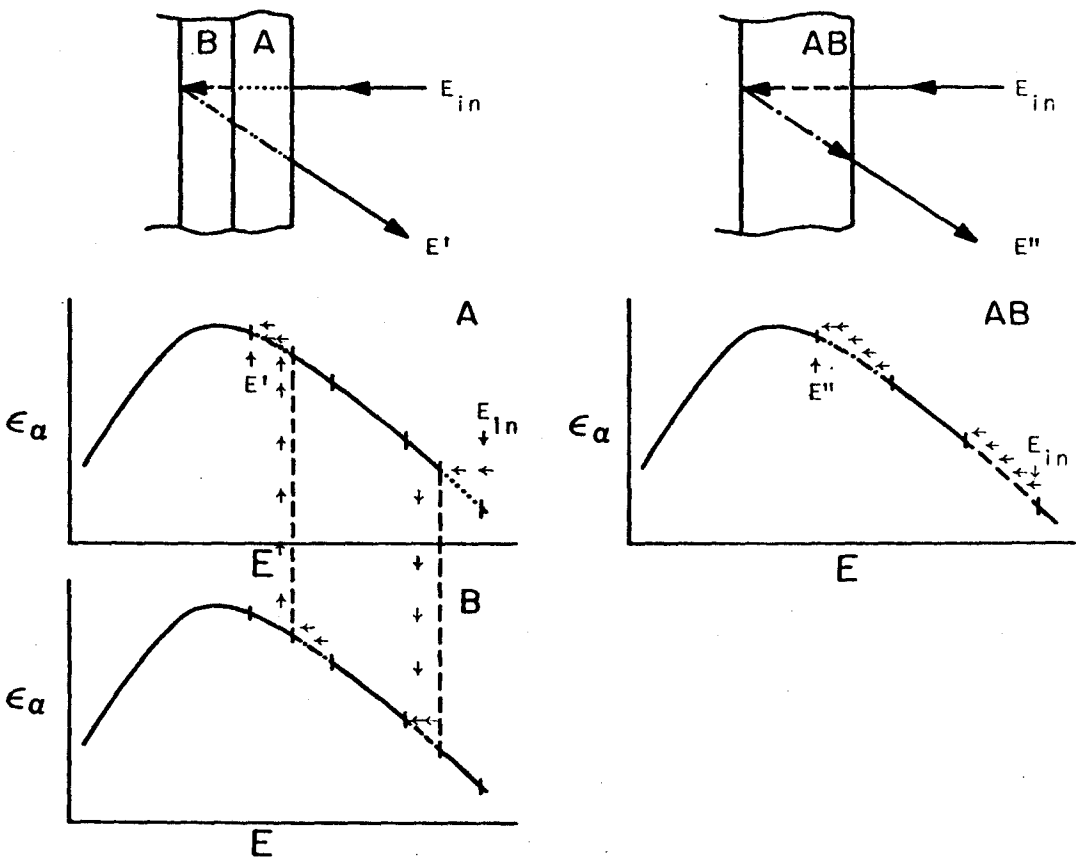

Figure 2.0

Bragg's rule and the similarity in the energy dependence of the stopping powers together predict that the total energy width of a two-layered target should be nearly independent of both the order of the two layers and the degree of mixing produced between the two layers. Thus, testing Bragg's rule by this procedure simply requires comparing the energy width of a two-layered sample with the energy width of the same sample after mixing the two layers.

In this intuitive argument for the plausibility of this test of Bragg's rule, it was assumed that the relative energy dependences of the stopping power is the same in all stopping media. Since this test was applied to helium ions with less than 2.5 MeV kinetic energy, this assumption is not exactly valid.

This assumption breaks down because the stopping powers of different stopping media do not have exactly the same relative energy dependence. To cite just one example of a failure of this assumption, there is a maximum in the energy dependence of the stopping cross section that occurs at different energies for different elements. The energy of this peak varies from about 600 keV for a light element like aluminum to over 1200 keV for a heavy element like gold. The relative energy dependence of the stopping power above and below this peak appears qualitatively to be less sensitive to the choice of the stopping medium.

A backscattering experiment samples the stopping power of the target material at two distinctly different energies. Applying this substitution concept separately to the incoming and outgoing trajectories may require different proportionality factors when calculating the substitution ratios for the two elements on the inward and outward paths.

Thus, this model might not predict that the total energy width will be fixed because the same composition ratio will necessarily be present on both the inward and outward trajectories.

However, this assumption is still approximately valid and it is not seriously violated. Because the impact of departures from the validity of this assumption is not obvious, this method of testing Bragg's rule was first evaluated by performing a detailed numerical simulation. The FØRTRAN listing and a description of the program used in this calculation are included as Appendix A.

The energy loss was first calculated for two-layered structures such as 500 Å of Au on 1500 Å of Ag. The procedure outlined in part 2.2 was used to calculate the Bragg-rule stopping power of the 2000 Å Au-Ag alloy film that would be formed by annealing this two-layered sample. This was then used to calculate the total energy loss after alloying. The energy of the particles backscattered from the silver-substrate interface was compared before(E'_{Ag}) and after(E''_{Ag}) this gedanken anneal since, in both cases, it is these particles that lose energy through the entire sample. In order to make a sensible estimate of the significance of any observed shifts, these were referenced to the energy of a particle scattered from Ag at the surface($E_{Ag} = K_{Ag}E_{in}$) by comparing the differences $E_{Ag}-E'_{Ag}$ and $E_{Ag}-E''_{Ag}$. The energy widths were also calculated for 1500 Å of Ag on 500 Å of Au to compare the energy widths of the gold signal before and after annealing the sample. The results of these calculations for various incident ion energies are shown in Table 2.1.

As expected, the calculated energy widths before($E_{Au}-E'_{Au}$; $E_{Ag}-E'_{Ag}$)

TABLE 2.1

E_{in} (keV)	$E_{Au}-E'_{Au}$ (keV)	$E_{Au}-E''_{Au}$ (keV)	$E'_{Au}-E''_{Au}$ (eV)	$E_{Ag}-E'_{Ag}$ (keV)	$E_{Ag}-E''_{Ag}$ (keV)	$E'_{Ag}-E''_{Ag}$ (eV)
2000	231.0516	230.9898	- 61.8	227.2541	227.4182	+ 64.1
1750	245.0112	244.9920	- 19.2	239.8594	239.8663	+ 6.9
1500	255.6523	255.6636	+ 11.3	248.9299	248.8991	- 30.8
1250	261.0997	261.1261	+ 26.4	252.6942	252.6480	- 46.2
1000	257.6225	257-5493	+ 26.8	247.7648	247.7224	- 42.4
750	240.2580	240.3763	+ 18.3	229.8730	229.8446	- 28.4
500	204.3968	204.4060	+ 9.2	194.7749	194.7595	- 15.4

Calculated energy widths. The total "backscattering energy widths" of the Au and Ag signals(see Figure 2.2) have been calculated for a two-layered sample of 500 Å Au and 1500 Å Ag for various incident $^4He^+$ ion energies. The Au energy width before annealing ($E_{Au}-E'_{Au}$) corresponds, for example, to a sample of 1500 Å Ag on 500 Å Au. Bragg's rule predicts that the energy width after annealing($E_{Au}-E''_{Au}$) must not be significantly different.

and after(E_{Au}-E''_{Au}; E_{Ag}-E''_{Ag}) the "annealing" are nearly unchanged. The small differences(E'-E") may be due to computational quantization errors or round-off errors in calculating the stopping power of the mixture. Since these differences are typically much less than 1 keV, it would be very difficult to observe these experimentally, and so the origin of these shifts was not actively pursued.

Calculations were also performed for 1500 Å Au/1500 Å Ag, 1500 Å Au/500 Å Ag, 500 Å Au/1500 Å Cu, 1500 Å Au/1500 Å Cu and 1500 Å Au/500 Å Cu and their alloys. The results are shown in Tables 2.2-2.6 . The total energy widths of these simulated smaples before and after annealing are also essentially unchanged at all incident energies for these pairs of metal layers.

Thus, Bragg's rule predicts that any changes in the total energy loss produced by alloying a two-layered sample should typically be less than 1 keV out of a total energy width of about 200-400 keV.

TABLE 2.2

E_{in} (keV)	$E_{Au}-E'_{Au}$ (keV)	$E_{Au}-E''_{Au}$ (keV)	$E'_{Au}-E''_{Au}$ (eV)	$E_{Ag}-E'_{Ag}$ (keV)	$E_{Ag}-E''_{Ag}$ (keV)	$E'_{Ag}-E''_{Ag}$ (eV)
2000	369.2808	368.8282	- 452.6	362.2867	362.2079	- 78.8
1750	388.7309	388.5463	- 184.6	379.6063	379.4355	- 170.8
1500	401.9423	401.9394	- 2.9	390.3900	390.1748	- 215.2
1250	405.5382	405.6226	+ 84.4	391.4063	391.2038	- 202.5
1000	393.5322	393.6246	+ 92.4	377.4018	377.2544	- 147.4
750	349.2286	349.2887	+ 60.1	342.7081	342.6246	- 83.5
500	297.4862	297.5062	+ 20.0	283.0501	283.0081	- 42.0

Calculated energy widths. The total backscattering energy widths of the Au and Ag signals (see Figure 2.2) have been calculated for a two-layered sample of 1500 Å Au and 1500 Å Ag for various $^4He^+$ incident particle energies. The Ag width before annealing($E_{Ag}-E'_{Ag}$) corresponds, for example, to a sample of 1500 Å Au on 1500 Å Ag. Bragg's rule predicts that the energy width after annealing($E_{Ag}-E''_{Ag}$) must not be significantly different.

TABLE 2.3

E_{in} (keV)	$E_{Au}-E'_{Au}$ (keV)	$E_{Au}-E''_{Au}$ (keV)	$E'_{Au}-E''_{Au}$ (eV)	$E_{Ag}-E'_{Ag}$ (keV)	$E_{Ag}-E''_{Ag}$ (keV)	$E'_{Ag}-E''_{Ag}$ (eV)
2000	254.2279	254.1781	- 49.8	249.6157	249.6909	+ 75.2
1750	267.7400	267.7377	- 2.3	261.6499	261.6702	+ 20.3
1500	277.4189	277.4502	+ 31.3	269.8154	269.7997	- 15.7
1250	281.7941	281.8403	+ 46.2	272.5506	272.5195	- 31.1
1000	277.0752	277.1183	+ 43.1	266.3891	266.3598	- 29.3
750	257.9996	258.0829	+ 29.3	246.7070	246.6884	- 18.6
500	219.1560	219.1719	+ 15.9	208.8131	208.8222	- 8.9

Calculated energy widths for 1500 Å Au and 500 Å Ag. The notation is similar to that in Tables 2.1 and 2.2. The difference in the energy widths before and after annealing are shown as $E'_{Au}-E''_{Au}$ and $E'_{Ag}-E''_{Ag}$. Bragg's rule predicts that this difference must be small compared to the total energy width. The calculated difference is probably too small to be observed experimentally with the current state of the art in sample preparation.

TABLE 2.4

E_{in} (keV)	$E_{Au}-E'_{Au}$ (keV)	$E_{Au}-E''_{Au}$ (keV)	$E'_{Au}-E''_{Au}$ (eV)	$E_{Cu}-E'_{Cu}$ (keV)	$E_{Cu}-E''_{Cu}$ (keV)	$E'_{Cu}-E''_{Cu}$ (eV)
2000	241.0828	241.4915	+ 408.7	227.1217	226.7300	- 391.7
1750	250.8334	250.9869	+ 153.5	233.3694	233.3586	- 10.8
1500	253.9991	253.9868	- 12.3	234.8821	235.0757	+ 193.6
1250	254.3374	254.2494	- 88.0	233.4362	233.6768	+ 240.6
1000	250.2915	250.4339	+ 142.4	227.3765	227.5437	+ 167.2
750	236.8661	236.8484	- 17.7	212.2104	212.2489	+ 38.5
500	205.1121	205.1619	+ 49.8	181.8787	181.8059	- 72.8

Calculated energy widths for 500 Å Au and 1500 Å Cu. The notation is similar to that in Tables 2.1, 2.2 and 2.3. All of the calculations assume that the films are of bulk density and assume the stopping cross sections of Cu and Ag as reported by Chu and Powers(1969) and of Au as reported by Lin, Olson and Powers(1973). Using other energy dependences for the stopping powers did not significantly affect the reproducibility.

TABLE 2.5

E_{in} (keV)	$E_{Au}-E'_{Au}$ (keV)	$E_{Au}-E''_{Au}$ (keV)	$E'_{Au}-E''_{Au}$ (eV)	$E_{Cu}-E'_{Cu}$ (keV)	$E_{Cu}-E''_{Cu}$ (keV)	$E'_{Cu}-E''_{Cu}$ (eV)
2000	377.1760	378.3001	+1124.1	356.6918	355.6316	-1060.2
1750	392.2485	392.4163	+ 167.8	365.4399	365.5134	+ 73.5
1500	399.1050	398.7094	- 395.6	367.5898	368.2069	+ 617.1
1250	399.2524	398.6897	- 552.7	363.2706	363.9241	+ 653.5
1000	388.1245	387.7601	- 364.4	348.6167	348.9668	+ 350.1
750	357.3332	357.3154	- 17.8	317.3875	317.3412	- 46.3
500	298.3830	298.6477	+ 264.7	263.5375	263.2137	- 323.8

Calculated energy widths for 1500 Å Au and 1500 Å Cu. The notation is similar to that in Tables 2.1, 2.2, 2.3 and 2.4. The shifts observed in these calculations are larger than those shown in the other five tables and these may now be large enough to be observed. However, they are more probably due to a small error in applying equation 2.11 when calculating the polynomial coefficients required for the program(see Appendix A).

TABLE 2.6

E_{in} (keV)	$E_{Au}-E'_{Au}$ (keV)	$E_{Au}-E''_{Au}$ (keV)	$E'_{Au}-E''_{Au}$ (eV)	$E_{Cu}-E'_{Cu}$ (keV)	$E_{Cu}-E''_{Cu}$ (keV)	$E'_{Cu}-E''_{Cu}$ (eV)
2000	257.1839	257.5920	+ 408.1	244.6578	244.2514	- 406.4
1750	269.4910	269.6011	+ 101.1	252.8082	252.7651	- 43.1
1500	276.8554	256.7730	- 82.4	256.7622	256.9138	+ 151.6
1250	279.6675	279.5087	- 158.8	256.1759	256.3714	+ 195.5
1000	274.8922	274.7639	- 128.3	248.4471	248.5779	+ 130.8
750	256.9633	256.9297	- 31.8	229.3771	229.3988	+ 21.7
500	219.3853	219.4476	+ 62.3	194.2808	194.2126	- 68.2

Calculated energy widths for 1500 Å Au and 500 Å Cu. The notation is similar to that in Tables 2.1, 2.2, 2.3, 2.4 and 2.5. All of these calculations show that Bragg's rule predicts that the energy width is very insensitive to the distribution of the constituent elements in Au-Ag and Au-Cu alloys. The similarity in the relative energy dependence of all stopping powers implies that this is also predicted for all other alloys and compounds.

2.4 Experimental Procedure

Since this experiment measures the reproducibility of the total energy lost in a sample, the sensitivity to deviations from Bragg's rule is limited, in part, by the reproducibility of the amount of stopping material. It is assumed that the measurement of the detected particle energy and the setting of the incident beam energy can be made with negligibly small errors. The reproducibility of the amount of stopping material can be adversely affected by side effects of the annealing process such as lateral transport of some of the stopping material, incorporation of additional stopping material from the ambient, loss of stopping material due to evaporation, or a chemical reaction with the substrate.

The effects of lateral transport can be minimized by carefully inspecting the samples for changes in the surface texture. The samples in this experiment were prepared on polished substrates to produce film samples with mirror finishes. After annealing, most of the samples retained their smooth appearance. Some of the samples were examined by phase contrast microscopy and scanning electron microscopy. These suggested that any surface coarseness produced by the annealing was due to separation of the sample film from the substrate. Since the particle beam extends over $\sim$2 mm of a sample, it is assumed that no significant lateral transport could plausibly have occurred over this large a distance.

The samples were annealed in a vacuum of better than 10^{-4} Torr to minimize the possibility of incorporating part of the annealing ambient into the films. Although this vacuum is not very impressive, it is

comparable to less than 1 ppm reactive impurity content in an inert gas like argon. In addition, this study was limited to the less-reactive elements of gold, silver, copper and aluminum. Although aluminum is chemically active, it rapidly forms a thin protective oxide that limits its reactions with the ambient. Copper, of course, oxidizes slowly.

The samples were annealed at the lowest possible temperature to minimize the vapor pressure of the constituent elements of the sample. Since all of the elements have negligible vapor pressures at the annealing temperatures of 200-500°C, the amount of stopping material lost by evaporation during the anneal is probably insignificant.

The substrates used in this study were selected, in part, to be chemically inert to reduce the chances of chemical interactions between the sample films and the substrates. No evidence of substrate-sample reactions were found after the annealing step either by visual inspection or in any of the backscattering spectra.

The reproducibility of the measured total energy loss is also affected by the lateral thickness uniformity of the thin film samples. Two different types of samples were prepared with special precautions to insure that the errors caused by any lateral nonuniformities were much smaller than the other errors in the experiment.

One type of target was prepared by vacuum evaporation from tungsten filaments onto substrates at room temperature. Material at least 99.99% pure was evaporated in a vacuum of better than 10^{-6} Torr at an average deposition rate of over 10 Å/sec. Half of the substrate was masked during the deposition of the first layer of stopping material. The sample was then exposed to the atmosphere to allow the orientation

of the mask to be changed by 90° on the sample. A second deposition of another stopping material produced a sample with four quadrants. The first quadrant had exposed substrate, the second and fourth quadrants each had single layers of the stopping materials, and the third quadrant had the two layers needed for testing Bragg's rule by the present method. This procedure is illustrated in Figure 2.1.

This type of sample was mounted on a two-axis goniometer with the intersection point of the four quadrants centered over the polar axis. The helium ion beam was then directed at a spot centered about 3 mm off the polar axis. The desired quadrant was then selected by changing the polar angle of the goniometer. The reproducibility of the beam spot location was better than ±1 mm and the azimuthal angle of the goniometer is also reproducible to within 0.2°. Since the filament-to-substrate distance during the deposition was about 10 cm, the calculated error due to thickness variations in the sample is less than 0.1%.

A second set of samples was prepared by evaporation from sources in alundum crucibles. The material was heated by radio frequency induction heating. The material used was at least 99.96% pure. Entrapment of additional impurities during the deposition was minimized by evaporating in a well cold-trapped vacuum of better than 10^{-7} Torr at an average deposition rate of over 15 Å/sec. The substrates were cooled to about 150°K to maximize the condensation rate from the vapor phase and hopefully improve the smoothness of the deposited film. The uniformity of these samples was guaranteed by the evaporation geometry. The evaporation source had a 2 cm diameter active area and it was located 35 cm from the substrates. The thickness variation in this

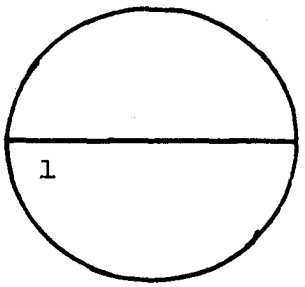

1. Deposit thin marker layer on entire substrate(optional)

2. Mask half of the substrate

   Deposit first layer on the unmasked half

3. Remove mask

   Deposit second thin marker layer(optional)

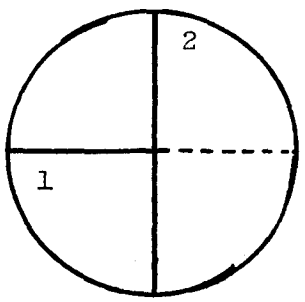

4. Rotate mask orientation 90°

   Deposit second layer

5. Remove mask

   Deposit final marker layer on entire sample(optional)

Produces sample with four sectors

1. Bare substrate
2. First layer alone
3. Two layers
4. Second layer alone

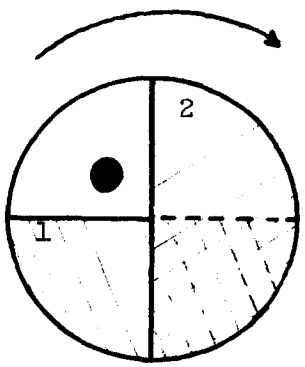

Mount on two-axis goniometer with normal axis at the center of the sample

Aim ion beam off-axis

Select desired quadrant by rotating the sample

Figure 2.1 Sample preparation procedure for producing a four-quadrant sample for the test of Bragg's rule in binary alloys.

evaporation system has been characterized by optical measurements(Wilts, 1972, unpublished), and the interpolated estimate of the maximum thickness variation on a 1 cm diameter sample is less than ±0.3%. This potential error was further reduced by reproducing the alignment of the ion beam spot location of the sample to within ±3 mm.

In addition to the two layers of stopping material, the samples used in the Au-Al and Au-Cu tests of Bragg's rule had gold marker layers. For example, in the Au-Al samples, there were two gold layers of less than 20 Å each deposited onto the two Al surfaces. These markers are so thin that they do not contribute significantly to the total energy loss in the sample. In the case of Au-on-Al, this was used to predict in advance the expected energy of particles scattered from the gold atoms at the substrate after annealing the sample. By including these markers and making use of the silicon and oxygen signals from the SiO_2 substrate, it was possible to simultaneously test Bragg's rule over a wide range of scattering kinematics for each setting of the incident particle energy. The use of these gold markers is also illustrated in a recent study of the energy straggling of 1-2 MeV ^4He(Harris and Nicolet, 1974).

2.5 Experimental Results

This method of testing Bragg's rule was applied to the binary metal alloy systems of Au-Ag, Au-Cu and Au-Al. Because copper and silver are not miscible in solid solutions, the Ag-Cu binary system was not included in this study. The Au-Ag and Au-Cu pairs both form metallic alloys of arbitrary composition. Gold and aluminum form a series of semi-insulating intermetallic compounds, one of which is familiarly known

to the semiconductor industry as the "purple plague." The results will be described in detail for one particular sample of Ag on Au. Since these are typical and representative of the results on the other pairs, the results for the other cases will only be summarized.

2.5.1 Ag-on-Au

A four-quadrant sample was prepared by depositing a 1900 Å Ag film onto a 1000 Å Au film on a thermally oxidized silicon substrate. The thickness of the two layers was determined by backscattering 2 MeV $^4He^+$ from the quadrants containing pure Au and pure Ag and using the appropriate stopping cross sections as reported in the literature(Chu and Powers, 1969; Lin, Olson and Powers, 1973).

The backscattering spectra of all four quadrants were taken for incident helium ion energies of 500-2000 keV. The sample was then annealed for about 30 min at 400°C in a vacuum of about 10^{-4} Torr. Backscattering spectra of the four quadrants were again taken using the same particle energies and the total energy loss before and after annealing were compared. The energies of the scattered particles were calibrated by using the energies of particles elastically scattered from surface atoms of known masses. This procedure guarantees that this step in the experiment is limited only by the precision of the reproducibility of the incident particle energy and not on the accuracy of the setting of the particle energy. In addition, the absolute particle energy was calibrated against a precision pulser that had in turn been calibrated using a number of natural α-particle sources. Furthermore, other students had recently performed calibrations using nuclear

reactions.

The backscattering spectra taken using 2 MeV $^4He^+$ before and after annealing the sample are shown in Figure 2.2. Also shown are decompositions of the spectra into the separate Au and Ag contributions. The arrow labeled E_{Au} identifies the energy of a particle scattered from a gold nucleus at the surface of the sample. The arrow labeled E'_{Au} in the pre-annealing spectrum indicates the lowest energy for a particle scattering from a gold nucleus in the sample. Similarly, the arrow marked E''_{Au} indicates the lowest energy observed for the gold signal in the post-annealing spectrum. The notation for silver is similar. The total backscattering energy of the gold signal is defined in the obvious way by taking the difference between $E_{Au} = K_{Au}E_{in}$ and either E'_{Au} or E''_{Au}.

Although the two rear steps in the pre-anneal spectrum(E'_{Au} and E'_{Ag}) are not clearly resolved in the experimental data, they are shown clearly separated in the decomposition of the two signals. Both of the decompositions represent spectra calculated using the computer program described in Appendix A. In the pre-annealing spectrum, the thickness values for the two layers used in the calculation were taken from the 2.0 MeV backscattering spectra(see above). The consistency of these values can be tested by comparing the calculated and experimental values for the highest energy of the Au signal in the pre-anneal spectrum. The agreement, shown in the top half of Figure 2.2, is obviously good. Another less reliable test was performed by differentiating the low energy edge of the total signal to locate E'_{Au} and E'_{Ag}. This also agreed with the calculated results to within ±1 channel, or about ±2 keV.

Figure 2.2 Top: Backscattering spectrum of a 1900 Å Ag film on 1000 Å Au. The Au signal is shifted toward lower energies by the overlying Ag, causing an overlap in the two signals. E_{Au} is the energy for backscattering from Au at the surface and E_{Ag} is the corresponding energy for Ag. E'_{Au} is the low energy edge of the Au signal and E'_{Ag} is the low energy edge of the Ag signal. The line is a calculated spectrum that assumes the stopping cross sections of Lin et al(1973) and Chu and Powers(1969) and assuming the thickness values given above. The backscattering yield is fitted only at E_{Ag}.

Bottom: Backscattering spectrum of the same film after annealing for 30 min at 400°C. E''_{Au} and E''_{Ag} are the low energy edged after annealing. The line is calculated by assuming complete and homogeneous mixing of the two metal layers and the yield is fitted only at E_{Au}.

If Bragg's rule is valid, the total energy loss through the entire film must be the same before and after anneal. This implies that E'_{Au} and E''_{Au} must be the same in both spectra.

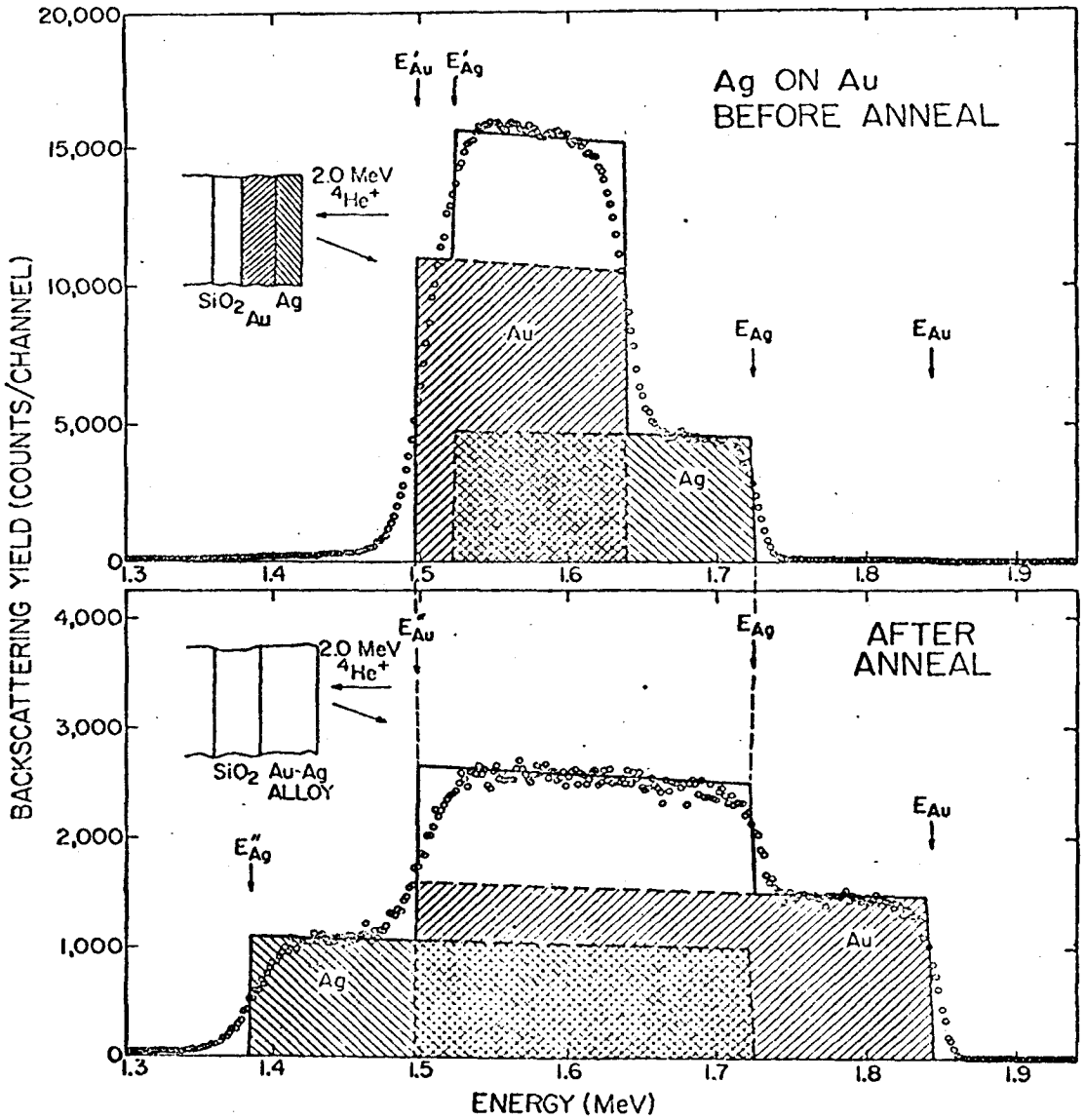
Ag ON Au
BEFORE ANNEAL
2.0 MeV
4He+
SiO2 Au Ag
Au
Ag
AFTER
ANNEAL
SiO2 Au-Ag
ALLOY
BACKSCATTERING YIELD (COUNTS/CHANNEL)
ENERGY (MeV)

Figure 2.2

The pre-annealing spectrum shown is a worst case example for determining E'_{Au} and E'_{Ag}. At all lower incident ion energies, the two steps were clearly and easily distinguished. The post-annealing spectrum was calculated by assuming that the two initial films formed a homogeneous alloy.

Bragg's rule predicts that E'_{Au} and E''_{Au} must be the same. The measured values of $E_{Au}-E'_{Au}$ and $E_{Au}-E''_{Au}$ for various incident particle energies of 0.5-2.0 MeV are given in Table 2.7. Within the accuracy of the experiment(±2 channels, or $\lesssim$ 4 keV), the energy width is unchanged after annealing, confirming Bragg's rule to an accuracy of about 1%.

Also shown in the table are the calculated energy width of the gold signal(both before and after annealing) and the experimental and theoretical energy widths of the silver signal after annealing. These calculations were also performed using the thickness values as determined by 2 MeV backscattering from the single layered quadrants. The good agreement in these cases demonstrates the accuracy of the computer program and the accuracy of the stopping cross section data used in the calculations.

2.5.2 Other Samples

Similar experiments were performed on a four-quadrant sample of Au-on-Ag. Since the two signals did not overlap in the pre-anneal data, the determination of the Ag signal energy width was much easier. The results were similar to those for the Ag-on-Au sample just described.

More measurements of both Au-on-Ag and Ag-on-Au were performed on a series of samples with initial film thicknesses of 1000 Å to 4000 Å

TABLE 2.7

E_{in} (keV)	$E_{Au}-E'_{Au}$ (keV)	$E_{Au}-E''_{Au}$ (keV)	ΔE_{Au} (keV)	$E_{Ag}-E''_{Ag}$ (keV)	
	experimental		calculated	exp.	calc.
	before anneal	after anneal	before & anneal	after anneal	
2000	343	344	346	343	340
1750	368	366	366	361	357
1500	381	378	379	370	368
1250	372	377	382	362	368
1000	372	374	371	357	355
750	336	335	327	318	321
500	284	278	276	261	262

The difference is given between the energy of ^{4}He backscattered from an atom of Au at the surface($E_{Au}=K_{Au}E_{in}$) and at the substrate(E'_{Au} or E''_{Au}) in a two-layered film before($E_{Au}-E'_{Au}$) and after($E_{Au}-E''_{Au}$) the film was annealed to produce complete and homogeneous mixing. The notation for Ag is similar. The sample used in these measurements is the sample shown in the spectra in Figure 2.2 with 1900 Å Ag on 1000 Å Au. ΔE_{Au} is the calculated value of $E_{Au}-E'_{Au}$ or $E_{Au}-E''_{Au}$ using the same procedures as in calculating Tables 2.1-2.6. The close equality observed in $E_{Au}-E'_{Au}$ and $E_{Au}-E''_{Au}$ confirm the applicability of Bragg's rule. Also shown are the experimental and calculated values for $E_{Ag}-E''_{Ag}$ for

Table 2.7 caption(continued)

the silver signal after annealing the sample. The agreement demonstrates the accuracy of the computed spectra. The uncertainties in the experimental values are less than or equal to ±2 channels, or approximately ±4 keV. The calculated values are based on the thicknesses of the pure metal quadrants(see Figure 2.1) as measured by backscattering at 2.0 MeV and using the Ag stopping cross sections of Chu and Powers(1969) and the Au stopping cross sections of Lin, Olson and Powers(1973).

for the pure elements and using samples with thickness ratios of about 1:1 to 1:3. These samples were prepared on glass substrates cooled to about 150°K, as described above. These measurements also produced similar results.

The maximum deviation observed on these other Au-Ag samples was about 2%. In general, the Au-Ag mixtures obey Bragg's rule to within ±1% from 0.3 to 2.0 MeV for samples with the appropriate thicknesses for a backscattering experiment(2000-5000 Å).

The Au-Al system was tested for both Au-on-Al and Al-on-Au using four-quadrant samples on thermally oxidized silicon substrates. The thin Au marker layers as well as the Si and O signals from the substrate were all used to test the reproducibility of the energy loss through the alloyed layer over a wide kinematic range. The post-annealing spectra showed a non-uniform distribution of gold and aluminum, a result that is consistent with the simultaneous formation of several intermetallic compound layers. The observed shifts in the marker energies for incident ion energies of 0.75-2.25 MeV were typically smaller than the estimated experimental accuracy of about 1%, although some did occassionally exceed 1%.

Measurements for Au-on-Cu were made using 1.0-2.25 MeV incident ion energies while measurements for Cu-on-Au were made only at 2.0 MeV. These samples were made by vacuum deposition onto cooled glass substrates, as described above. A small systematic increase in the energy width of +1±1% was observed after annealing the samples. This could have been caused by impurity absorption, and it has been suggested that an annealing vacuum of 10^{-4} Torr is not sufficient to prevent oxidation

of the copper(J. M. Poate, 1973).

2.6 Discussion

With minor reservations about the Au-Cu system, the results establish the applicability of Bragg additivity in the three binary metal combinations used in this experiment. Although gold is common to all three pairs, it is not believed that gold is in any way unique. Based on these results and other opportunities for applying this test, it is believed that Bragg's rule will be applicable to within 1% in all solid phase systems.

The ease with which this test can be applied can have significant implications on the practice of ion backscattering spectrometry. An important class of problems that has been extensively studied by backscattering is the interaction between thin layers where the substrate does not interact either chemically or metallurgically. Some recent examples of this of this have been studies of Ag-Al(Westmoreland et al, 1973) and Au-Al(Campisano et al, 1973) intermetallic compound formation, reliability studies of the metallization techniques used in manufacturing integrated circuits(Bower, 1973; Lugujjo et al, 1974), and the reactions between various metals and thermally grown silicon dioxide (Krautle et al, 1973). The reproducibility of the energy of the ions scattered from those atoms that remain at the sample-substrate interface can be taken as confirmation of the validity of Bragg's rule in that particular system. This makes the testing of Bragg's rule a by-product of many other experiments. A more practical approach would be to assume that Bragg's rule is valid and to use the reproducibility to test for

anomalous effects in the sample handling. For example, a shift of this signal to higher energies would be evidence of the loss of some of the sample material. Conversely, a shift to lower energies would correspond to the incorporation of additional stopping material, as might occur if the sample became oxidized.

REFERENCES

Chapter 2

P. D. Bourland and D. Powers, 1971, Phys. Rev. B., vol. 3, p. 3635.

R. W. Bower, 1973, thesis, Steele Laboratory of Electrical Sciences, California Institute of Technology(unpublished).

S. U. Campisano, G. Foti, F. Grasso, J. W. Mayer and E. Rimini, 1973, Proceedings of the International Conference on Applications of Ion Beams to Metals, p. 159.

W. K. Chu and D. Powers, 1969, Phys. Rev., vol. 187, p. 478.

J. M. Harris and M-A. Nicolet, 1974, unpublished.

H. Krautle, W. K. Chu, M-A. Nicolet, J. W. Mayer and K. N. Tu, 1973, Proceedings of the International Conference on Applications of Ion Beams to Metals, p. 193.

H. Krautle, M-A. Nicolet and J. W. Mayer, 1973, J. Appl. Phys., vol. 44, p. 3851.

W. K. Lin, H. G. Olson and D. Powers, 1973, Phys. Rev. B., vol. 8, p. 1881.

E. Lugujjo, R. Shima and M-A. Nicolet, 1974, unpublished.

J. M. Poate, 1973, private communication.

J. E. Westmoreland and W. H. Weisenberger, 1973, Thin Solid Films, vol. 19, p. 349.

Chapter 3

STOICHIOMETRIC COMPOUNDS

3.1 Introduction

Thin layers of dielectric compounds represent an important class of materials that has been investigated by ion backscattering. Examples include the formation of iron oxides(Feng, Bajorek and Nicolet, 1972), anodization studies of aluminum(Kamoshida and Mayer, 1972; Brown and Mackintosh, 1973) and tantalum(Chu, Nicolet, Mayer and Evans, 1974), the range of heavy ions in insulators(Chu, Crowder, Mayer and Ziegler, 1971), and the composition of films produced by chemical vapor deposition (Kamoshida, Mitchell and Mayer, 1971) and liquid phase epitaxy(Nicolet and Feng, 1974).

These dielectrics almost invariably contain either nitrogen, oxygen or some halogen. Since these elements usually are not conveniently available in the solid phase, it is difficult to test Bragg's rule in these materials by applying the procedure described in the previous chapter.

One possible alternative is to attempt to make an absolute measurement of the stopping cross section in the compound. Only the uncertainties in the thickness measurements limit the sensitivity of this approach. Gravimetric measurements of the amount of stopping material are at once the most accurate and least precise since weighing the amount of stopping material requires the fewest assumptions about the nature of the sample while it also has the largest inherent experimental uncertainties. Although the actual thickness of a dielectric

layer can be measured by using ellipsometry, interferometry or mechanical techniques, this would mean that the the density of the sample must also be known. One problem in this approach is that the particular allotropic phase and the density of a sample can depend significantly on the details of the fabrication procedure.

The approach used in this chapter is a combination of the methods proposed by Baglin et al(1974) and Feng et al(1973). The test is based on examining the self-consistency of the backscattered particle yields from several elements and their oxides. A failure to achieve this self-consistency would be taken as evidence of a violation of Bragg's rule. This procedure assumes that the samples are stoichiometric and that the Rutherford scattering cross section formula is applicable. Section 3.2 describes some of the basic backscattering formulas that are used in the calculations; the two assumptions just described are both implicitly included in the use of these formulas. Since the measurements were performed on two-layered targets, section 3.3 explores in detail the use of two-layered targets and how they modify the simpler concepts of section 3.2. The logic of the experiment, explicitly for the case of the five oxides used in this experiment, is presented in section 3.4.2(a) and the experimental results are presented and developed in section 3.4.2(d). A simplified application of this whole approach is illustrated in section 3.4.3 using the example of SiC. The implications of the results are discussed in part 3.5.

3.2 Basic Concepts

3.2.1 Energy Loss in Backscattering Geometries

Since the probability of a nuclear collision is extremely low, it is assumed that the backscattered ions follow straight line trajectories both into the sample before scattering and out of the sample after scattering. The apparent rate of energy lost by a backscattered particle is given by the [S]-factor, where

$$[S] = \frac{K}{|\cos\theta_{in}|}\left.\frac{dE}{dx}\right|_{E_{in}} + \frac{1}{|\cos\theta_{out}|}\left.\frac{dE}{dx}\right|_{E_{out}} \qquad (3.1)$$

where θ_{in} and θ_{out} are the incoming and outgoing angles with respect to the normal to the plane of the target. K is the kinematic factor that gives the ratio of the particle energies before and after elastic scattering and it is defined by

$$K = \left(\frac{m\cdot\cos\theta + \sqrt{M^2 - m^2\cdot\sin^2\theta}}{m + M} \right)^2 \qquad (3.2)$$

where m is the mass of the projectile, M is the mass of the scattering center and θ is the laboratory scattering angle. Thus, if the scattering geometry and the rate of energy loss are known, the [S]-factor relates the apparent energy lost to the depth in the target.

Similarly, the [ε]-factor, defined by

$$[\varepsilon] = \frac{K}{|\cos\theta_{in}|}\cdot\varepsilon_{in} + \frac{1}{|\cos\theta_{out}|}\cdot\varepsilon_{out} \qquad (3.3)$$

is another way of expressing the net rate of energy loss for a back-

scattered particle. In this case, ε is the stopping cross section and it is given by

$$\varepsilon = \frac{1}{N}\frac{dE}{dx} \qquad (3.4)$$

where N is the number density(cm^{-3}) of the stopping medium. The relation between an increment of energy lost δE and the corresponding increment in target depth δx is just

$$\delta E = [S]\cdot\delta x = [\varepsilon]\cdot N\cdot\delta x \quad . \qquad (3.5)$$

In practice, for a given incident particle energy and a target of uniform composition, $[S]$ (and $[\varepsilon]$) change by less than 5% for maximum target depths of 0.5-1.0 μm.

3.2.2 Thick Target Yields

In a particular scattering geometry and for an incident ion energy E_o, the thick target yield Y is the fraction of particles scattered into the solid angle of detection $\delta\Omega$ within a particular energy interval $[KE_o-\delta E, KE_o]$. This energy interval δE corresponds to a thin layer at the surface of the target of thickness δx , where

$$\delta x = \frac{\delta E}{[S]} = \frac{\delta E}{N[\varepsilon]} \quad . \qquad (3.6)$$

Since the number of scattering centers in this layer is $N\cdot\delta x$, the thick target yield Y will be given by

$$Y = Q \cdot \sigma(\Theta) \cdot N \cdot \delta x \cdot \delta\Omega = Q \cdot \sigma(\Theta) \cdot (\delta E / [\varepsilon]) \cdot \delta\Omega \qquad (3.6)$$

where Q is the incident ion dose and $\sigma(\Theta)$ is the appropriate scattering cross section.

If the scattering geometry is fixed and the total dose is somehow reproduced, the ratio of the thick target yields from A and from B will reduce to

$$\frac{Y_A}{Y_B} = \frac{\sigma_A / [\varepsilon]_A}{\sigma_B / [\varepsilon]_B} \qquad (3.7)$$

since the other factors obviously cancel. By assuming that the ratio of the scattering cross sections is known, the ratio of the $[\varepsilon]$-factors can be determined from a measurement of the yield ratio. It is usually assumed that the scattering cross section is given by the Rutherford formula. This is the basis of the method used by Baglin et al(1974).

3.2.3 Binary Oxides

The thick target spectrum from a binary oxide consists of the superposition of the signals produced by scattering from the cation nuclei("metal") and the oxygen. Since the metals used in this experiment are all more massive than oxygen, the signal from the metal appears at a higher energy than the corresponding oxygen signal. In this experiment, the attention is focussed on the signal from the metal and the metal atoms in the oxide, and the oxygen signal is usually ignored.

The signal yield from the metal atoms in an oxide will be lower

than the thick target yield from a pure metal target because the oxygen will contribute to the energy loss in the oxide without also contributing to the scattering yield. For example, consider the A signals from pure A and A_mB_n. Since the definition of the $[\varepsilon]$-factor is a linear combination of the stopping cross sections at two energies, the application of Bragg's rule to define a molecular $[\varepsilon]$-factor gives

$$[\varepsilon]^A_{A_mB_n} \doteq m\cdot[\varepsilon]^A_A + n\cdot[\varepsilon]^A_B \qquad (3.8)$$

where the subscripts identify the stopping material and the superscripts identify the scattering site(thus determining the value of K_A (Eq. 3.2) to be used in calculating $[\varepsilon]^A$ according to Eq. 3.3). Thus, $[\varepsilon]^A_B$ represents the appropriate $[\varepsilon]$-factor for scattering from an atom of A embedded in a stopping matrix of B. The yield of the A signal from the A_mB_n will be

$$Y^A_{A_mB_n} = Q\cdot\{m\cdot\sigma_A(\theta)\}\cdot\{\delta E/[\varepsilon]^A_{A_mB_n}\}\cdot\delta\Omega \qquad (3.9)$$

since there are m atoms of A in every molecule of A_mB_n. The ratio of the A signals from the A_mB_n and from pure A will be

$$\frac{Y^A_A}{Y^A_{A_mB_n}} = \frac{\sigma_A/[\varepsilon]^A_A}{m\cdot\sigma_A/[\varepsilon]^A_{A_mB_n}} = \frac{\frac{1}{m}\cdot[\varepsilon]^A_{A_mB_n}}{[\varepsilon]^A_A} \qquad (3.10)$$

since the scattering cross section terms now cancel.

Substituting Equation 3.8 into Equation 3.10 yields the expression

$$\frac{Y_A^A}{Y_{A_mB_n}^A} \doteq \frac{[\varepsilon]_A^A + \frac{n}{m} \cdot [\varepsilon]_B^A}{[\varepsilon]_A^A} > 1 \qquad (3.11)$$

where the $\doteq$ indicates that Bragg's rule has been assumed. It follows that the ratio of the $[\varepsilon]$-factors can be calculated from the yield by simply rearranging Eq. 3.11 into

$$\frac{[\varepsilon]_B^A}{[\varepsilon]_A^A} \doteq \frac{m}{n} \cdot \left(Y_A^A / Y_{A_mB_n}^A - 1 \right) \quad . \qquad (3.12)$$

If the relative energy dependence of the stopping cross section is known, the ratio $\varepsilon_A/\varepsilon_B$ can be calculated from the $[\varepsilon]$-factor ratio by using Eq. 3.3 .

In many cases, the ratio of the stopping cross sections for the pure elements $\varepsilon_A/\varepsilon_B$ can also be determined by comparing the thick target yields of A and B . A simple rearrangement of Eq. 3.7 gives

$$\frac{[\varepsilon]_A^A}{[\varepsilon]_B^B} = \frac{\sigma_A/Y_A^A}{\sigma_B/Y_B^B} \qquad (3.13)$$

where the notation of Eq. 3.8 has been used to update the notation in Eq. 3.13. This constitutes a method of determining $\varepsilon_A/\varepsilon_B$ that is independent of the measurement in the A_mB_n . Bragg additivity will require that these two ratios must be the same.

3.3 Two-Layered Structures

3.3.1 Motivation for Using Two-Layered Samples

Although the procedure described above is conceptually very simple, and therefore very attractive, it requires absolute reproducibility of the probe ion dose. This requires accurate current integration and exact correction for the electronic dead time. Since different materials can have different secondary emission rates and certainly have different effective scattering cross sections, eliminating these as potential sources of error requires great care.

The total dose can be made nearly identical for two materials by simultaneously measuring the signal yields from these two materials in a two-layered structure. Since there is negligible attenuation of the particle flux and because the same pulse rate will be present for both signals, the fluence and counting efficiency will be identical for both layers. The ratio of the heights of the two signals from the interface between the two layers will be given by the appropriate ratios of scattering cross sections and $[\varepsilon]$-factors. Since the incoming particle energy will be the same for both layers at the interface, the energy dependence of the (Rutherford) scattering cross section should have no significant effect on the ratio of the heights as evaluated from the interface between the two layers.

3.3.2 Example of a Spectrum from a Two-Layered Sample

A typical spectrum from a two-layered structure is schematically illustrated in Figure 3.1 for the case of Au on Ag. A sample consisting of a thin Au film on a thin Ag film on a light substrate, as shown in

Figure 3.1 Schematic representation of the backscattering spectrum of a two-layered target composed of a thin Au layer on top of a thin Ag layer. The ratio Y_{Au}/Y_{Ag}, evaluated at the interface as indicated in the figure, can be used to determine the ratio of the stopping cross sections in the two materials.

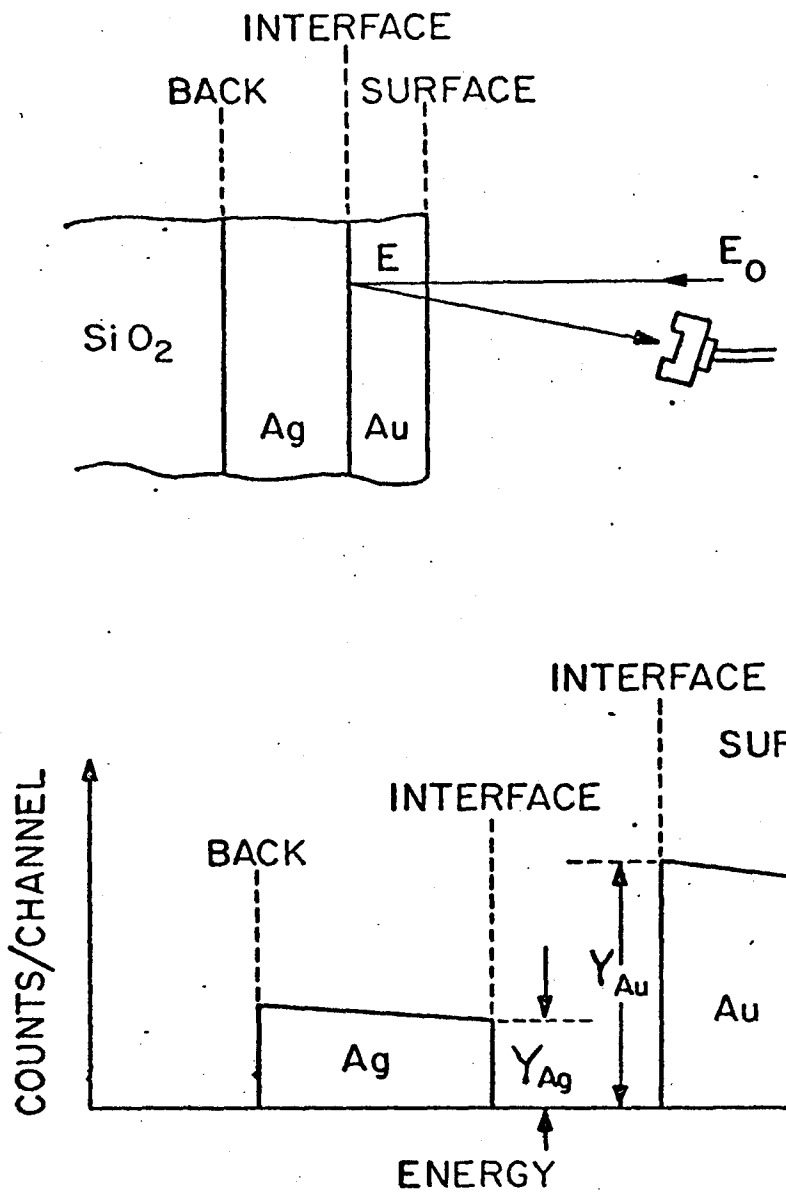
INTERFACE
BACK
SURFACE
E
E_o
SiO_2
Ag
Au
INTERFACE
SURFACE
INTERFACE
BACK
COUNTS/CHANNEL
Y_{Au}
Au
Ag
Y_{Ag}
ENERGY

Figure 3.1

Figure 3.2 An experimental spectrum of a thin layer of Au on top of a thin layer of Ag. The solid line is a calculated spectrum that assumes the stopping cross sections as reported by Lin et al(1973) and Chu and Powers(1969). The spectrum was calculated using the program described in Appendix A.

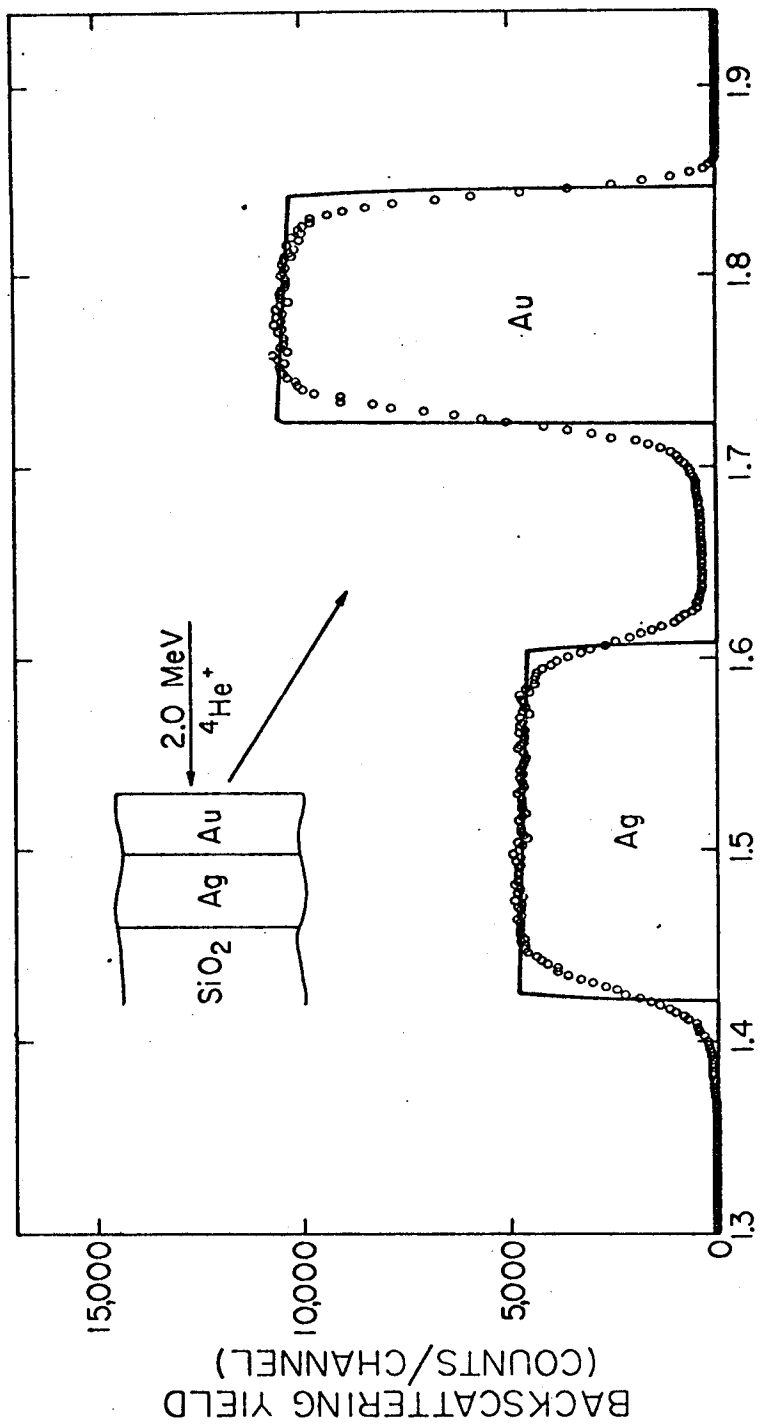
BACKSCATTERING YIELD
(COUNTS/CHANNEL)
15,000
10,000
5,000
0
1.3
1.4
1.5
1.6
1.7
1.8
1.9
ENERGY (MeV)
Au
Ag
2.0 MeV
$^4He^+$
Au
Ag
SiO_2

Figure 3.2

the top of the figure, will produce a spectrum similar to the one shown at the bottom of the figure. The high energy part of the Au signal is produced by particles scattered from the surface while the low energy part of the Au signal is due to the Au at the Au-Ag interface. Similarly, the high energy part of the Ag signal is from particles scattered by Ag nuclei at the Au-Ag interface and the low energy signal is from the Ag-substrate interface. The heights at the interface are indicated by Y_{Au} and Y_{Ag}. An experimental spectrum of Au on Ag is shown in Figure 3.2. The solid line shown in this figure is the calculated spectrum for this sample using the program in Appendix A.

The ratio of the heights at the interface is almost exactly given by Equation 3.7. The corrections to using the thick target yield formulas are determined analytically in the next section and the magnitude of these corrections is shown to be small both theoretically and experimentally.

3.3.3 Internal Backscattering Yields

The effects of the outward trajectory on the backscattering yield ratio were first recognized by Chu(1973, unpublished) and the numerical and experimental verification were first reported by Feng et al(1973). Brice(1973) subsequently reported a rigorous mathematical derivation of this effect on the thick target yield without commenting on the yield ratios from multi-layered samples. The intuitive argument of Feng et al will be presented in part (a), followed by an extension of Brice's results in part (b) and the experimental verification of this effect in part (c). In all cases, the effects are shown to be negligibly small.

(a) Qualitative Considerations. Consider the case of backscattering from a thin layer δx at a depth x in the interior of a target, as shown schematically in Figure 3.3. A particle with an incident energy E_{in} will reach the depth x with some lower energy E. If the particle is backscattered at x and through an angle θ it will have an energy $E_1 = KE$ at x and it will emerge from the target with an energy E_3. A particle backscattered from $x + \delta x$ will have an energy $E_1 - \delta E_1$ at depth x and it will exit with energy $E_3 - \delta E$. If the $[\varepsilon]$-factors and the scattering cross sections are evaluated at E-- the incoming particle energy at depth x -- the backscattered particle yield from δx is

$$Y = Q \cdot \delta\Omega \cdot \sigma \cdot \delta E_1 / [\varepsilon] \quad . \qquad (3.14)$$

Because the stopping cross section ε is a function of the particle energy, δE_1 will not be exactly equal to δE. The energy width in the interior of the target δE_1 is modified by the intervening material on the outward path to produce a corresponding detected energy width δE.

The magnitude of this effect can be estimated by a detailed consideration of the energy loss on the exiting trajectory. The total energy lost on the outward path $E_1 - E_3$ is given by

$$E_1 - E_3 = \int_0^t \varepsilon\{E(x)\} \cdot N \cdot dx \qquad (3.15)$$

where $t = x/|\cos\theta|$ is the path length for the outgoing particle. In the approxiamtion that $E_1 - E_3$ is small compared to E_1, the stopping

Figure 3.3 A schematic representation of backscattering from a layer δx_1 at a depth x within the target. For clarity, the layer δx_1 is drawn as separated from the rest of the target.

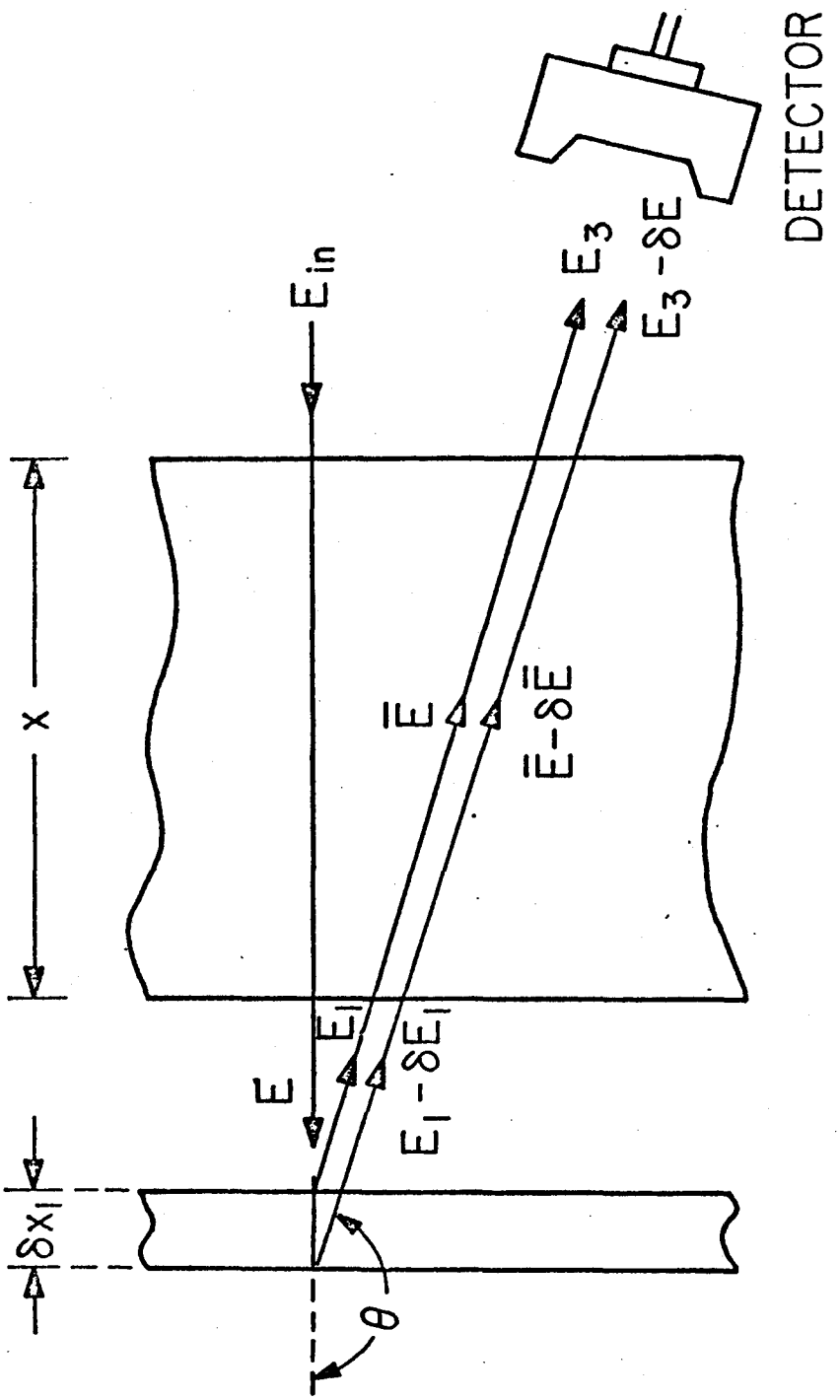
DETECTOR
E_{in}
E_3
$E_3 - \delta E$
$\bar{E}$
$\bar{E} - \delta \bar{E}$
x
E_1
$E_1 - \delta E_1$
E
δx_1
θ

Figure 3.3

cross section $\varepsilon(E)$ can be approximated by some average constant value and Equation 3.15 can be simplified to

$$E_1 - E_3 = \varepsilon(\bar{E}) \cdot N \cdot t / |\cos \theta| \qquad (3.16)$$

where $\bar{E}$ is some appropriate energy between E_1 and E_3. Similarly,

$$(E_1 - \delta E_1) - (E_3 - \delta E) = \varepsilon(\bar{E} - \delta\bar{E}) \cdot N \cdot t / |\cos \theta| \qquad (3.17)$$

where $\delta\bar{E}$ is between δE_1 and δE. Expanding $\varepsilon(\bar{E} - \delta\bar{E})$ into a Taylor's series and keeping only first order terms gives

$$\delta E = \delta E_1 - N \cdot t \cdot \left.\frac{d\varepsilon}{dE}\right|_{\bar{E}} \cdot \delta E \qquad (3.18)$$

or, more compactly,

$$\delta E_1 = \{ 1 + \varepsilon'(\bar{E}) \cdot N \cdot t \} \cdot \delta E \qquad (3.19)$$

where ε' is the derivative of ε with respect to the particle energy. The difference between δE_1 and δE is due to the energy dependence of the stopping cross section and to first order it is also proportional to the amount of intervening material. The magnitude of the correction term $\varepsilon' \cdot N \cdot t$ for 2000 Å Au ranges from about +6% at 0.6 MeV to -2% at 2.0 MeV, as illustrated in Figure 3.4.

For a two-layered structure of A on B, the experimentally measured heights at the interface will be

$$\frac{Y_A}{Y_B} = \frac{\sigma_A / [\varepsilon]_A}{\sigma_B / [\varepsilon]_B} \cdot \frac{\delta E_{1A}}{\delta E_{1B}} \qquad (3.20)$$

Figure 3.4 Interior energy loss corrections. The magnitude of the correction factor $\epsilon' Nt$ for 1000 Å Au is illustrated. The detected energy loss is greater than the corresponding interior energy loss by the factor $[\ 1 + \epsilon' Nt\ ]$ evaluated at the outgoing particle energy.

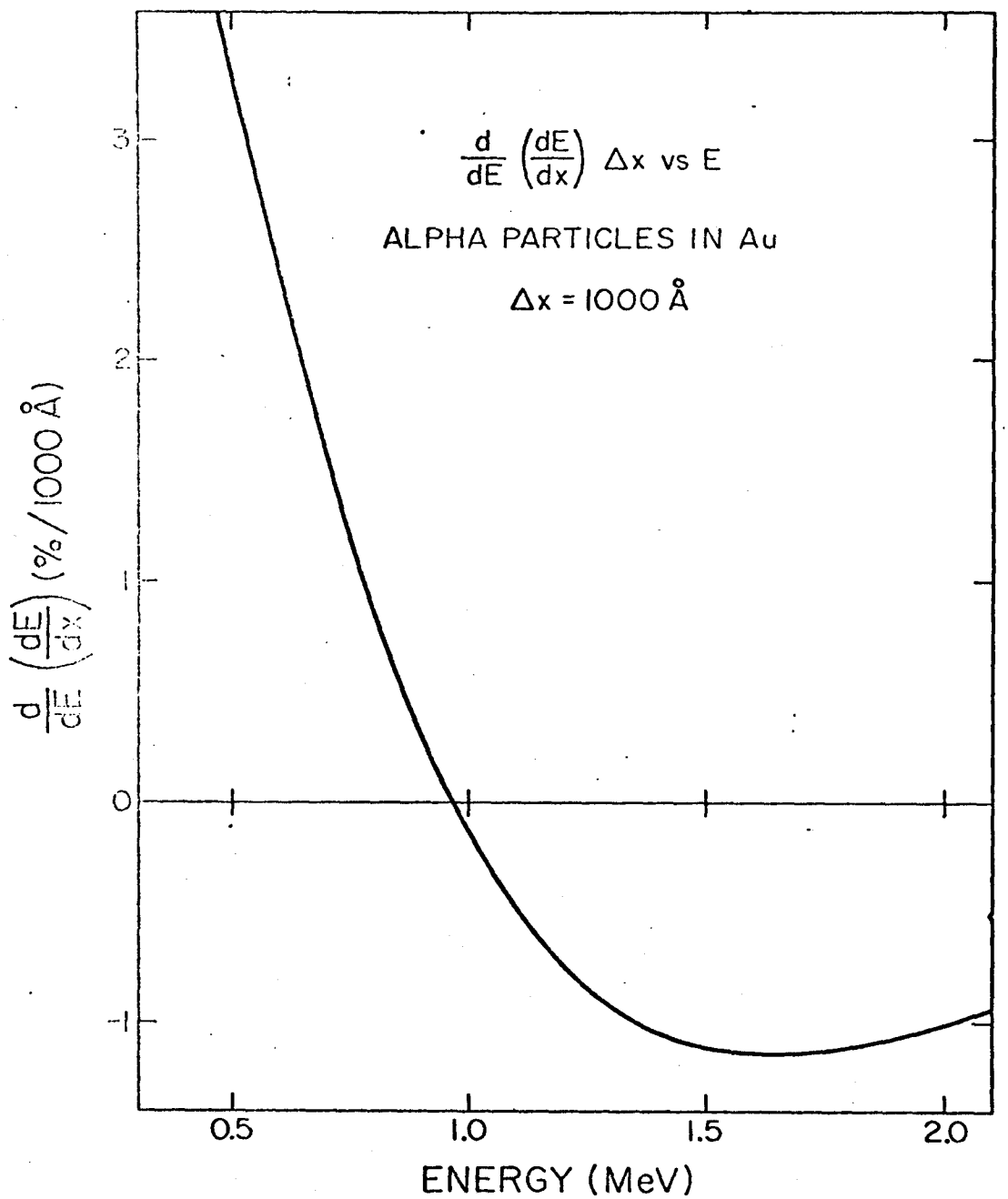
$\frac{d}{dE}\left(\frac{dE}{dx}\right)\Delta x$ vs E
ALPHA PARTICLES IN Au
Δx = 1000 Å
$\frac{d}{dE}\left(\frac{dE}{dx}\right)$ (%/1000 Å)
3
2
1
0
-1
0.5
1.0
1.5
2.0
ENERGY (MeV)

Figure 3.4

where δE_{IA} and δE_{IB} are the energy widths at the interface that correspond to a detected δE. The ratio $\delta E_{IA}/\delta E_{IB}$ represents a correction to Equation 3.7, the intuitive expression for the yield ratio. This correction to the thick target expression in a two-layered structure is

$$\frac{\delta E_{IA}}{\delta E_{IB}} = \frac{1 + \varepsilon_A'(\bar{E}_A)\cdot N_A \cdot t_A}{1 + \varepsilon_A'(\bar{E}_B)\cdot N_A \cdot t_A} \simeq 1 + \{\varepsilon_A'(\bar{E}_A) - \varepsilon_A'(\bar{E}_B)\}\cdot N_A \cdot t_A \qquad (3.21)$$

where N_A is the atomic number density of A, t_A is the outward path length through A and ε_A' is the derivative of the stopping cross section of A. The only difference between δE_{IA} and δE_{IB} is that ε_A' is evaluated at two different energies, $\bar{E}_A$ and $\bar{E}_B$, the two different "mean" energies of the particles on the outgoing path.

From Figure 3.4, it can be seen that the correction is small when $\bar{E}_A$ and $\bar{E}_B$ are both above 1.5 MeV since ε_A' is approximately constant above 1.5 MeV(Au is almost a worst case example for estimating this correction; ε' is approximately constant down to lower energies for most other materials). Obviously, when A and B are of similar mass, then $\bar{E}_A \simeq \bar{E}_B$, and this correction is again very small. Conversely, this effect can become significant when the difference in the kinematic factors K_A and K_B is large.

(b) Exact Solution. As a part of an effort to analyze the depth distribution of the elements in alloys of continuously varying composition, Brice(1973) has derived a mathematically exact solution for the thick target yield. This section presents an extension of Brice's formalism to show that it too results in a thickness dependence for the yield ratio that, to first order, is the same as that derived above. Just as the previous section produced a linearized estimate of this effect, this section simplifies Brice's exact solution to produce the same linearized solution.

Referring once again to Figure 3.3, we rewrite Brice's Equation 5 in our notation to define a function $x_2(E_1,E_3)$ through an integral equation

$$x_2(E_1,E_3) = \cos\theta_{out}\cdot\int_{E_3}^{E_1} dE'/S[E', x_2(E',E_3)] \quad (3.22)$$

where $S[E', x_2(E', E_3)]$ is the stopping power(dE/dx) for the outward bound particle at depth x_2 in the target and for an exit energy of E_3. Referring again to Figure 3.3, $S[E_1, x(E_1, E_3)]$ is the stopping power for the particle just after it has scattered at depth x. The functional form for x_2 is defined to allow for different values of E_1 that would correspond to different depths in the target. The spatial dependence of S was included by Brice to allow for smooth variations in the sample composition. This expression is an exact statement of the relation of the depth in the target, the energy of the exiting particle after scattering at that depth, and the final detected energy.

Relating the energy loss immediately after scattering δE_1 to the observed energy loss δE only requires some simple differential analysis. Taking the differential of x_2 while allowing both E_1 and E_3 to vary gives

$$dx_2 = \cos\theta_{out} \cdot \{ \frac{dE_1}{S[E_1, x_2(E_1,E_2)]} - \frac{dE_3}{S[E_3, x_2(E_3,E_3)]} + dE_3 \cdot \int_{E_3}^{E_1} dE' \cdot \frac{\partial}{\partial E_3} [\frac{1}{S[E', x_2(E',E_3)]}] \} . \tag{3.23}$$

If $x_2 = x$ is a constant, this expression simplifies to

$$\left.\frac{\partial E_1}{\partial E_3}\right|_x = \frac{S[E_1,x]}{S[E_3,0]} - S[E_1,x] \cdot \int_{E_3}^{E_1} dE' \cdot \frac{\partial}{\partial E_3} \{ \frac{1}{S[E', x(E',E_3)]} \} \tag{3.24}$$

where it has been noted that $x_2(E_3,E_3) = 0$.

Now consider the case of a two-layered structure of A on B , and let x be the depth to the interface between the two layers. For the ions scattered from A near the interface, the appropriate equation is just

$$\frac{\partial E_{1A}}{\partial E_{3A}} = \frac{S_A[E_{1A},x]}{S_A[E_{3A},0]} - S_A[E_{1A},x] \cdot \int_{E_{3A}}^{E_{1A}} dE' \cdot \frac{\partial}{\partial E_{3A}} \{ \frac{1}{S_A[E', x(E',E_{3A})]} \} \tag{3.25}$$

where the subscripts have been added where appropriate. Since the A layer is of uniform composition, dE/dx is a slowly varying function

of energy and the integrand will be small. Dropping this term simplifies the expression to

$$\frac{\partial E_{1A}}{\partial E_{3A}} \simeq \frac{S_A[E_{1A},x]}{S_A[E_{3A},x]} = 1 + \frac{S_A[E_{1A},x] - S_A[E_{3A},0]}{S_A[E_{3A},0]} . \tag{3.26}$$

The second term in the expression can be expanded to first order as

$$\frac{S_A[E_{1A},x] - S_A[E_{3A},0]}{S_A[E_{3A},0]} = \frac{S_A' \cdot \{E_{1A}-E_{3A}\}}{S_A[E_{3A},0]} \tag{3.27}$$

where S_A' is the derivative of S_A with respect to the particle energy evaluated at some appropriate energy between E_{1A} and E_{3A}. By noting that, again to first order,

$$x = \frac{E_{1A} - E_{3A}}{S[E_{3A},0]} \tag{3.28}$$

and realizing that from Equation 3.4 it follows that $S_A' = N\varepsilon_A'$, the expression in Equation 3.26 can be rewritten as

$$\frac{\partial E_{1A}}{\partial E_{3A}} \simeq 1 + \varepsilon_A'(\bar{E}_{3A}) \cdot N \cdot x \tag{3.29}$$

which is similar to Equation 3.19.

Solving for scattering from the B layer as evaluated at the interface will give a similar expression,

$$\frac{\partial E_{1B}}{\partial E_{3B}} = 1 + \varepsilon'_A(\bar{E}_{3B})\cdot N \cdot x \qquad (3.30)$$

since the only difference in the two cases is the energy of the emerging particle. Since the detected energy width is necessarily the same for both elements, i. e., $\delta E_{3A} = \delta E_{3B}$, the ratio of the effective energy widths at the interior interface is the same as Equation 3.21.

(c) Experimental Verification. The effect of the energy loss on the outgoing path was investigated by measuring the yield ratio of gold on aluminum as a function of the thickness of the gold layer. This pair was chosen to maximize the differences in the kinematic factors K_{Au} and K_{Al} , which maximizes the difference in the energy of the outward going particle. This then made the yield ratio depend measurably on the Au film thickness.

Measurements were performed on samples of Au-on-Al on thermally oxidized silicon substrates and Au-on-Al on carbon substrates. The effective thickness of the Au film was varied by changing both the actual Au film thickness and the orientation of the sample with respect to the ion scattering geometry. The use of the carbon substrate allowed a verification of the purity of the Al and Au films while a comparison of the results on the two substrates tested the reproducibility of the yield ratio. Although the background for the Al signal increases with the Au film thickness, tilting these samples is known to disproportionately increase this background(Chu, 1973) and it therefore tests

Figure 3.5 A backscattering spectrum of a two-layered target of Au on top of Al on a carbon substrate. The method of determining the heights at the interface, including the background subtraction procedure, is illustrated in this example.

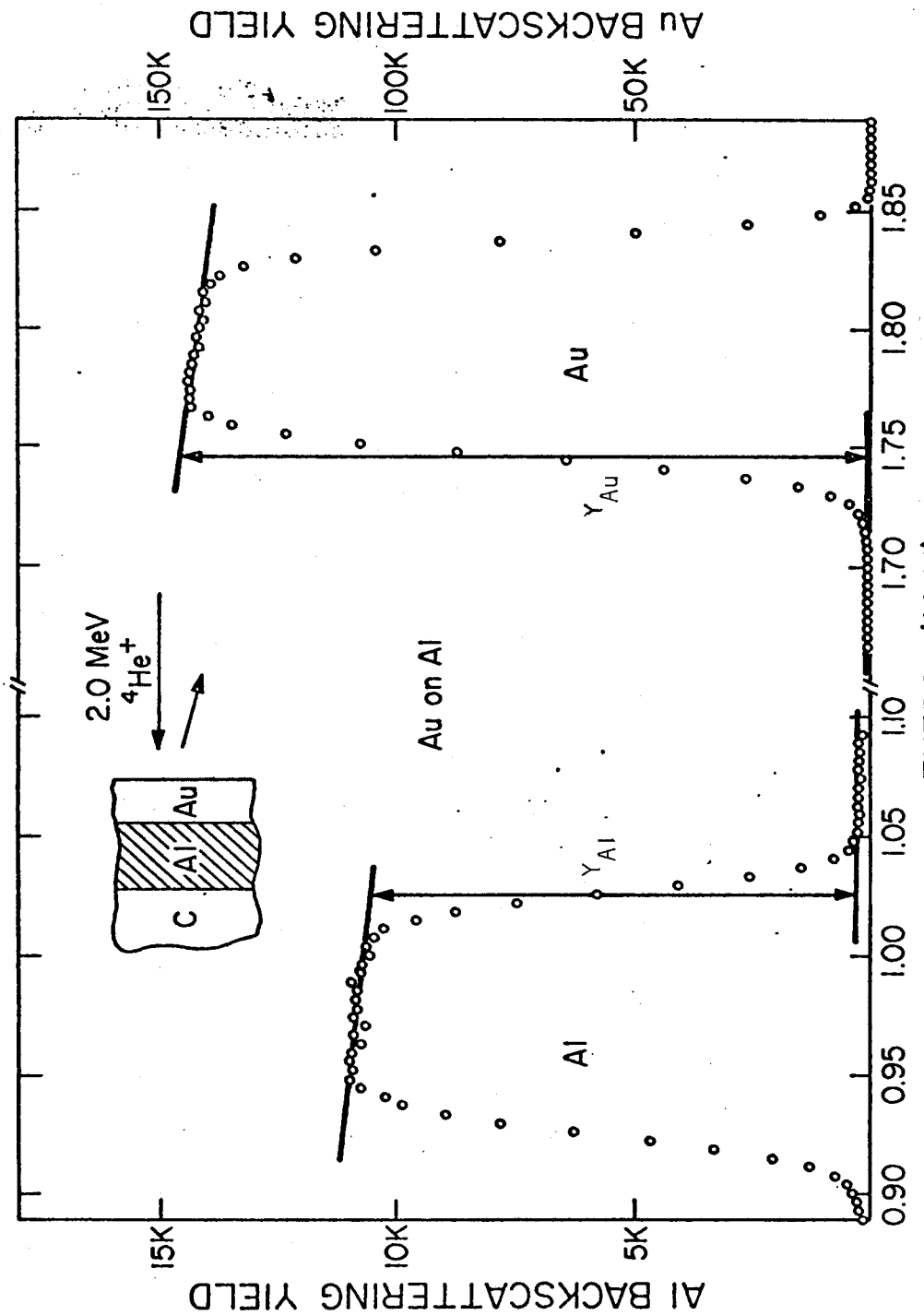
Au BACKSCATTERING YIELD
150K
100K
50K
Au
Y_{Au}
2.0 MeV
$^4He^+$
Au on Al
Au
Al
C
Y_{Al}
Al
15K
10K
5K
Al BACKSCATTERING YIELD
0.90
0.95
1.00
1.05
1.10
1.70
1.75
1.80
1.85
ENERGY (MeV)

Figure 3.5

the accuracy and reproducibility of the background subtraction procedure.

A representative backscattering spectrum of Au-on-Al on a carbon substrate is shown in Figure 3.5. This shows the typical statistical precision used in these measurements. Also illustrated are the methods used to determine the appropriate signal height ratio and the background subtraction method.

The results of a series of these measurements are shown in Figure 3.6 with the yield ratio plotted as a function of the effective Au film thickness as determined by the width of the Au signal. The ratio clearly depends on the Au thickness and it is independent of both the choice of the substrate and the orientation of the sample(after allowing for the increased effective Au thickness). The solid line shown in the figure is the calculated thickness dependence using the Al stopping cross section of Chu and Powers(1969) and the Au stopping cross section of Lin, Olson and Powers(1973) in the program described in Appendix A. The dashed line was drawn by increasing these calculated ratios by about 5%. The errors shown in the measured ratios are primarily due to uncertainties in the Al signal height caused by the finite thickness of the Al films, energy straggling and the background from the Au signal.

These measurements establish the existence of the difference in the effective energy width at the detector and inside the target, as predicted in the previous two sections. The 5% difference between the solid and dashed lines suggests that there is a 5% relative error in the stopping cross sections used in the calculations; this is within the sum of the estimated errors in the two stopping cross section values.

Figure 3.6 The yield ratio for Au on Al as a function of the Au film thickness. The solid line represents the ratios calculated using the stopping cross section values of Lin et al(1973) and Chu and Powers(1969). The dashed line was drawn by increasing these ratios by about 5%.

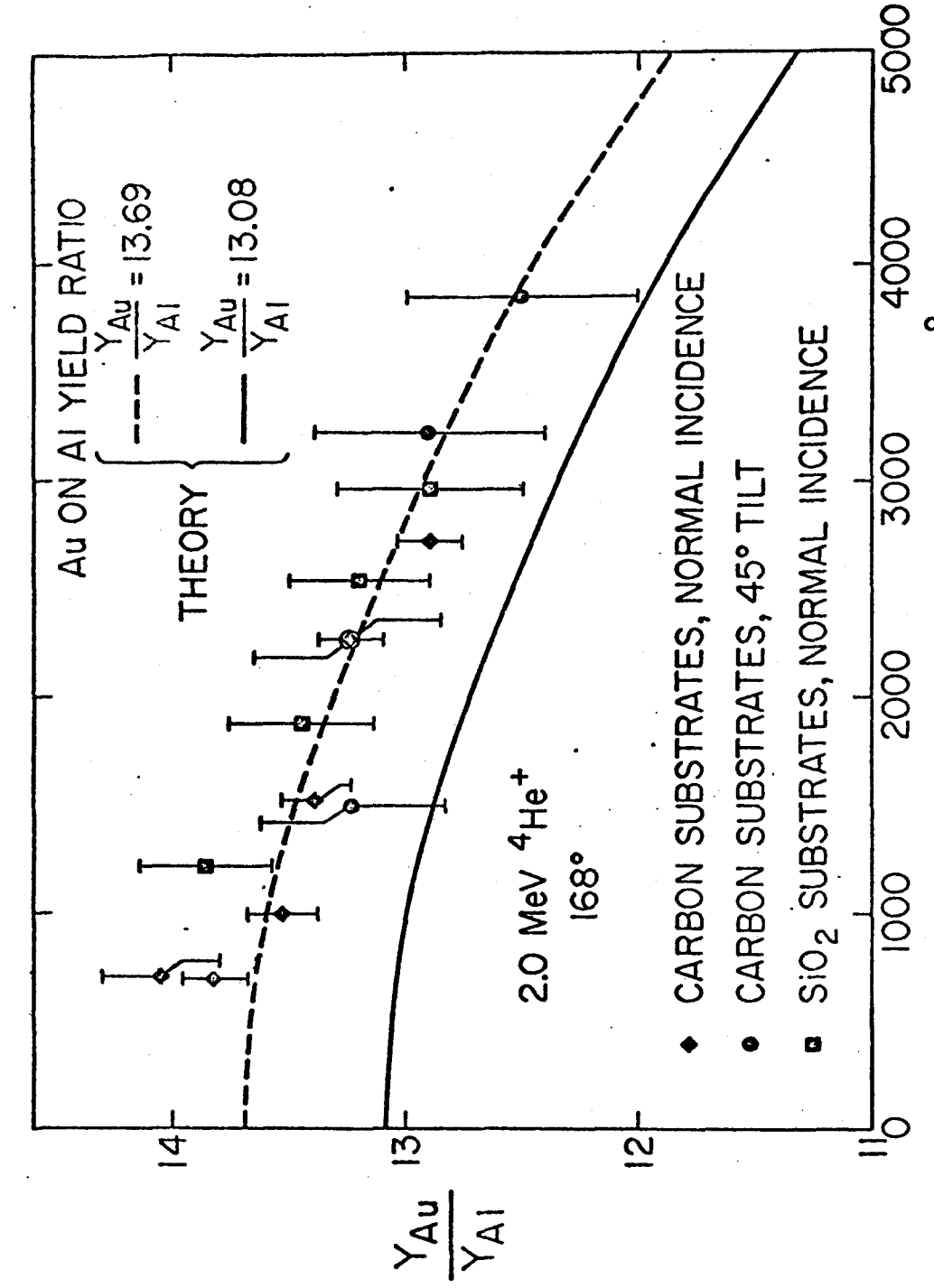
Au ON Al YIELD RATIO
$\frac{Y_{Au}}{Y_{Al}}$ = 13.69
THEORY
$\frac{Y_{Au}}{Y_{Al}}$ = 13.08
2.0 MeV $^4He^+$
168°
CARBON SUBSTRATES, NORMAL INCIDENCE
CARBON SUBSTRATES, 45° TILT
SiO_2 SUBSTRATES, NORMAL INCIDENCE
$\frac{Y_{Au}}{Y_{Al}}$
SURFACE Au THICKNESS (Å)
14
13
12
11
0
1000
2000
3000
4000
5000

Figure 3.6

In the context of the Bragg's rule experiments, the real importance of this section is that it demonstrates that the measured yield ratio from a two-layered structure is accurately given by Equation 3.7 in most cases and that the corrections to this expression are small. In the worst-case example of Au-on-Al, the correction for a 4000 Å thick gold layer on the aluminum is less than 8%. The correction will be much smaller when the elements in the two layers are of similar mass, as in the case of layers of aluminum and silicon.

3.4 Bragg's Rule in Solid Compounds

3.4.1 The One-Spectrum Approach

The simplest way of exploiting the two-layered approach to measuring the yield ratio is just to compare the signal yields from an element in a compound and from the same element in its pure form. This ratio is given by Equation 3.10 and it should be possible to calculate the required $[\varepsilon]$-factors by taking the stopping cross section values available in the literature.

The ineffectiveness of this approach can be appreciated by comparing theoretically calculated yield ratios with the experimentally measured ratios, as shown in Figures 3.7 and 3.8. The theoretical spectra were calculated using the Al and Fe stopping cross sections of Chu and Powers(1969) and the oxygen stopping cross section of Bourland, Chu and Powers(1971) in the program described in Appendix A. Figure 3.7 shows a comparison of the theoretical and experimental yield ratios at three incident energies for a sample of α-Fe_2O_3 on Fe. In this case, there is apparently good agreement between the predicted and measured yield ratios; any errors are less than the 5% uncertainty in the relative values of the stopping cross sections. A similar comparison for a self-supporting target of Al on γ-Al_2O_3 is shown in Figure 3.8; the disagreement is beyond the sum of the assigned errors in the two stopping cross sections used in the calculations.

The discrepancy in the aluminum oxide case is primarily due to the errors in the stopping cross sections used to produce the calculated spectra. In general, the 3-5% uncertainty in the measured stopping

Figure 3.7 A comparison of the theoretical and experimental spectra for α-Fe_2O_3 on pure Fe at 2.0, 1.5 and 1.0 MeV. The theoretical spectra are based on the stopping cross section values of Chu and Powers(1969) and Bourland et al(1971). The calculated and experimental yield ratios agree to within the uncertainties in the stopping cross sections used in the calculations.

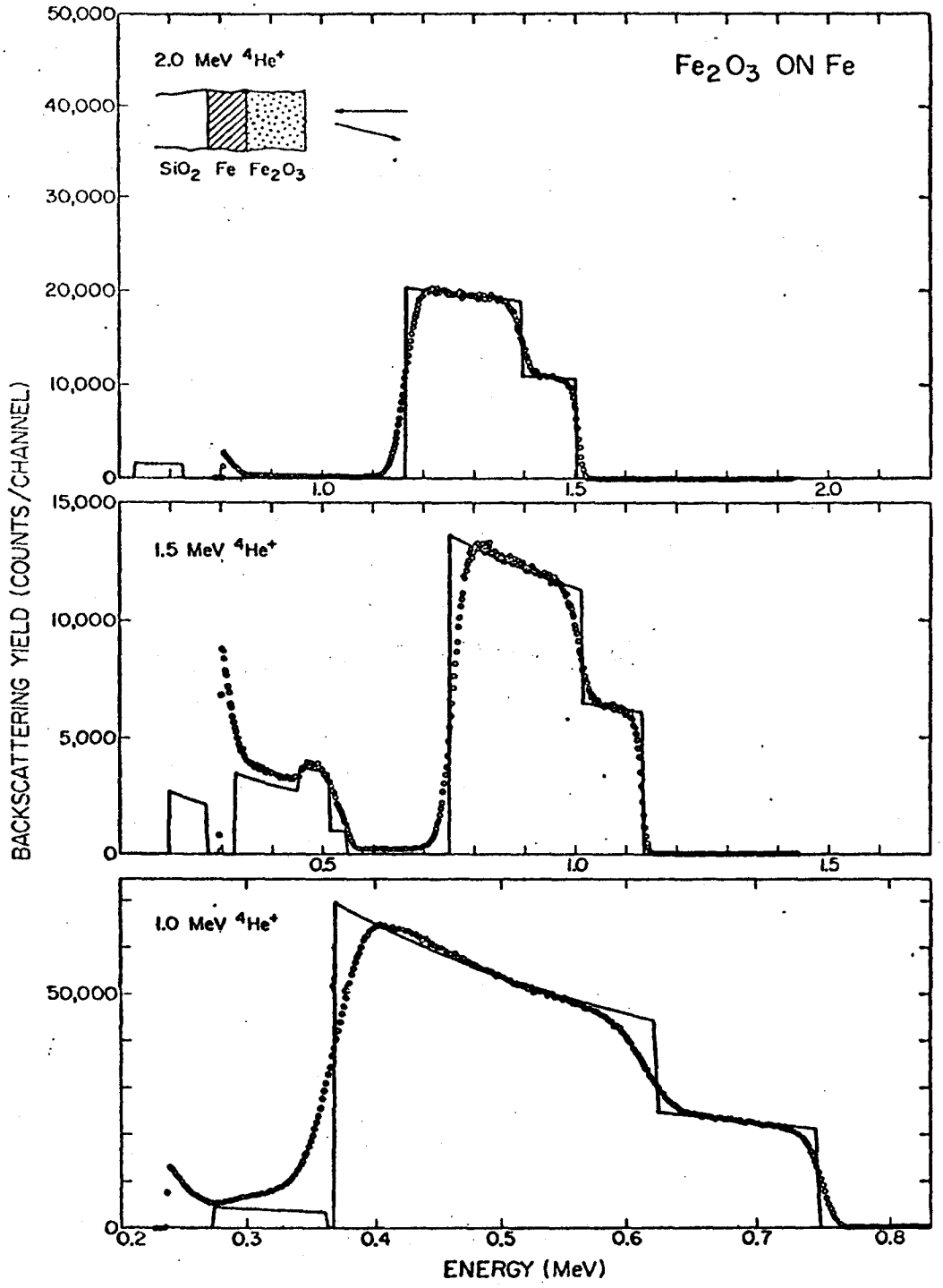
2.0 MeV $^4He^+$
Fe_2O_3 ON Fe
SiO_2 Fe Fe_2O_3
1.5 MeV $^4He^+$
1.0 MeV $^4He^+$
BACKSCATTERING YIELD (COUNTS/CHANNEL)
ENERGY (MeV)

Figure 3.7

Figure 3.8 A comparison of the theoretical and experimental spectra for Al on a self-supporting Al_2O_3 film at 2.0, 1.5 and 1.0 MeV. The calculated spectra are based on the stopping cross section values of Chu and Powers(1969) and Bourland et al(1971). The disagreement in the calculated and experimental yield ratios suggests a relative error in the two stopping cross sections of as much as 20%, assuming Bragg's rule is valid.

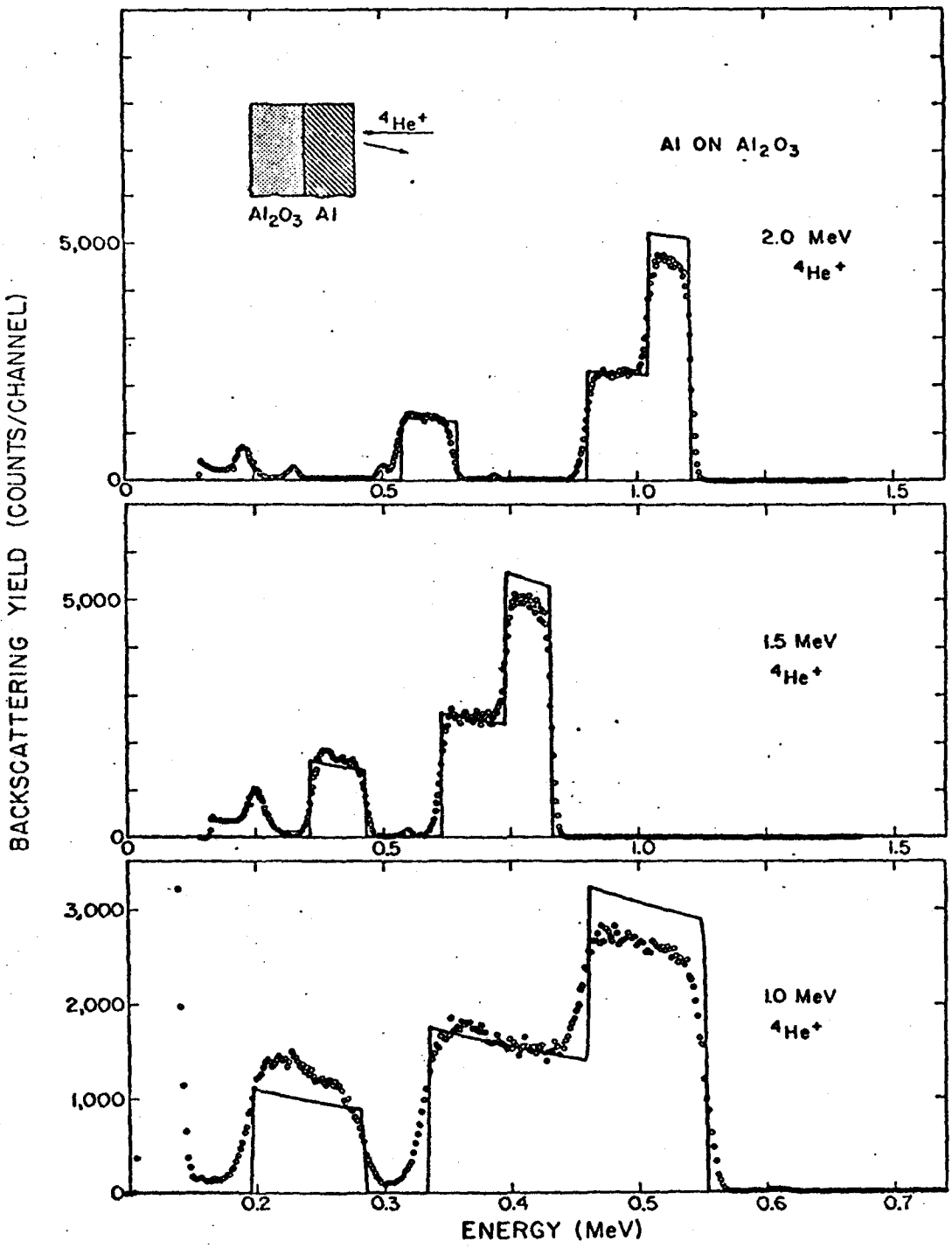
BACKSCATTERING YIELD (COUNTS/CHANNEL)
$^4He^+$
Al_2O_3 Al
Al ON Al_2O_3
2.0 MeV
$^4He^+$
1.5 MeV
$^4He^+$
1.0 MeV
$^4He^+$
5,000
0
3,000
2,000
1,000
0.5
1.0
1.5
0.2
0.3
0.4
0.6
0.7
ENERGY (MeV)

Figure 3.8

cross sections in solids and the 1-3% estimated error for the stopping power of gases limit the sensitivity of this approach to 4-6%. This, of course, does not allow for the possibility that there may be a systematic error in one of the two approaches used to measure these stopping cross sections. The following section describes an experiment in which the verification of Bragg's rule is divorced from this unfortunate dependence on absolute stopping cross section values.

3.4.2 The Nearly Numberless Spectra Approach

(a) Concepts. The whole motivation for developing the methods of this chapter was to find a way of testing Bragg's rule in those targets in which the approach described in the previous chapter is, for one reason or another, inapplicable. The present approach will be applied to the case of the binary dielectric compounds. Although this procedure is more generally applicable, five particular oxides have been chosen to illustrate the procedure and to test the validity of Bragg's rule in these oxides for 1-2 MeV helium ions.

It is difficult to apply either the approach of the previous chapter or the two-spectra approach of the next section[3.4.3] because one of the elements, oxygen, is not conveniently available as an elemental solid target. However, the present method can be used to compare the contributions of oxygen to the stopping in several oxides. Bragg's rule will then require that this contribution be the same in all of the compounds.

In the present experiment, the five oxides used were MgO, Al_2O_3, SiO_2, α-Fe_2O_3 and Fe_3O_4. In this case, a determination of the four

stopping cross section ratios Al-Mg, Al-Si, Al-Fe and Al-O would be sufficient to determine the allowed stopping cross section ratios for all other combinations. The Al-Mg, Al-Si and Al-Fe ratios would be determined from samples of the pure metals(where silicon has been generically included among the metals). The Al-O ratio in this experiment could be determined by measuring the Al-Al_2O_3 yield ratio. The test of Bragg's rule then consists of determining the Mg-O, Si-O and Fe-O stopping cross section ratios from MgO, SiO_2, α-Fe_2O_3 and Fe_3O_4.

This example constitutes a system of five unknown quantities, the absolute stopping cross sections of the five elements. The use of the stopping cross section ratios reduces the complexity of this example to only four unknowns. There are over ten ways of pairing these four metals with each other and with their oxides. Since Bragg's rule asserts linearity, the yield ratio measurements from these pairings define at least ten linear relationships between these four unknowns. The existence of a unique solution for this overdetermined system is necessary for the validity of Bragg additivity.

This procedure requires that four assumptions be satisfied to establish the existence of a solution to the overdetermined system. The assumption that we believe we are testing is the applicability of Bragg's rule of linear additivity of elemental stopping cross sections to compounds. A second, and presumably safe for these elements, assumption is that the scattering cross section of backscattered 2 MeV ^4He ions can be accurately calculated by using the Rutherford formula (Ziegler and Baglin, 1974). Thirdly, the conversion from the backscattering $[\varepsilon]$-factors (Equation 3.3) to the stopping cross section at

the incident particle energy assumes that the relative energy dependence of the stopping cross section, without reference to the absolute value, is known for each element. Finally, the composition of the targets must be known. Although it is possible that two or more of these assumptions may fail simultaneously, producing a cancellation of errors, this is highly improbable. Self-consistency is taken as prima facie evidence that all of these conditions have been satisfied.

(b) Experimental Considerations. The target material can be amorphous, polycrystalline, textured or single crystal. In the first two cases, the thick target yield in a backscattering experiment should be independent of the orientation of the sample and no special precautions are required to insure a valid yield measurement. The samples in which both sample layers were assumed to be amorphous or polycrystalline were mounted in a sample holder with orthogonal translational and azimuthal position control. Measurements were made with stationary targets and with the incoming beam at normal incidence.

Since a preferred crystal grain orientation in a textured sample or a single crystal target could result in significant channeling of the incoming beam, special care must be taken to avoid anomalous yield measurements from these targets. When a sample was suspected of having a layer of this type, it was mounted on a two-axis goniometer. During the measurement the sample would be continually rotated around its polar axis while the azimuthal angle was varied in 1/2° steps from 5° to 7°. This results in a thick target yield that represents an average over several "random" crystalline directions.

(c) Sample Preparation and Measurements. The compounds used in this study were chosen from those that could a priori be assumed to be stoichiometric. Nevertheless, the composition of these samples was not blithely assumed to be known. With only one exception, each type of sample was produced in several different ways. Only the first example will be described in detail.

(i) Al-Al_2O_3. The Al_2O_3-on-Al yield ratio was measured using four different thicknesses of anodically formed Al_2O_3(presumably γ-Al_2O_3). The Al-on-Al_2O_3 yield ratio was measured using samples of Al deposited onto (0001) α-Al_2O_3(single crystal sapphire), (11$\bar{2}$0) α-Al_2O_3 and anodized γ-Al_2O_3.

The γ-Al_2O_3 was formed by anodizing commercial Al foil(supplied by the Reynolds Metal Company, Richmond, Va.) in an aqueous solution of $(NH_4)_2HC_6H_5O_7$ using current densities of less than 10 mA/cm^2. The stoichiometry of a film produced by this method was checked by Rutherford backscattering on a self-supporting 1500 Å film and the oxygen-to-aluminum ratio was found to be 1.53±0.05. The (0001) α-Al_2O_3 was supplied by Union Carbide and the (11$\bar{2}$0) α-Al_2O_3 was supplied by Inselek, Inc.(Princeton, N. J.) as the substrate of epitaxially grown (111) silicon-on-sapphire.

The accuracy of the Al-Al_2O_3 yield ratio also depends on the purity of the Al layer. The purity of the evaporated Al was determined by simultaneously depositing an Al film onto carbon and aluminum foil substrates. The backscattering spectra taken with these samples are shown in Figure 3.9. The Al-on-C spectrum shows evidence of oxidation on both surfaces of the evaporated Al. There are no detectable

Figure 3.9 Purity tests of the evaporated Al films. The top half of the figure shows a backscattering spectrum for Al deposited onto a carbon substrate. This shows that there is a small amount of oxidation at the two surfaces of the Al film, but there is no evidence of any additional bulk impurities.

The bottom part of the figure shows the spectrum for Al deposited onto Al foil. The dip in the yield at about 975 keV is due to the native oxide on the Al foil. The match in the yields of the evaporated and bulk Al indicates that there are no significant undetected impurities.

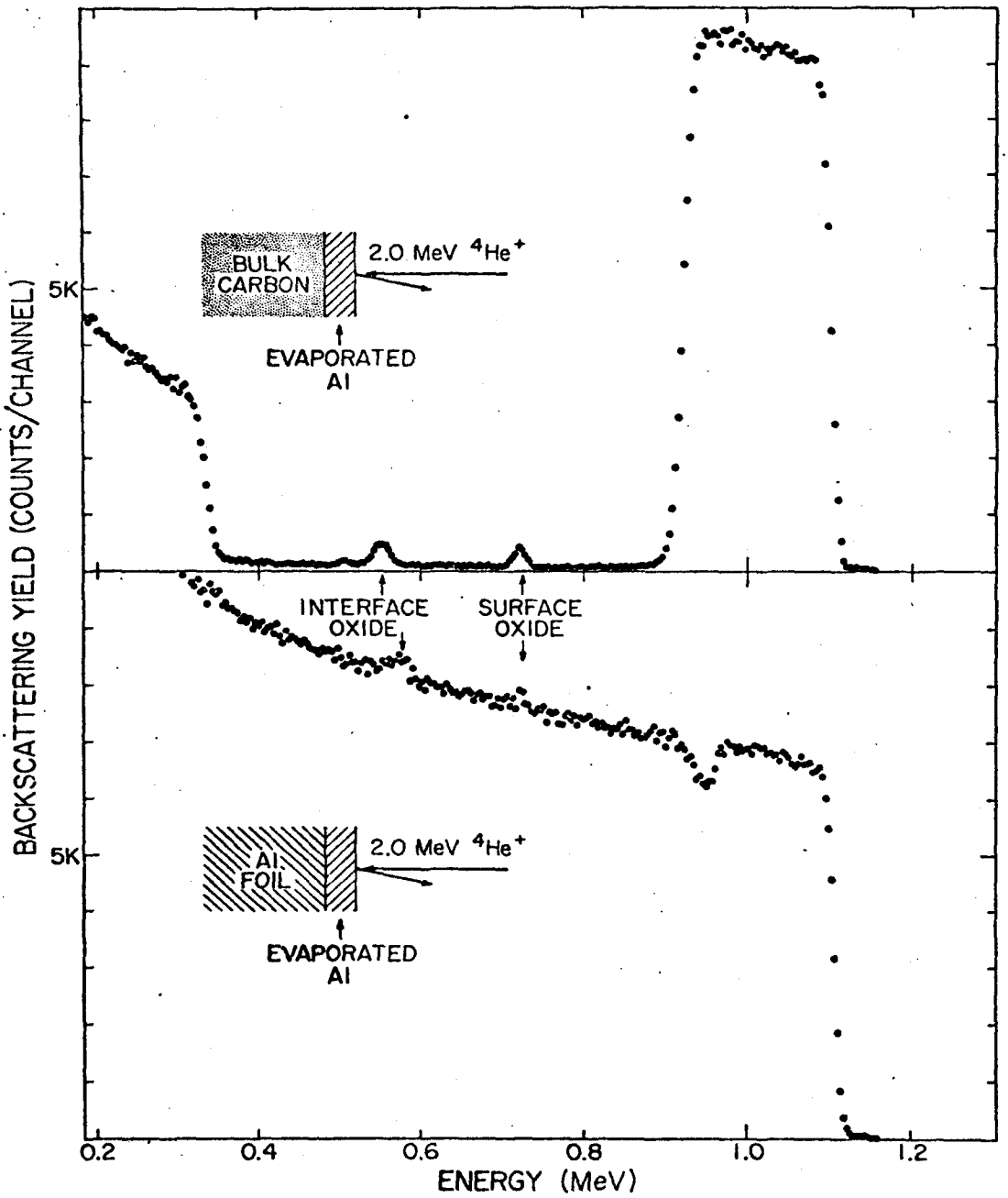
BACKSCATTERING YIELD (COUNTS/CHANNEL)
5K
5K
BULK CARBON
2.0 MeV $^4He^+$
EVAPORATED Al
INTERFACE OXIDE
SURFACE OXIDE
Al FOIL
2.0 MeV $^4He^+$
EVAPORATED Al
0.2
0.4
0.6
0.8
1.0
1.2
ENERGY (MeV)

Figure 3.9

impurities in the bulk of the deposited material. The Al-on-Al foil spectrum shows that the backscattering yields of the two layers are identical. The dip is due to the native oxide on the Al foil. This shows that there are no significant impurities in the film since the presence of impurities in the evaporated Al would be indicated by a lower backscattering yield from the deposited layer, just as the interface is marked by the dip due to the oxide on the surface of the foil. The impurity content of the Al foil is assumed to be insignificant.

The Al-Al_2O_3 yield ratios as determined from seven samples as described above were reproducible to within better than 1%. The repeatability of the measurements is encouraging evidence both that the method used in this experiment is valid and that all the samples are stoichiometric Al_2O_3.

(ii) Si-SiO_2. The SiO_2-on-Si yield ratio was determined for two thicknesses of thermally grown SiO_2 on single crystal Si. The Si-on-SiO_2 ratio was measured for amorphous Si deposited onto fused quartz, AT-cut quartz and thermally grown SiO_2.

Thermally grown SiO_2 has been extensively investigated and it is believed that any deviations from stoichiometry are below the sensitivity of most experiments. The fused quartz, supplied by Amersil, Inc. (Hillside, N. J.) is claimed to have less than 100 ppm impurities. The AT-cut single crystal quartz was removed from an electrically active quartz crystal resonator.

The purity of the evaporated Si was tested by simultaneously depositing the Si onto Si and C substrates. Despite a small amount of

oxygen contamination of a few per cent evident in the Si-on-C sample, the backscattering yield from the evaporated Si matched the yield from the single crystal Si to within better than ±1/2%. The single crystal silicon is assumed to be pure.

The ratios of the yields from the Si and SiO_2 layers were reproducible to within ±1/2% in all of these samples.

(iii) $Fe-Fe_2O_3-Fe_3O_4$. The compositions of the two iron oxides were inferred from the magnetic, electrical, optical and crystallographic properties. The sample preparation techniques and the verification of the properties of the oxides will be described in Part II.

The purity of the Fe films was established by depositing Fe onto a carbon substrate and using backscattering to show that there are no detectable impurities. Measurements using x-ray fluorescence also showed no evidence of measurable amounts of similar mass impurities such as nickel or cobalt.

The reproducibility of the $Fe-Fe_2O_3$ and $Fe-Fe_3O_4$ ratios was better than ±1%. The two ratios are also consistent with each other within ±1%.

(iv) Mg-MgO. The Mg-MgO ratio was determined for only one sample. The MgO is a single crystal (100) wafer supplied by Semi-Elements(Saxonburg, Pa.). The Mg film was evaporated from material of better than 99.9% purity in a vacuum of better than 10^{-6} Torr. The purity of the Mg films produced this way was not extensively tested, but there was no evidence of any significant impurities in any of the backscattering spectra.

(v) Al-Si. The Al-on-Si yield ratio was measured for Al deposited on single crystal (111) Si and on Si deposited on a carbon

substrate. The Si-on-Al ratio was determined using samples of Si deposited on Al foil and a deposited Al film. The measured ratios were within ±1% for all samples.

(vi) Fe-Al. The Fe-Al ratio was measured using Fe deposited onto Al foil and Al deposited onto a fim of Fe on a Si substrate. One sample of each type was measured and the two yield ratios were almost identical.

(vii) Fe-Si. The Fe-on-Si was measured with two different thicknesses of Fe deposited onto single crystal (111) Si. No measurements of the Si-on-Fe ratio were performed. The ratio was reproducible to better than ±1/2%.

(viii) Al-Mg. The Al-on-Mg ratio was determined from two samples with different thicknesses of Al deposited on Mg films on MgO substrates. The Mg-on-Al ratio was measured using a single sample of Mg deposited on a film of Al on a thermally oxidized silicon substrate. The measured ratios were the same within 2%.

(d) Results. A typical spectrum, for a sample of Al deposited on (0001) α-Al_2O_3, is shown in Figure 3.10. The data was taken using a beam current of 150 nA and a total dose of 500 μC. To avoid anomalous yields due to channeling effects, the sample was continually rotated about its polar axis and the azimuthal angle was changed from 5° to 7° in 1/2° steps at every 100 μC of incremental dose.

The yield ratio is determined by extrapolating the Al and Al_2O_3 plateaus to the point representing the interface between the two layers and taking the ratio of the projected yields. This procedure insures

Figure 3.10 Yield ratio measurements. The spectrum was taken by backscattering from a target of Al deposited onto (0001) α-Al_2O_3. The sample was rotated about a polar axis perpendicular to the plane of the sample while the azimuthal angle was varied during the measurement. The method of determining the yield ratios by projecting to the interface between the two layers is illustrated once again.

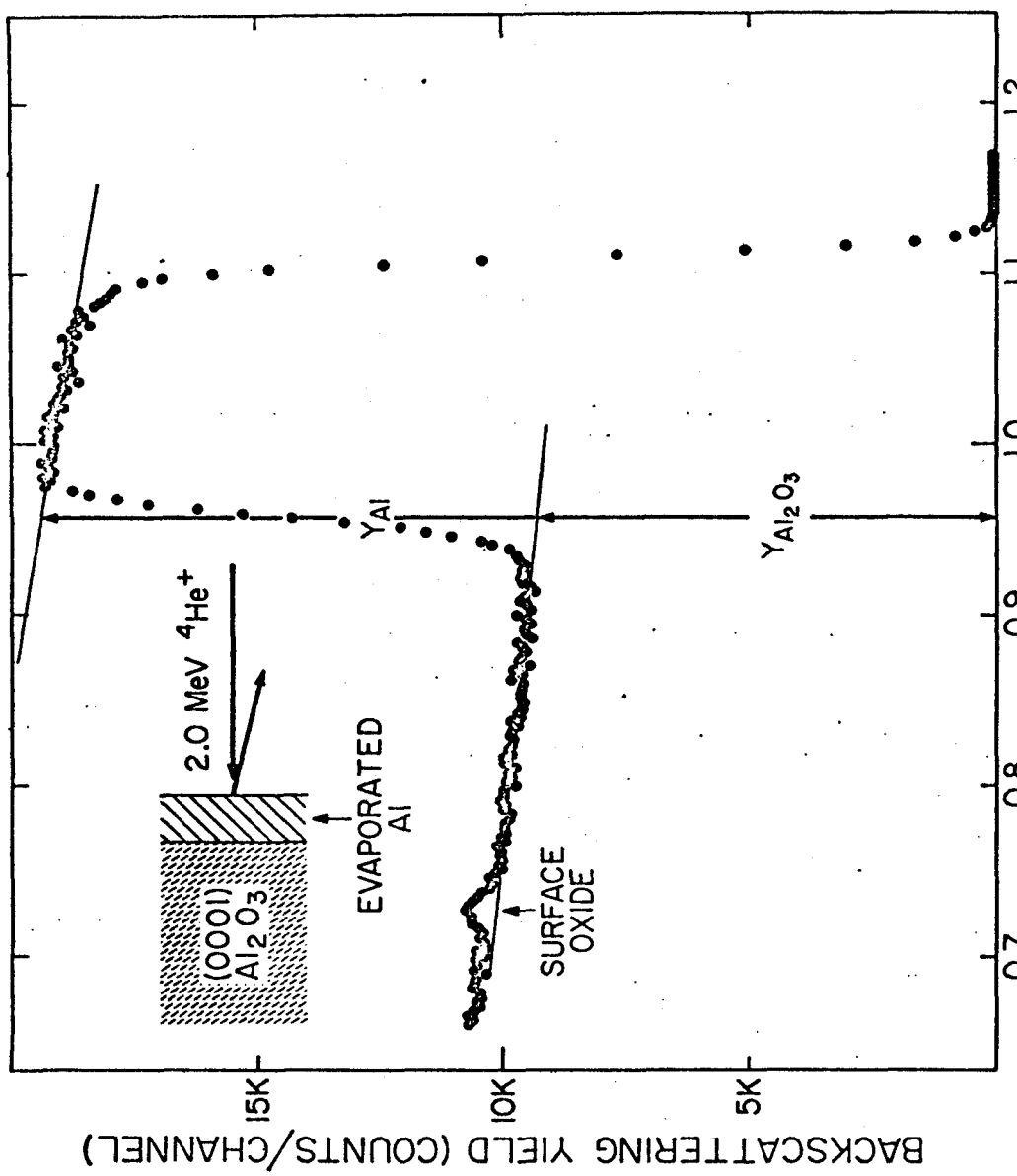
BACKSCATTERING YIELD (COUNTS/CHANNEL)
15K
10K
5K
0.7
0.8
0.9
1.0
1.1
1.2
ENERGY (MeV)
Y_{Al}
$Y_{Al_2O_3}$
2.0 MeV $^4He^+$
EVAPORATED Al
(0001) Al_2O_3
SURFACE OXIDE

Figure 3.10

that the backscattered particle yields are evaluated at the same incident particle energy. An example of the extrapolation procedure used for scattering from two dissimilar elements is shown in Figure 3.4.

Obviously, the accuracy of the yield ratio determination does not depend on the accurate measurement of the total ion fluence. This ratio also is not very sensitive to the scattering geometry and the absolute beam energy because errors of this type tend to cancel each other when ratios are taken. As discussed in section 3.3, the effect of the thickness of the surface layer on the yield ratio is negligible for these cases. The only parameters that plausibly affect the accuracy of the determination of this ratio are the composition of the two layers, the statistical fluctuations in the data, and the judgment of the investigator in estimating the yield levels.

The results of the yield ratio measurements are shown in Table 3.1. The number of samples used to determine each ratio and the reproducibility of the experimental ratios are also shown in the table. Since the Mg-MgO yield ratio was measured on only one sample, the tabulated uncertainty is an estimated value.

Note that the Al-Si, Al-Fe and Fe-Si ratios constitute all possible pairings of Al, Si and Fe. The self-consistency of these values is much better than could be expected from the uncertainties in each value. This supports the validity of the approach used in this experiment.

The yield ratios of the pure metals were used to determine the ratios of the stopping cross sections at 2.0 MeV. First, the ratios of the $[\varepsilon]$-factors was calculated according to Equation 3.13. The laboratory frame scattering cross sections were calculated using

Table 3.1

EXPERIMENTAL YIELD RATIOS

Sample Type	Number of Samples	Yield Ratio	Standard Deviation
Al/Mg	3	1.207	1.8 %
Si/Al	4	1.069	0.81%
Fe/Al	2	2.524	0.08%
Fe/Si	2	2.358	0.17%
Mg/MgO	1	1.703	(~1%)
Al/Al_2O_3	7	2.075	0.83%
Si/SiO_2	5	2.356	0.49%
Fe/Fe_2O_3	4	1.678	0.36%
Fe/Fe_3O_4	3	1.616	0.62%

The experimental yield ratios for 168° backscattering of 2 MeV ^4He ions from two-layered samples. The yield ratio is the yield of the first layer identified in the "Sample Type" column divided by the yield of the other layer. The standard deviation represents the experimental reproducibility of the measurement. The Mg-MgO ratio was measured only once and the tabulated uncertainty is an estimated value.

Darwin's formula(1914). The corrections to the center-of-mass Rutherford cross section for a few selected target masses are shown in Table 3.2. This correction is also shown as a function of the mass ratio of the incident particle and target nucleus in Figure 3.11.

The $[\varepsilon]$-factor ratios were then converted to stopping cross section ratios by inverting Equation 3.3. The energy dependence of the semi-empirical stopping cross sections of Ziegler and Chu(1973) were used to determine the appropriate $[\varepsilon]/\varepsilon$ ratio. The stopping cross section ratios, normalized to the value of silicon, are shown in Table 3.3. Also shown in the table for comparison are the ratios calculated from Ziegler and Chu's semi-empirical stopping cross sections. Although the stopping cross section ratios determined from the present yield ratio measurements are in significant disagreement with the semi-empirical values(especially when comparing Al and Si), these do not affect the present results. The present experiment is based on the self-consistency of all the yield ratios taken together and does not depend on any absolute determination of the stopping cross sections.

The metal/oxide yield ratios were used to determine the ratio of the stopping cross sections of the metal and the oxygen, assuming the validity of Bragg's rule. These ratios, calculated for the incident ion energy of 2.0 MeV, are shown in Table 3.4. These ratios were determined by first calculating the appropriate $[\varepsilon]$-factor according to Equation 3.12, such as $[\varepsilon]_O^{Al}/[\varepsilon]_{Al}^{Al}$. This was then converted to a stopping cross section ratio $\varepsilon_O/\varepsilon_{Al}$ by again inverting Equation 3.3 using the same set of semi-empirical stopping cross sections.

Table 3.2

LABORATORY FRAME CORRECTIONS TO THE CM

RUTHERFORD SCATTERING CROSS SECTION

Mass	$\theta_{lab}=172°$	$\theta_{lab}=168°$	$\theta_{lab}=164°$
6	0.3113272	0.3147143	0.3195132
7	0.4564539	0.4600852	0.4651968
9	0.6464355	0.6495306	0.6538567
10	0.7077985	0.7105394	0.7143627
11	0.7549605	0.7573739	0.7607355
12	0.7918316	0.7939568	0.7969136
14	0.8447374	0.8464012	0.8487123
16	0.8799741	0.8813001	0.8831400
19	0.9141084	0.9150844	0.9164375
20	0.9223163	0.9232050	0.9244366
23	0.9409759	0.9416612	0.9426105
24	0.9457261	0.9463586	0.9472346
27	0.9569938	0.9574994	0.9581994
28	0.9599806	0.9604521	0.9611050
31	0.9672913	0.9676788	0.9682153
35	0.9742952	0.9746014	0.9750252
37	0.9769836	0.9772583	0.9776385

This table gives the correction factor $F\{m,M;\theta_{lab}\}$ to the center-of-mass formula for the Rutherford scattering cross section, where

$$\sigma_{lab}(\theta) = F\{m,M;\theta\}\cdot\sigma_{cm}(\theta)$$

where the projectile mass m is assumed to be 4 amu.

Figure 3.11 Laboratory Frame Corrections to the CM Rutherford Scattering Cross section. This shows the magnitude of the corrections shown in Table 3.2. Note that in this case, the ordinate is not the function F as defined in the table caption, but instead, 1 - F . This was chosen to make it possible to see the small errors for very heavy target nuclei. Note that the error in using the CM cross section for scattering ^{4}He from ^{56}Fe is only around 1%.(note that the two horizontal scales are different: the lower scale is for helium backscattering; the upper scale is for the more general case of arbitrary mass ratios).

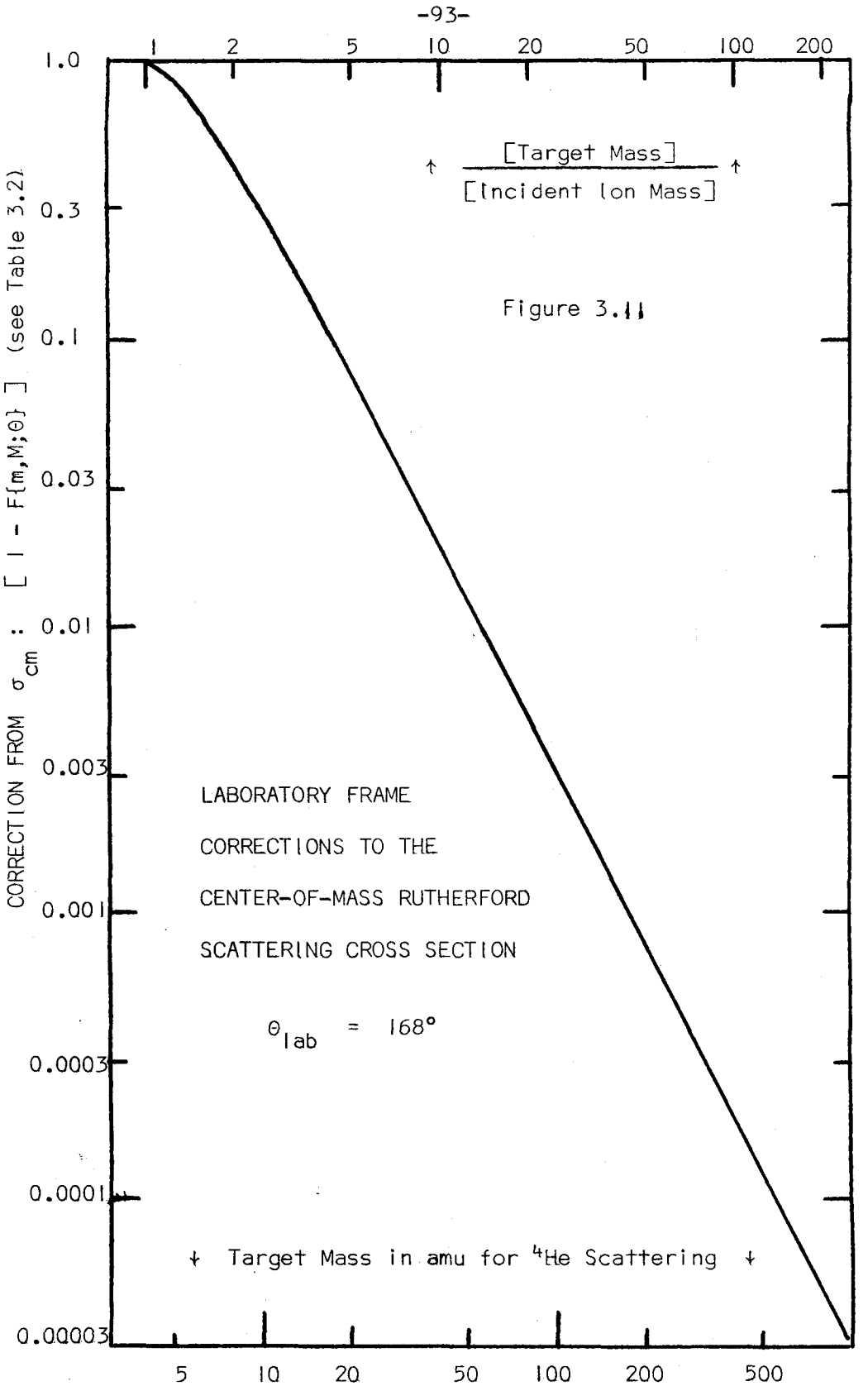
1
2
5
10
20
50
100
200
1.0
0.3
0.1
0.03
0.01
0.003
0.001
0.0003
0.0001
0.00003
5
10
20
50
100
200
500
↑ [Target Mass] / [Incident Ion Mass] ↑
CORRECTION FROM σ_{cm} : [1 - F{m,M;θ}] (see Table 3.2)
LABORATORY FRAME
CORRECTIONS TO THE
CENTER-OF-MASS RUTHERFORD
SCATTERING CROSS SECTION
θ_{lab} = 168°
↓ Target Mass in amu for ^{4}He Scattering ↓

Figure 3.11

Table 3.3

RELATIVE α-PARTICLE STOPPING CROSS SECTIONS

Metal →		Mg↓	Al↓	Si↓	Fe↓
$\frac{\varepsilon^{2.0\ MeV}_{metal}}{\varepsilon^{2.0\ MeV}_{silicon}}$ →	Present → Measurements	0.985	0.995	1.000	1.485
	Ziegler and Chu(1973) →	0.916	0.898	1.000	1.442
Discrepancies between present and tabulated values →		+7.5%	+10.8%	------	+3.0%

Relative stopping cross sections at 2.0 MeV. The top row identified the metal in the oxide. The first part give the ε-ratios based on the present yield ratio measurements on the pure metals, normalized to silicon. Below that are the

Table 3.3 caption(continued)

ratios calculated from the values given in Ziegler and Chu(1969). The bottom row gives the relative discrepancies between these two sets of values.

Table 3.4

RELATIVE STOPPING CROSS SECTIONS FOR SOLID OXYGEN

Metal→		Mg↓	Al↓	Si↓	Fe↓
$\frac{2x\varepsilon\{\text{'solid' oxygen}\}}{\varepsilon\{\text{metal}\}}$	→ 2.0 MeV	1.34 (3%)	1.33 (2%)	1.36 (1 1/2%)	0.90 (2%)

The ratios of twice the stopping cross section of "solid oxygen" to the stopping cross section of a metal were calculated from the yield ratios given in Table 3.1 using the procedures outlined in the text. The uncertainties in the values, shown parenthetically, were calculated by propagating the standard deviations shown in Table 3.1.

By combining the results of Tables 3.3 and 3.4, it is possible to calculate the relative contribution of an oxygen atom to the molecular stopping cross sections of the different oxides. If Bragg's rule is valid, this contribution in one oxide, e.g., Al_2O_3, must be the same as the contribution in all other oxides. The relative values of this contribution of oxygen to the molecular stopping cross sections are shown in Table 3.5 with the estimated error. The values have been normalized to an average value of unity to highlight the consistency of the oxygen stopping cross sections in these five oxides.

Since the absolute stopping cross sections of these five elements have been determined experimentally by several laboratories, the absolute value of this contribution to the molecular stopping cross section can be evaluated by using the ratios in Table 3.4 and the reported stopping cross sections for the metals. Recalling the wide variations in the metal/metal yield ratios when compared to some of these experimental values, it would not be expected that all of calculations would produce the same value. The results of these calculations, using the selected values of the pure metal stopping cross sections given in Table 3.7, are shown in Table 3.6 with the value reported for molecular O_2 in the gas phase included for comparison. The stopping cross sections thus obtained are systematically 6-22% lower than in gas phase.

Table 3.5

RELATIVE OXYGEN STOPPING CROSS SECTIONS

Oxide→	MgO ↓	Al_2O_3 ↓	SiO_2 ↓	α-Fe_2O_3 Fe_3O_4 ↓
$\frac{\varepsilon^{2.0\ MeV}_{oxygen}}{\langle\varepsilon^{2.0\ MeV}_{oxygen}\rangle_{av}}$ →	0.995 (3.4%)	0.989 (2.4%)	1.016 (2.0%)	0.999 (2.3%)

This shows the variation in the contribution of oxygen to the stopping in the five oxides. These have been calculated by using the relative stopping cross sections as shown in Tables 3.3 and 3.4. The values have been normalized to emphasize the existence of a unique contribution to the molecular stopping cross sections by the oxygen. The uncertainties, shown parenthetically, were calculated by propagating the standard deviations in the measurements shown in Table 3.1.

Table 3.6

CALCULATED ABSOLUTE VALUES FOR THE
STOPPING CROSS SECTION OF
"SOLID" OXYGEN

Metal →	Mg↓	Al↓	Si↓	Fe↓	O_2^*↓
$2 \cdot \varepsilon^{solid}_{oxygen}$ at 2.0 MeV† →	59	56	67	67	72
Difference from gaseous O_2 →	-18%	-22%	-7%	-6%	--

*The reference value for gaseous O_2 is from Bourland, Chu and Powers (1971).

†Stopping cross section values are all in units of [10^{-15} eV cm^2].

The absolute values of the oxygen stopping cross sections, calculated from the ratios shown in Table 3.4 and using the values shown in Table 3.7, show a systematic deviation from the reported value for gaseous O_2, which is included for comparison.

Table 3.7

REFERENCE STOPPING CROSS SECTIONS

Element →	O_2	Mg	Al	Si	Fe
ε(1.0 MeV) →	94	56	52	67	93
ε(1.5 MeV) →	83	50	47	58	85
ε(2.0 MeV) →	72	44	42	49	75
Reference →	*	†	†	§	†

All stopping cross sections are in units of [10^{-15} eV-cm^2] .

* Bourland, Chu and Powers(1971)

† Chu and Powers(1969)

§ Eisen et al(1972)

3.4.3 The Two-Spectra Approach

The two-spectra approach is based on the recognition that Bragg additivity only requires that the relative stopping cross sections be described by a linear relation. In a binary system, the ratio of the stopping cross sections can be determined from the ratio of the thick target yields of the pure elements, as indicated by Equation 3.13. This only requires that both elements are available in pure form as solid targets. An implicit assumption in this step is that the scattering cross sections of both elements are known. Just as in the previous section, this means that both must be accurately described by the classical Rutherford formula. The ratio of the stopping cross sections can also be determined by comparing the signal from one of the elements, usually the heavier of the two, with the signal from the same element in its pure form and then using Equation 3.12. This step assumes that the composition of the compound is known, and this is most readily accomplished by limiting the choice to binary compounds with narrow existence regions.

This particular approach is illustrated by the example of silicon carbide. This happens to be one of the few stoichiometric binary compounds in which the compound and both elements are readily available in a state that is suitable for performing a backscattering experiment (usually one or both of the elements in a II-VI or III-V compound is not easily made into a smooth thin film sample with a low vapor pressure; one alternative that does appear feasible is MgSi). The two spectra shown in Figure 3.12 are, on the top, for Si deposited onto pyrolytic carbon and, on the bottom, silicon deposited on single

Figure 3.12 The two spectra required to test Bragg's rule in SiC. Since both silicon and carbon are readily available as solids, the yield ratio from the Si-on-C target (top) should give the ratio of the stopping cross sections in the two elements. The yield ratio of the silicon signals from the Si-on-SiC target (bottom) should similarly give the ratio of the atomic stopping cross section of Si and the molecular stopping cross section of SiC. By assuming Bragg's rule, the stopping cross section ratio of Si and C can be determined independently from these two spectra. The validity of Bragg's rule demands that these two ratios be equal.

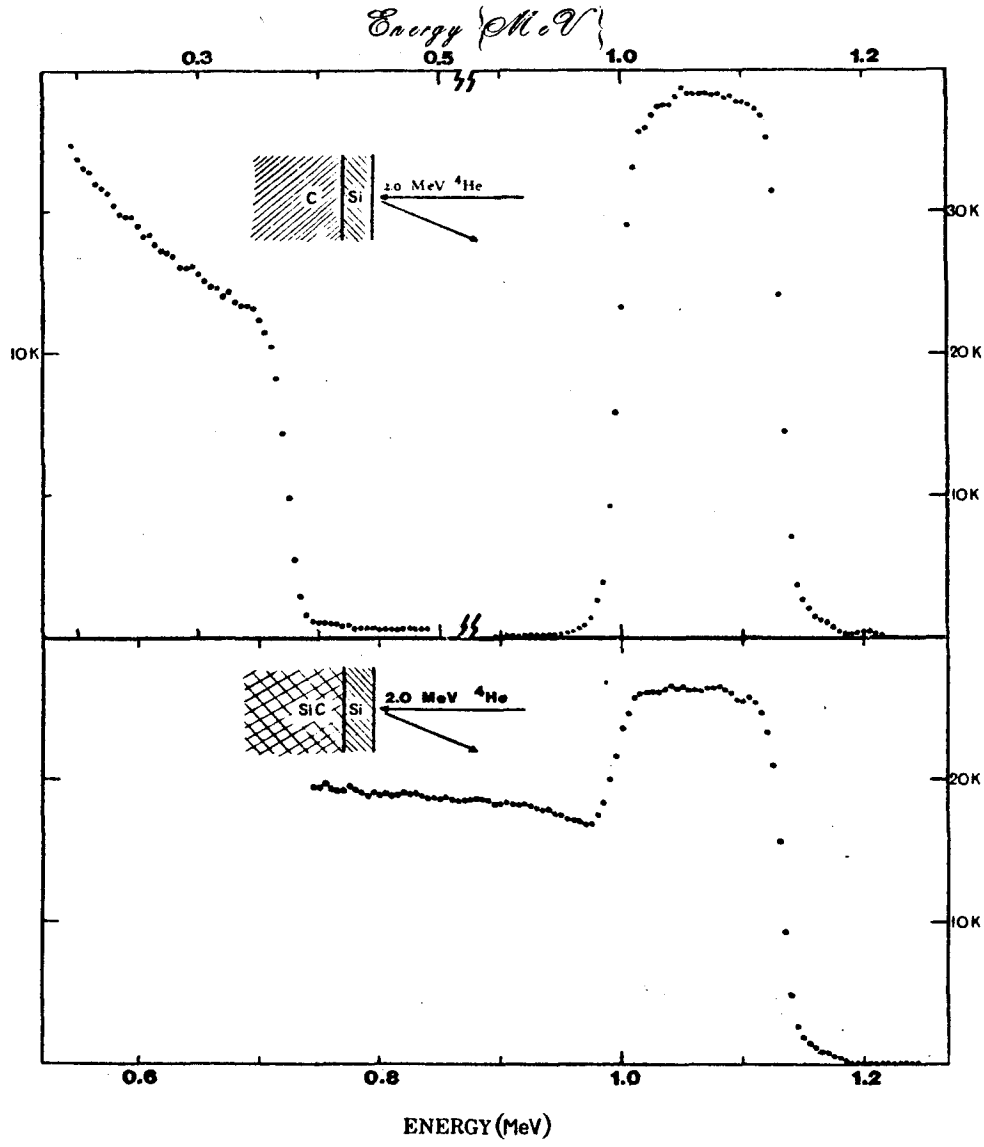
Energy (MeV)
0.3
0.5
1.0
1.2
C
Si
2.0 MeV 4He
30K
10K
20K
10K
SiC
Si
2.0 MeV 4He
20K
10K
0.6
0.8
1.0
1.2
ENERGY (MeV)

Figure 3.12

crystal, hexagonal SiC. Since the silicon carbide sample was a single crystal, the special precautions of 3.4.2(b) were taken.

The measured silicon-to-carbon yield ratio is 3.82. The measured ratio of the silicon signals in the pure silicon and the SiC is 1.53. Unfortunately, these two ratios are inconsistent with each other. The ratio of the Si and SiC signals, however, is in good agreement with the stopping cross sections of Lin, Olson and Powers(1973) for Si and Chu and Powers(1969) for C, assuming Bragg's rule is valid.

Although this discrepancy could reflect a breakdown in the applicability of Bragg's rule, there are several alternative explanations. The carbon used in this experiment was prepared by carbonizing a plastic at elevated temperatures; some hydrogen could be trapped in the carbon to contribute to the energy loss while remaining otherwise undetected. The would account for the low yield in the carbon signal observed in the top of Figure 3.11.

In addition, it is possible that the scattering cross section of the carbon nucleus is not accurately given by the Rutherford formula, even though there are no significant phase shifts in the scattered particle wavefunction below 2.5 MeV(Hill, 1953; Jones et al, 1962).

The origins of this disagreement were not actively pursued because this two-spectra approach is not of applicability to a great variety of sample targets. This approach has been only to illustrate that the convoluted argument of section 3.4.2 is not required in all cases.

3.5 Discussion

3.5.1 Experimental Approach

This chapter has described a self-consistent procedure for testing Bragg's rule that does not require the knowledge of any absolute stopping cross section values. Although the simple two-spectra approach was not successful in the case of SiC, this probably can be attributed either to a bad sample or to a non-Rutherford scattering cross section for carbon and it probably does not reflect a failure in the analytical approach. The technique was vindicated by the nearly numberless spectra approach, which was used to demonstrate that the contribution of oxygen to the molecular stopping cross section of five oxides for 1-2 MeV ^4He ions is independent of the cation element.

Although the method of testing Bragg's rule described here has been applied only to oxides, it can obviously be extended to all stoichiometric solid compounds. It is most useful for testing binary compound systems such as oxides or nitrides(Si_3N_4-AlN-BN), in which the normal phase of the one element common to all the compounds is not normally the solid phase. It can also be extended to test the reproducibility of the stopping cross sections of chemical radicals such as $(NO_3)^-$, $(SO_4)^=$, etc. The advantage of this test is that in its self-consistency or in its failure to achieve self-consistency, it does not depend on the accuracy of any absolute measurements.

3.5.2 Bragg Additivity

The present results demonstrate that for these five oxides, there is a unique set of five stopping cross sections that is consistent with all combinations of pure metals and their oxides. Since this experiment depends on the energy loss on both the incoming and outgoing trajectories, this result is applicable to ^{4}He ions with energies of 1-2 MeV.

Recently, Baglin(1974) has performed a similar experiment to test Bragg's rule. His approach differs from the present method in that he used thick target yield levels instead of two-layered targets. As discussed in section 3.3.1, this requires accurate measurements of the ion dose and exact dead time correction. Facilities of this type are available to Baglin at the IBM Watson Research Center, and they were not available here at the California Institute of Technology. By measuring the thick target yields and solving Equation 3.6 for $[\varepsilon]$, he was able to determine the stopping cross sections for several elements and compounds by then inverting Equation 3.3.

One striking result of Baglin's experiment is that he used the oxygen and nitrogen stopping cross sections of Bourland, Chu and Powers (1971) and he found good agreement with Bragg's rule in SiO_2, Al_2O_3, Si_3N_4 and AlN, in direct contrast with the present results. This is due in part to the fact that he used his own values for the Al and Si stopping cross sections rather than use those reported in the literature, as was done here. His measurement of the Al stopping cross section, however, is about 11% higher than the value of Chu and Powers (1969). If this value at 2.0 MeV and the shape of the stopping power curve of Appendix B were used in the present calculations, the present

yield ratio measurements would then be in good agreement with these stopping powers.

The other reason his results appear to be in better agreement than ours is that Baglin compares molecular stopping cross sections while we compare the contributions of oxygen to the molecular stopping cross sections. Thus, any relative errors revealed by his measurements would be compared to the sum of the atomic stopping cross sections; *the* relative measurements found in our data are compared with the smallest of the relevant atomic stopping cross sections. The same effective discrepancy in both experiments would therefore appear larger using our analytical approach. For example, a closer examination of his results on SiO_2 show that the observed molecular stopping power is 2.3% low compared to his predicted value. Applying the present analytical method and assigning the discrepancy to the oxygen implies that the effective oxygen stopping cross section in his measurement is 7.6% lower than the reference value, compared to the 7% value shown in Table 3.6.

There is a basic philosophical difference in the two experiments. The results presented here have been used to develop a self-consistent analysis of the signal yields. The present results do not depend significantly on any external measurements. In Baglin's experiment, the analysis of the results depend critically on the measurements of Bourland, Chu and Powers(1971). The essence of the present analysis is to demonstrate the validity of a necessary condition for Bragg additivity. Baglin makes the broader claim that Bragg's rule is valid.

3.5.3 Physical State Effects

The reduction in the stopping cross section with increasing density due to dielectric effects was first recognized by Swann(1938). These effects have been shown to be large and easily observed for relativistic ion velocities in which Čerenkov radiation contributes to the loss of energy(see Crispin and Fowler(1970) for a recent review on this subject). By including these dielectric screening corrections for non-relativistic particles, Fermi(1940) has estimated that the stopping power in a condensed medium is "of the order of several per cent" lower than in a gaseous medium. A recent calculation based on Lindhard and Winther's statistical approach has shown that, in addition, solid state charge distributions produce lower stopping cross sections than Hartree-Fock-Slater wavefunctions for isolated atoms(Chu, Moruzzi and Ziegler).

In the energy range of 0-2 MeV ^{4}He ions, the most extensive experiments have been performed by the Baylor group. Their measurements on several hydrocarbon gases showed that the contribution to the stopping by the carbon in these compounds was systematically higher than the measured stopping power of solid carbon(Bourland and Powers, 1971). However, the carbon contribution to the stopping in fluoro-carbon gases was found to be in good agreement with the stopping in solid carbon(Powers, Chu, Robinson and Lodhi, 1972).

The systematic discrepancy observed in Table 3.6 between the oxygen contribution in the solid oxides and in molecular oxygen constitutes possible evidence for a physical state effect. Because of the possible errors in the absolute stopping cross sections(Table 3.7), each individual determination of the effective stopping cross section

of "solid" oxygen by this method could not be construed as proof of the existence of a physical state effect. However, a systematic discrepancy is observed for all possible choices of reference stopping powers.

For example, the stopping in Si has been measured independently by three groups with reasonably good agreement between 1 MeV and 2 MeV (Eisen et al, 1972; Lin, Olson and Powers, 1973; Ziegler and Brodsky, 1973). We have used the values of Eisen et al, the largest of the reported values. Using the other values would increase the apparent density effect by 2-5%, giving values of 9-12% for this effect in SiO_2.

The Al stopping cross section has been reported by two groups with agreement within about 5% for 1-2 MeV α-particles(Chu and Powers, 1969; Porat and Ramavataram, 1961). Because of the large inconsistencies in the Al-Si relative yields with respect to the reported stopping powers, we have remeasured the Al stopping cross section(see Appendix B). These values are in good agreement with the results of Porat and Ramavataram(1961), which are 2-6% higher than the results of Chu and Powers(1969) between 1 MeV and 2 MeV. This would reduce the observed physical state effect in Al_2O_3 from the 22% shown in Table 3.6 to about 17%.

We have also remeasured the Fe stopping cross section(Appendix B) and found slightly lower values(7±5%) than reported by Chu and Powers (1969). Using this value wsuld increase the apparent physical state effect in th two iron oxides to about 13%.

Bourland et al (1971) directly measured the differential energy loss in a gas cell in their measurement of the stopping cross section

in gaseous molecular oxygen, while Rotondi(1968) differentiated the range-energy relation. These two measurements agree between 1.5 MeV and 2.0 MeV with Rotondi's value about 5% higher at 1 MeV. Adopting Rotondi's values would increase the apparent physical state effect by 0-3%, depending on the oxide.

By taking appropriate choices of the reference stopping cross sections, the apparent physical state effect can be narrowed to 10-15%. This is almost exactly the value predicted in Ziegler, Chu and Feng (see the discussion in Chapter I for an appreciation of the limited contribution of the present author to this work).

The observed systematic discrepancy could be attributed to chemical binding effects. The magnitude of these effects on the stopping in gaseous oxides can be estimated by considering the cases of N_2O, N_2, CO and CO_2. Using the measurements of Bourland, Chu and Powers (1971) for these gases as well as O_2, it is possible to compare the contribution of oxygen to these molecular stopping cross sections with the stopping cross section of pure oxygen. In one case, CO and CO_2, there is no significant difference from molecular O_2 for 1-2 MeV ^4He ions. In the other case, N_2 and N_2O, the Bragg rule contribution of the oxygen is systematically 5-8% lower than the pure oxygen value in the same energy range.

The compounds used in this study are the stoichiometric oxides with the lightest cations from which nuclear scattering at 2.0 MeV could be expected to be purely electrostatic. This maximizes the fraction of the valence band electrons, which varies from 30% to 53%.

A simple test of the nature of the chemical binding is the difference in the Pauling electronegativity, which varies from 1.7 for Si-O to 2.3 for Mg-O. This covers almost the entire range available for binary solid oxides. The estimated ionic character of the bonding of these oxides varies from 51% to 74%. Any changes in the stopping power due to chemical binding effects should be maximized by this choice of compounds. Within the 1% sensitivity of the present experiment, there are no observable chemical effects in the stopping of 1-2 MeV ^{4}He ions in these solid oxides.

Baglin and Ziegler(1974) also investigated the possibility of chemical effects on the stopping power of silicon carbide. The thick target yields of three different allotropic forms of silicon carbide, 3C(β)-SiC, 6H-SiC and amorphous SiC, were compared and found to be the same within ±1%. Since the two crystalline forms have band gaps of 2.3 eV and 3.0 eV, this is taken as evidence that there were no observable chemical effects on the stopping in these different forms of silicon carbide.

3.5.4 Applications to Backscattering Spectrometry

The validity of Bragg's rule implies that the stopping power in units of $dE/\rho dx$ can be predicted from the absolute stopping powers of the constituent elements. The present results indicate that the errors produced by making this assumption are much smaller than the uncertainties in the available stopping cross section data. Note, however, that the stopping power in units of $dE/\rho dx$ is relatively insensitive to almost all variations in the sample composition.

A more useful application would be to determine the composition of a sample from the thick target yield. If the signals from all of the constituent elements are easily extracted, the present method is not recommended. The composition can more accurately be determined directly from the separate signals. Sometimes, as in the case of several oxides, the signals from the elements with low atomic numbers cannot be measured easily. In these cases, there is no alternative to inferring the composition from the thick target yield signals from the heavy elements. The accuracy of this procedure, while no better than the available stopping cross section data, will not be affected by any deviations from Bragg's rule.

Two qualifications must be attached to the present claims. First, they only apply to ^4He ions of energy over 1 MeV, since significant deviations from Bragg's rule are expected to appear at lower energies. Secondly, the accuracy of the calculated stopping powers of solids can be improved slightly if the stopping cross sections of the normally gaseous elements is reduced by about 10%; applying this change, for example, improved the agreement between the predicted and observed yields from a sample of Ta_2O_5 (one of the samples shown in Chu, Nicolet, Mayer and Evans, 1974; calculations by Feng and Chu, unpublished).

REFERENCES

Chapter 3

J. E. E. Baglin and J. F. Ziegler, 1974, J. Appl. Phys., vol. 45, p. 1413.

P. D. Bourland, W. K. Chu and D. Powers, 1971, Phys. Rev. B, vol. 3, p. 3625.

P. D. Bourland and D. Powers, 1971, Phys. Rev. B, vol. 3, p. 3635.

David. K. Brice, 1973, Sandia Laboratories Internal Report SLA-73-0843(unpublished).

F. Brown and W. D. Mackintosh, 1973, J. Electrochem Soc., vol. 120, p. 1096.

W. K. Chu, 1973, unpublished.

W. K. Chu, B. L. Crowder, J. W. Mayer and J. F. Ziegler, 1973, Appl. Phys. Lett., vol. 22, p. 490.

W. K. Chu, V. L. Moruzzi and J. F. Ziegler, 1974, unpublished.

W. K. Chu, M-A. Nicolet, J. W. Mayer and C. A. Evans, 1974, to be published, Analytical Chemistry.

W. K. Chu and D. Powers, 1969, Phys. Rev., vol. 187, p. 478.

A. Crispin and G. N. Fowler, 1970, Rev. Mod. Phys., vol. 42, p. 290.

C. G. Darwin, 1914, The Philosophical Magazine, vol. 28, p. 499.

F. H. Eisen, G. J. Clark, J. Bøttiger and J. M. Poate, 1972, Radiation Effects, vol. 13, p. 93.

J. S.-Y. Feng, C. H. Bajorek and M-A. Nicolet, 1972, IEEE Trans. on Magnetics, vol. MAG-8, p. 277.

J. S.-Y. Feng, W. K. Chu, M-A. Nicolet and J. W. Mayer, 1973, Thin Solid Films, vol. 19, p. 195.

E. Fermi, 1940, Phys. Rev., vol. 57, p. 485.

Richard W. Hill, 1953, Phys. Rev., vol. 90, p. 845.

C. M. Jones, G. C. Phillips, R. W. Harris and E. H. Beckner, 1962, Nuclear Physics, vol. 37, p. 1.

M. Kamoshida and J. W. Mayer, 1972, J. Electrochem. Soc., vol. 119, p. 1084.

M. Kamoshida, I. V. Mitchell and J. W. Mayer, 1971, Appl. Phys. Lett., vol. 18, p. 292.

W. K. Lin, H. G. Olson and D. Powers, 1973, Phys. Rev. B, vol. 8, p. 1881.

W. K. Lin, H. G. Olson and D. Powers, 1973, J. Appl. Phys., vol. 44, p. 3631.

M-A. Nicolet and J. S.-Y. Feng, 1974, unpublished(presented at the International Magnetics Conference, 14-17 May 1974, Toronto, Ontario, Canada).

D. I. Porat and K. Ramavataram, 1961, Proc. Phys. Soc.(London), vol. 78, p. 1135.

D. Powers, W. K. Chu, R. J. Robinson and A. Lodhi, 1972, Phys. Rev. A, vol. 6, p. 1425.

E. Rotondi, 1968, Radiation Research, vol. 33, p. 1.

W. F. G. Swann, 1938, J. Franklin Institute, vol. 226, p. 598.

J. F. Ziegler and J. E. E. Baglin, 1974, J. Appl. Phys., vol. 45, p. 1888.

J. F. Ziegler and M. H. Brodsky, 1972, J. Appl. Phys., vol. 44, p. 188.

J. F. Ziegler and W. K. Chu, 1973, IBM Research Report RC4288(#19193).

J. F. Ziegler, W. K. Chu and J. S.-Y. Feng, 1974, unpublished.

Chapter 4

SUMMARY

Two self-consistent approaches to verifying the applicability of Bragg's rule have been described for solid targets. These two methods of testing Bragg additivity can be applied to the vast majority of the possible mixed solid targets. The sensitivity of these methods have been shown experimentally to be about 1%.

The present results indicate that any violations of Bragg's rule in solid alloys or compounds are below 1-2%. However, when one of the elements is normally a gas, the gas phase stopping cross section appears to be slightly larger than the solid phase stopping cross section for the same element. In the broadest, this constitutes a violation of Bragg's rule. Nonetheless, there is a unique value for the contribution of oxygen to the stopping power of a solid oxide, even if this value appears to be lower than the gas phase value. This result suggests that changes in the stopping power due to physical state and density effects probably dominate any possible changes due to the differences in the chemical binding states in these solid compounds.

A practical consequence is that Bragg's rule can be confidently applied when analyzing MeV backscattering spectra. Any errors in doing this for 1-2 MeV ^4He ions will usually be much smaller than the uncertainties in the stopping cross section data used in the analysis. The accuracy may be improved slightly by making a 10% allowance for the apparent density effects. Furthermore, reversing the logic of the test described in Chapter 2 results in an easy method for testing

the consistency of the data taken either from a series of identical samples or from the same sample after various steps in an experiment. The uncertainties in the available stopping power data preclude reversing the logic of the test described in Chapter 3 to determine the composition of a layer with a better than about 10% accuracy.

APPENDIX A

A COMPUTER PROGRAM TO SIMULATE BACKSCATTERING SPECTRA

A.1 General Description

As a part of the Bragg's rule experiment, a computer program to synthesize a backscattering spectrum was developed. It is capable of calculating a theoretical spectrum for a multi-layered target in which the composition in each layer is constant. The program was written to accomodate a structure with up to ten layers. A complementary program, written by David Brice(1973), can be used to analyze a single-layered spectrum with continuously varying composition.

In a typical backscattering spectrum, the detected particles are analyzed into channels of equal energy intervals. Therefore, the calculation must be performed in depth intervals that correspond to equal energy intervals at the detector.

In this program, the calculation is performed in two passes. In the first pass, the backscattered energy as a function of depth is calculated for intervals of equal width, such as 20 Å. This generates a table that gives the incoming particle energy and the detected particle energy as a function of depth, as well as the differential rate of detected energy loss(the [S]-factor). Because of the number of calculations required to generate this table, this is the slowest step in the entire program. The incoming and outgoing particle energies as a function of position in the target are used to determine the rate at which the particle loses energy. This is calculated by entering the particle energy into a polynomial fit to the energy dependence of the stopping

power of the target. Since the kinematic scattering factors(Eq. 3.2) are different for different elements, this table must be calculated separately for each element in the target that produces a detectable signal.

Once this table has been generated, the next step is to calculate the scattering yield from each element. The table allows the program to calculate the step size required to produce fixed detected energy intervals. The backscattering rate from that step is then calculated from the partial density of the element in that step and the Rutherford scattering cross section(Darwin, 1914). The scattering cross section is calculated using the incident ion energy as given in the table calculated in the first pass. Since the Rutherford cross section for any large angle scattering is very small, it is assumed that there is no beam flux attenuation throughout the target.

The signal for each element is calculated separately. The program has facilities to plot each of these signals separately. In addition, it is assumed that the detected spectrum is a superposition of the signals from the separate layers and separate elements. The program calculates the superposition of these signals by taking a channel-by-channel sum of the signals and plots the composite spectrum. Provisions have been made to allow the suppression of this plotting feature, since this can be an expensive operation.

A provision is also made to display on the same plot the calculated spectrum and an experimental spectrum. In order to make a sensible comparison, the height of the calculated spectrum can be normalized to match the height of part of the experimental data.

In addition, the program has an arbitrary normalization, corresponding to an arbitrary but constant incident particle dose, available to the user. As a third normalizing option, the normalizing factor can be made identical to that in a previously calculated spectrum to facilitate direct comparisons; part of the output of every calculation is the normalizing factor and the option used to determine that factor.

The only obvious error in the program is that it assumes that all things are constant in each step. In particular, it assumes that the particle energy and the stopping power are both constant over each step. The calculated value is the mean value over each interval, so the error in the program is of the order of the differences of the first derivatives of the stopping power or the scattering cross section at the ends of the interval. Thus, this small error is of the order of the second derivative of the stopping power or the scattering cross section. The less obvious errors are due to truncation errors in the computer itself, which have been minimized by using double precision arithmetic. Nonetheless, the effects of these hardware limitations can sometimes be seen in the calculated results. Fortunately, these errors are usually much smaller than the errors in the stopping cross section data used in the calculations.

A.2 Using the Program

This part describes, approximately in the sequence the data are entered, the requirements for successfully using the program. The first requirement is 200 K bytes of core storage, which must be specified on the SET card in order to load the program into the computer.

The program is capable of calculating an arbitrarily large number of complete spectra. The first card in the DATA deck specifies the number of spectra to be generated by the program. The FORTRAN format for this card is (8X, I2). The following set of data cards is then read once for each complete spectrum to be generated.

The first card of a set for one spectrum gives the number of layers in the target, the number of elements in the target, the beam energy in keV, the "quitting" energy in keV, the backscattering angle in degrees, the energy width of a channel in keV, the size of the step to be used in the first pass in angstroms, the normalization value to be used in the program and a flag to indicate how the program is to use the normalization value. The format for this card is (3X, I2, 3X, I2, 3F10.3, 2F10.4, F15.3, 3X, I2). The quitting energy tells the program when to terminate its calculations and the internally determined lower limit is 200 keV. When the normalization flag is negative, the value entered for the normalization is ignored and the value available in the program is used. When the flag is positive, the value entered is taken as the desired number of counts desired in the highest completely filled channel for the first element calculated. To avoid generating meaningless calculations, this element must be present in the first layer of the target. A zero value for the flag means that the normalization value is to be taken as the value to be used internally in the program. The same normalization value is used for all computations of a given spectrum and this value is outputted by the program with each one of the signals calculated for each of the elements.

The next card is used to set up the plotter for the final,

completely synthesized spectrum. The first entry is the alphanumeric information to be printed in the upper right hand corner of the plot. The minimum and maximum energies to be plotted, in keV, are the next two entries. The maximum value of the vertical axis in counts per channel is the fourth entry. The fifth entry is a flag to indicate to the program whether or not there is experimental data to be plotted with the calculated spectrum. The last entry is a flag that allows suppressing all of the plotted output of the program. The program is designed to automatically optimize the horizontal and vertical scales of the plot to allow for the fact that there are twenty vertical and thirty-two horizontal divisions on the graph paper supplied by the Caltech computing center. To allow plotting experimental data with the calculated spectrum, the fifth entry must be over 100. To suppress all plotting, the last flag must be a negative integer. Note that the default values on these last two flags, the action taken when these are left blank, is not to plot any experimental data and to plot all the calculated spectra. The format for this card is (2X, A8, 3F10.2, 7X, I3, 7X, I3).

The next card contains the labels for the horizontal and vertical axes when plotting the complete spectrum. The format for this card is (2A40).

The next set of cards give the energy loss specifications for each layer. There must be one of these cards for each layer. The first entry is the density of the layer in gm/cm^3. The second set of entries are the five coefficients of a fourth order polynomial fit to the energy loss curve for that layer, a_0, a_1, a_2, a_3, and a_4, where

$$\frac{dE}{\rho dx} = a_0 + a_1E + a_2E^2 + a_3E^3 + a_4E^4$$

where the energy is in keV and the stopping power is ten times the value in (keV-cm^2/μg). For example, the stopping power of aluminum at 2.0 MeV is about 100 kev-cm^2/μg. The energy used by the program would be 2000 (in keV) and the stopping power would be about 1000 (in 10 x keV-cm^2/μg). This is, admittedly an unfortunate set of units, but it is a historical accident of the development of the program. It was not changed to more conventional units because there exists here a profound respect for one of the corollaries to Murphy's Law: Never fool with a working system! At least two semi-empirical formulations to smooth fits to the stopping power have appeared recently(Chu and Ziegler, 1973; Brice, 1973), and if the coefficients for a large number of materials is available for either of these formulations, it might be worthwhile to modify the program to accommodate these tables. Returning to the essentials of the program, after the five coefficients comes the eight alphanumeric characters that the user can assign to identify the layer in the printed output. The last entry is the thickness of the layer in angstroms, assuming the density specified as the first entry. The format for this card is (F7.3, 5E11.4, A8, F10.2).

The next set of cards provides the relevant information for each target element. There must be three cards for each element. The first of these three cards gives the mass of the target element in atomic mass units(amu), the charge of the nucleus in elementary charges(the same as atomic number), and the name of the element. The format for thic card is (10X, 2F10.4, 2X, A8). The next card gives the partial

density of the element in each layer in gm/cm^3 in the format (10F8.4). The partial density is the contribution of the element to the density of the layer. The sum of the partial densities for each layer should equal the density of the layer. Since it may be possible that a layer would contain elements that would not be detected by backscattering(such as hydrogen), the sum of the partial densities entered into the program for each layer do not necessarily add up to the density of the layer. The program does not have any provision for checking that these partial densities sum to the layer densities. The third card of these sets gives the labels for the horizontal and vertical axes of the plot of the contribution of this particular element to the total spectrum. The format for this card is (2A40).

If the experimental data flag was set greater than or equal to 100, the program looks for some experimental data. The first card in this set contains the number of data points to be read, the energy of the first data point in keV, and the energy of the last data point in keV. The format of this card is (6X, I4, 2F10.2). The program then determines the number of cards to be read, assuming there are ten data points per card in a (10F8.0) format. After the data have been read, the next two cards give the alphanumeric data to be printed in the plot. The first of these cards holds the eight characters to go into the upper right hand corner of the plot in the format (2X, A8). The horizontal and vertical axes labels are read from the last card in the familiar (2A40) format.

This completes the data required for a single spectrum.

The output from the program was designed to minimize the requirement to find the data cards when reading the printed output. The most important part of this is that every data card read into the program is printed out by the program before that information is used by the program. To facilitate reading this output, descriptive legends accompany the regurgitation of the material on the data cards.

After that, the calculated data from the first set of computations is printed. This is the energy versus depth information that is used in the rest of the program. The first column gives the depth into the target in angstroms; the second gives the corresponding detected backscattering energy from that depth; the column gives the [S]-factor as a function of the depth in keV/Å; and the last column has the incoming particle energy as a function of depth.

The second part of the output gives the backscattered count rate as a function of the detected energy. The first line gives the normalization value used internally by the program as well as the externally specified normalization flag. The tabulated data then gives the channel number in descending order, the backscattered particle energy for that channel, the count rate into that channel, the beam energy at that particular depth, and the corresponding depth.

This output is generated for each element in the target. As the signal from each element is calculated, they are summed to give the composite spectrum.

The plotted output, if it is not suppressed, consists of one plot for each element, giving the contribution of each element to the total spectrum, and one composite plot produced by superposing all

the calculated elemental contributions. The horizontal and vertical scales for the single-element signal plots are those specified by the user and as modified by the program. The vertical scale in the final composite plot is again modified by the program to insure that none of the calculated spectrum exceeds the limit of the vertical scale. If experimental data is to be plotted, the composite spectrum is replotted and the experimental data is plotted on the same scale.

A.3 Listing of the Program

The following is a listing of the program to simulate backscattering spectra. It is divided into three parts. The first part is the main program. This part reads the data into the computer and controls the subroutines to eventually produce the composite plot of the calculated spectrum.

The second part is a subroutine called RANDOM. This is the part of the program that actually calculates the depth dependence of the incoming and backscattered particle energies and then calculates the backscattered particle yield for a particular element in the target. This part of the program also plots the calculated signal from each target element before returning control to the main program.

The third part contains the miscellaneous subroutines needed to provide further support for the main program. The function ALF is used to calculate the kinematic scattering factor(Eq. 3.2). The function CROSS calculates the corrections to the center-of-mass formula for the laboratory-frame Rutherford scattering cross section. The function ELOSS is used to calculate the appropriate rate of energy loss

for a particular particle energy in a specified layer. The function EOUT is designed to calculate the detected particle energy of an outgoing, backscattered particle; the data required for this subroutine are the particle energy after scattering, the depth in the target, and the scattering angle.

Note that special care has been taken in this program to properly account for the fact that some channels may span an interface between two layers. The calculated spectra show no anomalous dips or peaks near these interfaces, indicating that the calculations in these potentially hazardous regions have been performed properly.

```
      IMPLICIT REAL*8(A-H,O-$),INTEGER(I-N)
      DIMENSION  RATE(2000),THICK(10),PART(10),ANAME(10),PRHO(10)
      COMMON/R/ A(5,10),RHO(10),DX
      COMMON/T/T1,T2,T3,T4,T5,T6,T7,T8,T9,T10
      REAL*4  WORDS(3),WORD(3),SPECT(2000),RAND(2000)
      REAL*4  XLABEL(10),YLABEL(10)
      REAL*4  XLAB(10),YLAB(10),XMIN,XMAX,XLONG,YMIN,YMAX,YLONG,VMAX
      COMMON/INPUT/EIN,EQUIT,ECHAN,THETA
      COMMON/SIZE/XLAB, YLAB, WORD, XMIN, XMAX, XLONG,
     1   YMIN, YMAX, YLONG, IDIVX, IDIVY
      COMMON/TARGET/AMASS,ZT
      COMMON/P/IPFLG
      REAL*4  XLNGTH,YLNGTH,XLNG,YLNG
      REAL*4  XLLL,YLLL
      REAL*4  EXPX(2000), EXPY(2000)
      EQUIVALENCE(RATE(1),EXPX(1)),(RATE(1001),EXPY(1))
      EQUIVALENCE (WORD(1),ENAME)
C
C     THE FOLLOWING CARDS SET UP THE PLOTTER
C
      COMMON/COMPLO/ITEST,XLNGTH,YLNGTH
      COMMON/COMCPL/IT,XLNG,YLNG
      COMMON/COMPLT/ITTT,XLLL,YLLL
      ITEST  =  1
      XLNGTH =  16.0
      YLNGTH =  10.0
      IT     =  1
      XLNG   =  16.0
      YLNG   =  10.0
      ITTT   =  1
      XLLL   =  16.0
      YLLL   =  10.0
      YMIN   =  0.0
C
C       SKIP A COUPLE OF PAGES ON THE PRINTER
C
      WRITE(6,100)
      WRITE(6,100)
  100 FORMAT('1')
C
C       READ THE NUMBER OF COMPLETE SPECTRA TO BE GENERATED
C
      READ(5,101)  NSPEC
  101 FORMAT(8X, I2)
C
C       WRITE THE NUMBER OF COMPLETE SPECTRA TO BE GENERATED AND
C            PLOTTED
C
      WRITE(6,102)  NSPEC
  102 FORMAT(20X,'THE NUMBER OF COMPLETE SPECTRA TO BE GENERATED IS',
     1   I3,',')
C
C
      EXECUTE THE I/O ROUTINES AS MANY TIMES AS THERE ARE SPECTRA
C           TO BE GENERATED
C
      DO  999   ISPEC  =  1,NSPEC
C
C       VMAX IS PART OF THE SELF-SCALING ROUTINE FOR THE PLOTTER
C
```

```
      VMAX   =  0.0
C
C
C       READ THE FOLLOWING INPUT
C            THE NUMBER OF LAYERS IN THE SAMPLE
C
C            THE NUMBER OF ELEMENTS TO BE CONSIDERED
C            THE INCIDENT BEAM ENERGY IN KEV
C            THE ENERGY VALUE FOR TERMINATING CALCULATIONS
C                 THE DEFAULT VALUE IS 100 KEV
C            THE BACKSCATTERING ANGLE IN DEGREES
C            THE "ENERGY PER CHANNEL" IN KEV
C            THE SIZE OF THE ITERATION STEP IN THE CALCULATION IN ANG
C            THE NORMALIZATION VALUE FOR THE SPECTRUM
C            AND A FLAG TO DETERMINE HOW TO USE THE NORMALIZATION
C               WHEN THE FLAG>0 THE NORMALIZATION VALUE IS TAKEN AS THE
C                 NUMBER OF COUNTS IN THE HIGHEST COMPLETELY FILLED
C                 CHANNEL WHEN GENERATING A SPECTRUM
C               WHEN THE FLAG=0 THE VALUE IS TAKEN AS A VALUE
C                 PREVIOUSLY DETERMINED, AS IN THE CASE OF A SECOND
C                 ELEMENT IN A SINGLE SPECTRUM
C               WHEN THE FLAG<0 THE NORMALIZATION VALUE IS IGNORED
C
      READ(5,105)  NLAYER,NEL,EIN,EQUIT,THETA,ECHAN,DX,ANORM,NORM
  105 FORMAT(3X,I2,3X,I2,3F10.3,2F10.4,F15.3,3X,I2)
C
C       RECALL THAT THE DEFAULT VALUE FOR THE MINIMUM ENERGY FOR
C            CONTINUING CALCULATIONS IS 100 KEV
C
      EQUIT  =  DMAX1( EQUIT, 100.0D0)
C
C       WRITE THE SPECTRUM NUMBER OF THIS SET OF SPECTRA
C
      WRITE(6,106)  ISPEC
  106 FORMAT('1',9X,'THE INPUT DATA FOR SPECTRUM NUMBER  ',I3 //// )
C
C       WRITE THE DATA ON THE FIRST DATA CARD FOR THIS SET OF CARDS
C
      WRITE(6,107)
  107 FORMAT(9X,'LAYERS',7X,'ELEMENTS',7X,'EIN(KEV)',5X,'EQUIT(KEV)',
     1   10X,'ANGLE',5X,'ECHAN(KEV)',8X,'DX(ANG)',11X,'NORM',5X,'NFLAG',
     2  / )
      WRITE(6,108)  NLAYER,NEL,EIN,EQUIT,THETA,ECHAN,DX,ANORM,NORM
  108 FORMAT(10X,I3,11X,I3,9X,F10.3,4X,F10.3,7X,F10.3,3X,F10.4,6X,
     1   F10.4,4X,F15.3,3X,I2 ///)
C
C       READ THE INFORMATION FOR SETTING UP THE PLOTTER
C            THE LEGEND GOING IN THE UPPER RIGHT HAND CORNER IS FIRST
C            NEXT IS THE MINIMUM ENERGY TO BE PLOTTED IN KEV
C            THIRD IS THE MAXIMUM ENERGY TO BE PLOTTED IN KEV
C            THEN THE MAXIMUM NUMBER OF COUNTS PER CHANNEL EXPECTED
C            AND NEXT IS A FLAG TO DETERMINE WHETHER OR NOT
C               EXPERIMENTAL DATA WILL FOLLOW TO BE PLOTTED WITH A
C               COMPLETE SYNTHESIZED SPECTRUM
C                  THE FLAG MUST BE >99 BEFORE THE PROGRAM WILL
C                   ACCEPT A SET OF EXPERIMENTAL DATA FOR PLOTTING
C            FINALLY, THERE IS AN OPTION TO SUPPRESS PLOTTING OF THE
C               SYNTHESIZED SPECTRA,  THIS OPTION IS EXERCISED BY
C               SETTING THE FLAG TO ANY NEGATIVE NUMBER.
C
```

```
      READ(5,109)  WORDS(1),WORDS(2),XMIN,XMAX,YMAX,IRAW,IPFLG
  109 FORMAT(2X,2A4,3F10.2,7X,I3,7X,I3)

C       NOW WRITE THE DATA ON THE SECOND DATA  CARD
C
      WRITE(6,110)
  110 FORMAT(10X,'PLOTTER CONTROL',15X,'WORDS',10X,'XMIN',16X,'XMAX',
     1   16X,'YMAX',6X,'REAL DATA?',4X,'PLOT?' / )
      WRITE(6,111)  WORDS(1),WORDS(2),XMIN,XMAX,YMAX,IRAW,IPFLG
  111 FORMAT(38X,2A4,6X,F10.2,10X,F10.2,10X,F10.2,8X,I4,6X,I4 // )
C
C       READ THE LABELS FOR THE HORIZONTAL AND VERTICAL AXES ON THE
C            COMPLETE SYNTHESIZED SPECTRUM.  IF ONLY ONE ELEMENT IS TO
C            BE CONSIDERED, THIS PLOT WILL BE OMITTED.  HOWEVER, A CARD
C            MUST STILL BE INCLUDED FOR THE LABELS EVEN IF ONLY BLANKS
C
      READ(5,112)  XLABEL, YLABEL
  112 FORMAT(20A4)
C
C       NOW WRITE THE LABELS ON THE PRINTED OUTPUT
C
      WRITE(6,113)
  113 FORMAT(40X,'XLABEL',40X,'YLABEL' / )
      WRITE(6,114)  XLABEL, YLABEL
  114 FORMAT(40X, 10A4,6X,10A4 /////)
C
C       THE FOLLOWING DO LOOPS ARE FOR ZEROING OUT THE ARRAYS

      DO  205   IL  =  1, 2000
      SPECT(IL)  =  0.0
      RAND(IL)   =  0.0
  205 CONTINUE
      DO  209   IL  =  1, 10
      PART(IL)     =  0.0
      THICK(IL)    =  0.0
      ANAME(IL)    =  0.0
      RHO(IL)      =  0.0
      DO  208   IJ  =  1, 5
      A(IJ,IL)     =  0.0
  208 CONTINUE
  209 CONTINUE
C
C
C       READ ONE CARD FOR EACH LAYER SPECIFYING
C
C            THE DENSITY OF THE LAYER IN GM/CM**3
C            THE COEFFICIENTS OF THE FOURTH ORDER POLYNOMIAL GIVING
C            THE STOPPING POWER OF THE MATERIAL IN THE LAYER
C            THE NAME OF THE LAYER
C            AND THE THICKNESS OF THE LAYER IN ANGSTROMS
C
C
C       AS THE DATA IS BEING READ, WRITE IT OUT ON THE PRINTER

      DO  219   IL  =  1,NLAYER
      READ(5,120)  RHO(IL),(A(J,IL),J=1,5),ANAME(IL),THICK(IL)
  120 FORMAT(F7.3,5E11.4,A8,F10.2)
      WRITE(6,121)  IL
  121 FORMAT('   LAYER  =  ',I3,' ,'  // )
      WRITE(6,122)
```

```
  122  FORMAT(10X,'DENSITY',10X,'A(0)',12X,'A(1)',12X,'A(2)',12X,'A(3)',
     1  12X,'A(4)',15X,'LNAME',6X,'THICK'/ )
       WRITE(6,123)  RHO(IL),(A(J,IL),J=1,5),ANAME(IL),THICK(IL)
  123  FORMAT(10X,F7.3, 6X, 5(E11.4,5X),6X,A8,3X,F10.2 ///  )
  219  CONTINUE
C
C        THE FOLLOWING DEFINES THE DEPTH TO EACH INTERFACE
C
       T1     =  THICK(1)
       T2     =  T1   +  THICK(2)
       T3     =  T2   +  THICK(3)
       T4     =  T3   +  THICK(4)
       T5     =  T4   +  THICK(5)
       T6     =  T5   +  THICK(6)
       T7     =  T6   +  THICK(7)
       T8     =  T7   +  THICK(8)
       T9     =  T8   +  THICK(9)
       T10    =  T9   +  THICK(10)
C
C         WRITE THE NAME OF EACH LAYER, THE THICKNESS OF THE LAYER,
C              AND THE THICKNESS OF THE SAMPLE TO THE DEPPEST PART OF THE
C              LAYER
C
       WRITE(6,250) (ANAME(J), J = 1, NLAYER)
  250  FORMAT('1',9X,10A10)
       WRITE(6,251) (THICK(J), J = 1, NLAYER )
  251  FORMAT(//10X, 10F10.2)
       WRITE(6,252)  T1, T2, T3, T4, T5, T6, T7, T8, T9, T10
  252  FORMAT(//10X, 10F10.2 / '1' )
C
C         THE FOLLOWING IS A ROUTINE FOR OPTIMIZING THE HORIZONTAL AND
C              VERTICAL AXES ON THE PLOTTER
C
       LOG    =  ALOG10(YMAX)
       CHAR   =  10.0**LOG
       DIGMAX =  YMAX/CHAR
       IF(DIGMAX-1.0)  305,301,305
  301  DIGMAX =  10.0*DIGMAX
       CHAR   =  CHAR/10.0
  305  MAXDIG =  DIGMAX
       DIGMX  =  MAXDIG
       IF(DIGMAX-DIGMX)  307,307,306
  306  DIGMX  =  DIGMX + 1.0
  307  MINDIG =  YMIN/CHAR
       DIGMN  =  MINDIG
       DIGDIF =  DIGMX - DIGMN
       IF(DIGDIF-5.0)  312,312,311
  311  DIF    =  10.0
       IDIVY  =  10
       GO TO 320
  312  IF(DIGDIF-2.0)  314,314,313
  313  DIF    =  5.0
       IDIVY  =  5
       GO TO 320
  314  IF(DIGDIF-1.0)  316,316,315
  315  DIF    =  2.0
       IDIVY  =  4
       GO TO 320
  316  DIF    =  1.0
       IDIVY  =  10
```

```
  320  YMIN   =  DIGMN*CHAR
       YMAX   =  YMIN + DIF*CHAR
       YLONG  =  10.0
       LOG    =  ALOG10(XMAX)
       CHAR   =  10.0**(LOG-1)
       DIGMAX =  XMAX / CHAR
       IF(DIGMAX - 10.0 )  331,331,332
  331  DIGMAX =  10.0*DIGMAX
       CHAR   =  CHAR/10.0
  332  MAXDIG =  DIGMAX
       DIGMX  =  MAXDIG
       IF(DIGMAX-DIGMX)  334,334,333
  333  DIGMX  =  DIGMX + 1.0
  334  MINDIG =  XMIN/CHAR
       DIGMN  =  MINDIG
       DIGDIF =  DIGMX - DIGMN
       IF(DIGDIF - 64.0 )  343,343,341
  341  DIF    =  160.0
       GO TO 360
  343  IF(DIGDIF-32.0)   346,346,344
  344  DIF    =  64.0
       GO TO 360
  346  IF(DIGDIF-16.0)  349,349,347
  347  DIF    =  32.0
       GO TO 360
  349  IF(DIGDIF-6.4)  352,352,350
  350  DIF    =  16.0
       GO TO 360
  352  IF(DIGDIF-3.2)  354,354,353
  353  DIF    =  6.4
       GO TO 360
  354  IF(DIGDIF -1.6)  357,357,355
  355  DIF    =  3.2
       GO TO 360
  357  DIF    =  1.6
  360  IDIVX  =  16
       XMIN   =  DIGMN*CHAR
       XMAX   =  XMIN + DIF*CHAR
       XLONG  =  16.0
C
C         THE FOLLOWING IS FOR INPUTTING THE SPECIFICATIONS OF EACH
C              ELEMENT
C
       DO  899   IEL  =  1, NEL
C
C         FIRST ZERO  OUT THE VALUES OF THE PARTIAL DENSITY
C
       DO  223   IL  =  1, 10
       PRHO(IL)   =  0.0
  223  CONTINUE
C
C         NOW ZERO OUT THE BUFFER AREA FOR HOLDING THE COUNT RATE FOR
C              EACH ELEMENT
C
       DO  224   IL  =  1, 2000
       RATE(IL)   =  0.0
  224  CONTINUE
C
C         READ THE MASS OF THE THE ELEMENT IN AMU, THE CHARGE IN
C              ELEMENTARY CHARGES, AND THE NAME OF THE ELEMENT
```

```
C
      READ(5,130)  AMASS, ZT, ENAME
  130 FORMAT( 10X, 2F10.4, 2X, A8 )
C
C       BEFORE WRITING THE INFORMATION ON THIS CARD, TELL US WHICH
C            SPECTRUM AND WHICH ELEMENT WE ARE DOING THE CALCULATION ON
C
      WRITE(6,131)  ISPEC, IEL
  131 FORMAT(10X,'SPECTRUM NUMBER = ',I3,20X,'ELEMENT NUMBER = ',I3///)
C
C            NOW WRITE THE INFORMATION SPECIFYING THE ELEMENT
C
      WRITE(6,132)
  132 FORMAT(23X,'AMASS',14X,'CHARGE',12X,'ELEMENT NAME' / )
      WRITE(6,133)  AMASS, ZT, ENAME
  133 FORMAT( 20X, F10.4,10X, F10.4,15X, A8  //// )
C
C       READ THE PARTIAL DENSITY OF THE ELEMENT IN EACH LAYER IN GM/CC
C
      READ(5,140)  (PRHO(IJ),IJ=1,NLAYER)
  140 FORMAT( 10F8.4 )
C
C       AND THEN WRITE THE PARTIAL DENSITY OF THE ELEMENT IN EACH LAYER
C
      WRITE(6,141)
  141 FORMAT(10X,'PARTIAL DENSITY'//5X,'LAYER = ',5X,'1',9X,'2',9X,'3',
     1   9X,'4',9X,'5',9X,'6',9X,'7',9X,'8',9X,'9',9X,'10' // )
      WRITE(6,142)  ( PRHO(IJ),IJ = 1, 10)
  142 FORMAT( 15X, 10( F8.4, 2X)///)
C
C       A PLOT IS TO BE GENERATED FOR EACH ELEMENT TO SHOW ITS
C            CONTRIBUTION TO THE WHOLE SPECTRUM,  READ THE HORIZONTAL
C            AND VERTICAL AXES LABELS FOR THIS PLOT
C
      READ(5,150)  XLAB,YLAB
  150 FORMAT(  20A4  )
C
C       NOW WRITE THE LABELS AS USUAL
C
      WRITE(6,151)
  151 FORMAT(10X,'PLOTTER CONTROL',15X,'WORDS' / )
      WRITE(6,152)  WORD(1),WORD(2)
  152 FORMAT( 38X, 2A4 // )
      WRITE(6,113)
      WRITE(6,114)  XLAB, YLAB
C
C       WE WANT TO SAVE EXECUTION TIME, SO ONLY CALCULATED AS DEEP AS
C            THE ELEMENT IS PRESENT IN THE SAMPLE
C
      KLAYER =  0
      DO  229   ILAYER  =  1,10
      JLAYER =  11 - ILAYER
      IF(PRHO(JLAYER))   229,229,225
  225 KLAYER =  JLAYER
      ILAYER =  25
  229 CONTINUE
      EQSAVE =  EQUIT
C
C       CALCULATE THE RANDOM SPECTRUM FOR THIS ELEMENT
C
```

```
      CALL  RANDOM(RATE,KLAYER,ANORM,NORM,PRHO)
      EQUIT = EQSAVE

C       ADD UP THE CONTRIBUTIONS FROM EACH ELEMENT TO SYNTHESIZE A
C            RANDOM SPECTRUM FOR ALL ELEMENTS CONSIDERED
C
      DO  249   IL  =  1, 2000
      SPECT(IL)   =  SPECT(IL) + RATE(IL)
      VMAX   =  AMAX1(VMAX,SPECT(IL))
  249 CONTINUE
  899 CONTINUE
C
C       READJUST THE VERTICAL AXIS IF NECESSARY
C
      IF(VMAX.LE.YMAX)  GO TO 950
      LOG    =  ALOG10(VMAX)
      CHAR   =  10.0**LOG
      DIGMAX =  VMAX / CHAR
      IF(DIGMAX - 1.0 )  905, 901, 905
  901 DIGMAX =  10.0 * DIGMAX
      CHAR   =  CHAR / 10.0
  905 MAXDIG =  DIGMAX
      DIGMX  =  MAXDIG
      IF(DIGMAX - DIGMX)  907, 907, 906
  906 DIGMX  =  DIGMX + 1.0
  907 DIGDIF =  DIGMX
      IF(DIGDIF - 5.0)  912, 912, 911
  911 DIF    =  10.0
      IDIVY  =  10
      GO TO 920
  912 IF(DIGDIF - 2.0 )  914, 914, 913
  913 DIF    =  5.0
      IDIVY  =  5
      GO TO 920
  914 IF(DIGDIF - 1.0)  916, 916, 915
  915 DIF    =  2.0
      IDIVY  =  4
      GO TO 920
  916 DIF    =  1.0
      IDIVY  =  10
  920 YMAX   =  DIF * CHAR
C
C       PLOT ONLY THOSE CHANNELS THAT FIT WITHIN THE ENERGY AXIS
C
  950 SPAN   =  XMAX - XMIN
      NPOINT =  SPAN/ECHAN + 1.0
      MINPT  =  XMIN / ECHAN + 1.0
      MAXPT  =  MINPT + NPOINT - 1
      DO  970   IL  =  MINPT, MAXPT
      IR     =  IL - MINPT + 1
      RAND(IR)  =  SPECT(IL)
  970 CONTINUE
C
      BYPASS THE REST IF THE PLOTTING SUPPRESSION OPTION IS CALLED

      IF(IPFLG.LT.0) GO TO 980
C
C       IF THERE WAS MORE THAN ONE ELEMENT, GENERATE A COMPOSITE PLOT
C
      IF(NEL-1)  980,980,971
```

```
  971  WORDS(3)  =  73.0
       CALL LABEL(0.0,0.0,XMIN,XMAX,XLONG,IDIVX,XLABEL,40,0)
       CALL LABEL(0.0,0.0,YMIN,YMAX,YLONG,IDIVY,YLABEL,40,1)
       CALL CPLOT(RAND,NPOINT,NPOINT,WORDS,YMAX,YMIN,5)
C
C        BYPASS THIS SECTION IF THERE IS NO EXPERIMENTAL DATA
C
  980  IF(IRAW.LT.100)  GO TO 999
C
C        READ THE NUMBER OF EXPERIMENTAL POINTS AND THE MINIMUM AND
C             MAXIMUM ENERGIES OF THE EXPERIMENTAL POINTS.  ASSUME EQUAL
C             ENERGY INTERVALS BETWEEN POINTS
C
       READ(5,161)  NPT, EMIN, EMAX
  161  FORMAT(  6X, I4,2F10.2 )
C
C        WRITE THE FLAG VALUE SO WE KNOW WHY IT LOOKED FOR RAW DATA
C
       WRITE(6,162)  IRAW
  162  FORMAT('1',9X,'THE FLAG FOR PLOTTING RAW DATA WITH A',
     1   ' SYNTHESIZED PLOT IS  ',  I4, '  .' / 10X
     2   ' THIS VALUE SPECIFIES THAT SUCH A PLOT SHOULD BE MADE.'///)
C
C        WRITE THE SPECIFICATIONS OF THE RAW DATA
C
       WRITE(6,163)  NPT, EMIN, EMAX
  163  FORMAT(10X,'THE NUMBER OF CHANNELS IS ', I4, ' .' //
     1        10X,'THE ENERGY OF THE LOWEST CHANNEL IS  ', F10.3,
     2            ' KEV.'  /
     3        10X,'THE ENERGY OF THE HIGHEST CHANNEL IS  ',F10.3,
     4            '  KEV.' ///)
       WRITE(6,164)
  164  FORMAT(50X,'EXPERIMENTAL DATA'//)
C
C        DETERMINE THE NUMBER OF DATA CARDS ASSUMING 10 POINTS PER CARD
C
       NCARD  =  NPT / 10
       MPT    =  NCARD * 10
       IF(NPT-MPT)  982, 982, 981
  981  NCARD  =  NCARD + 1
  982  CONTINUE
C
C        ZERO OUT THE LOCATIONS OF THE EXPERIMENTAL DATA SINCE IT  IS
C             EQUIVALENCED WITH ANOTHER ARRAY
C
       DO  983   IPT  =  1,2000
       EXPX(IPT)   =  0.0
       EXPY(IPT)   =  0.0
  983  CONTINUE
       DO  985   ICARD  =  1, NCARD
       IPT    =  10 * ICARD
       MPT    =  IPT - 9
       IF(IPT.GT.NPT)  IPT  =  NPT

C        READ THE EXPERIMENTAL DATA STARTING WITH THE LOWEST ENERGY
C
       READ(5,165)  (EXPY(JPT),JPT=MPT,IPT)
  165  FORMAT(10F8.0)
       LPT    =  MPT - 1
C
```

```
C         WRITE THE EXPERIMENTAL DATA IN A READABLE FORMAT
C
          WRITE(6,166)  LPT, (EXPY(JPT),JPT=MPT,IPT)
  166     FORMAT(10X,I5,15X,10(F8.0,2X) )
  985     CONTINUE
C
C         NOW CALCULATE THE ENERGY OF EACH CHANNEL FOR THE EXPERIMENTAL
C               DATA BY ASSUMING EQUAL ENERGY INTERVALS
C
          PT      =  NPT - 1
          EPT     =  (EMAX-EMIN)/PT
          DO  989    IPT  =  1, NPT
          PT      =  IPT - 1
          EXPX(IPT)    =  EMIN + EPT * PT
  989     CONTINUE
C
C         READ THE LEGEND FOR THE UPPER RIGHT HAND CORNER OF THE PLOT
C               AND THE LABELS FOR THE HORIZONTAL AND VERTICAL AXES
C
          READ(5,167)  WORDS(1),WORDS(2),XLABEL,YLABEL
  167     FORMAT(2X, 2A4 / 20A4 )
C
C         NOW WRITE THE ALPHANUMERIC DATA FOR THE EXPERIMENTAL DATA PLOT
C
          WRITE(6,168)
  168     FORMAT(//)
          WRITE(6,151)
          WRITE(6,152) WORDS(1),WORDS(2)
          WRITE(6,114)  XLABEL, YLABEL
          WORDS(3)    =  73.0
C
C         PLOT THE EXPERIMENTAL DATA
C         AND THEN PLOT THE SYNTHESIZED COMPOSITE SPECTRUM AGAIN
C
          CALL LABEL(0.0,0.0,0.0,XMIN,XMAX,XLONG,IDIVX,XLABEL,40,0)
          CALL LABEL(0.0,0.0,0.0,YMIN,YMAX,YLONG,IDIVY,YLABEL,40,1)
          CALL  XYPLT(NPT,EXPX,EXPY,XMIN,XMAX,YMIN,YMAX,WORDS,0,4)
          CALL  CPLOT(RAND,NPOINT,NPOINT,WORDS,YMAX,YMIN,5)
C
C         GO BACK AND REPEAT IF THERE ARE MORE SPECTRA TO BE GENERATED
C
  999     CONTINUE
C
C         NOW QUIT AND GO HOME
C
          STOP
          END
```

```
      SUBROUTINE RANDOM( RATE, NLAYER, ANORM, NORM, PRHO )
C
C       THIS IS THE FAST VERSION OF THIS PROGRAM
C
      IMPLICIT  REAL*8(A-H,O-$),INTEGER(I-N)
      DIMENSION  SIGMA(2,2000),EDET(2000),RATE(2000)
      DIMENSION  THICK(10),ANAME(10),PRHO(10),TSAVE(10)
      REAL*4  BEAM(2000), DEEP(2000)
      REAL*4  WORDS(3),XRATE(2000),YRATE(2000),XLABEL(10),YLABEL(10)
      REAL*4  XLONG,XMIN,XMAX,YLONG,YMAX,YMIN
      COMMON/P/IPFLG
      COMMON / DP /  SIGMA,EDET
      COMMON / SP /  BEAM,DEEP
C
C       SIGMA(1,I)  WILL HOLD THE ENERGY AT THE DETECTOR AS A FUNCTION
C          OF DEPTH IN EQUAL STEPS OF DX ANGSTROMS
C       SIGMA(2,I) WILL HOLD D(SIGMA(1,I))/DX IN KEV. PER ANGSTROM
C       EDET WILL STORE THE INCREMENTED DETECTED ENERGY IN THE
C          CALCULATION OF THE BACKSCATTERING RATE
C       RATE IS THE NUMBER OF COUNTS PER INCREMENT OF DETECTED ENERGY
C
C
      COMMON /R/A(5,10),RHO(10),DX
C
C       A   IS A MATRIX HOLDING THE 5 COEFFICIENTS OF THE FITTED DE/DX
C          FOR EACH ONE OF THE 10 LAYERS ALLOWED FOR IN THE PROGRAM
C       RHO IS THE DENSITY OF EACH LAYER IN GRAMS/CM**3
C       DX IS THE INCREMENT IN DISTANCE USED TO CALCULATE SIGMA
C       PRHO IS THE PARTIAL DENSITY IN GRAMS/CM**3 OF THE ELEMENT
C          BEING CALCULATED.
C
C
      COMMON /T/ T1,T2,T3,T4,T5,T6,T7,T8,T9,T10
C
C       TN IS THE THICKNESS OF THE SAMPLE IN TO THE DEEPEST PART OF
C          LAYER N.
C
      DIMENSION  TN(10)
      EQUIVALENCE  (SIGMA(1),XRATE(1)),(SIGMA(2001),YRATE(1))
      EQUIVALENCE  (TN(1),T1),(TN(2),T2),(TN(3),T3),(TN(4),T4),
     1  (TN(5),T5),(TN(6),T6),(TN(7),T7),(TN(8),T8),(TN(9),T9),
     2  (TN(10),T10)
C
C       TN(I) IS TO FACILITATE THE CALCULATIONS WHEN
C          CROSSING AN INTERFACE
C
      COMMON/TARGET/AMASS,ZT
C
C       AMASS IS THE MASS OF THE TARGET ELEMENT IN AMU
C       ZT IS THE ATOMIC NUMBER OF THE TARGET ELEMENT
C
C
      COMMON/INPUT/EIN,EQUIT,ECHAN,THETA
C
C       EIN IS THE ENERGY OF THE INCIDENT ALPHA PARTICLE BEAM IN KEV
C       THETA IS THE BACKSCATTERING DETECTING ANGLE IN DEGREES
C       EQUIT IS THE LOWEST DETECTED ENERGY FOR WHICH CALCULATION
C          SHOULD BE MADE.   EQUIT IS ALSO IN KEV.
C       DX IS THE SIZE OF THE STEP USED IN CALCULATING THE
C          BACKSCATTERED ENERGY AS A FUNCTION OF  TARGET DEPTH
```

```
C         ECHAN IS THE ENERGY PER CHANNEL IN CALCULATING THE
C            BACKSCATTERED SPECTRUM
          ANORM IS THE NORMALIZATION TO BE USED IN CALCULATING THE
C            HEIGHT OF THE RANDOM SPECTRUM, AS SPECIFIED BY 'NORM'
C         NORM DETERMINES HOW ANORM IS TO BE HANDLED IN THE PROGRAM
C              IF NORM < 0 , THEN ANORM IS TO BE IGNORED
C              IF NORM = 0 , THEN ANORM IS A PREVIOUSLY DETERMINED FACTOR
C              IF NORM > 0 , THEN ANORM IS THE NUMBER OF COUNTS IN THE
C                   HIGHEST FILLED CHANNEL, AND THE SPECTRUM IS TO BE
C                   NORMALIZED TO THAT VALUE
C
C
C
C         THE FOLLOWING PART OF THE PROGRAM IS TO READ IN THE DATA
C            THAT SPECIFIES THE CHARACTERISTICS OF EACH LAYER
C
      COMMON/SIZE/XLABEL, YLABEL, WORDS, XMIN, XMAX, XLONG,
     1   YMIN, YMAX, YLONG, IDIVX, IDIVY
C
C         THE FOLLOWING SECTION IS TO SET INITIAL VALUES OF VARIABLES
C
      NLAYER = MIN0(NLAYER, 10)
      WRITE(6,800)
  800 FORMAT('1')
      TNN    = TN(NLAYER) + DX
      DEL    = DMOD(TNN,DX)
      TNN    = TN(NLAYER) + DEL
      NLAY   = NLAYER + 1
      DO  439  I = NLAY, 10
      TSAVE(I)  =  TN(I)
      TN(I)     =  TNN
  439 CONTINUE
      DO  349   I  =  1,2000
      SIGMA(1,I)  =  0.0
      SIGMA(2,I)  =  0.0
      EDET(I)     =  0.0
      RATE(I)     =  0.0
      BEAM(I)     =  0.0
      DEEP(I)     =  0.0
  349 CONTINUE
      LAYER = 1
      LSAVE  =  1
      HEMASS =  4.0
      PI     =  3.14159D0
      ATHETA = PI * THETA / ( 0.18D3 )
      ALPHA  = ALF(ATHETA,AMASS,HEMASS)
      EOUTR  = ALPHA*EIN
      X      =  0.0D0
      DE     =  0.0D0
C
C       ITHICK IS THE NUMBER OF STEPS TO BE TAKEN IN GENERATING SIGMA
C
      ITHICK =  T10/DX  + 1.0D0

C       IF ITHICK IS TOO LARGE, IT IS ARBITRARILY MADE EQUAL TO 1000
C
      IT     =  MIN0(ITHICK,1000 )
      SIGMA(1,1)  =  EOUTR
      E      =  EIN
C
```

```
C         THE FOLLOWING SECTION ITERATES AND GENERATES THE VALUES OF
C            THE ENERGY AT THE DETECTOR FOR BACKSCATTERED PARTICLES

      DO  299  ITER  = 2,IT
      TER    =  ITER -1
      X      =  TER*DX
      DE  =  DX*ELOSS(E,LAYER)*RHO(LAYER)*1.0D-05
      E   =   E + DE
      IF(X.GT.T9 .AND.X.LE.T10)      LAYER = 10
      IF(X.GT.T8 .AND.X.LE.T9 )      LAYER = 9
      IF(X.GT.T7 .AND.X.LE.T8 )      LAYER = 8
      IF(X.GT.T6 .AND.X.LE.T7 )      LAYER = 7
      IF(X.GT.T5 .AND.X.LE.T6 )      LAYER = 6
      IF(X.GT.T4 .AND.X.LE.T5 )      LAYER = 5
      IF(X.GT.T3 .AND.X.LE.T4 )      LAYER = 4
      IF(X.GT.T2 .AND.X.LE.T3 )      LAYER = 3
      IF(X.GT.T1 .AND.X.LE.T2 )      LAYER = 2
      IF(X.GE.0.0.AND.X.LE.T1 )      LAYER = 1
      IF(LAYER.EQ.LSAVE)    GO TO 355
      E      =  E + DE
      X      =  X + DX
      DX1    =  TN(LSAVE) - X
      DE1    =  DX1*ELOSS(E,LSAVE)*RHO(LSAVE)*1.0D-05
      E      =  E + DE1
      X      =  X + DX1
      DX2    =  DX - DX1
      DE2    =  DX2*ELOSS(E,LAYER)*RHO(LAYER)*1.0D-05
      E      =  E + DE2
      X      =  X  +  DX2
  355 EBACK  =  E * ALPHA
      LSAVE  =  LAYER
      BEAM(ITER)  =  E
      XX     =  X
      EQOUT  =  EQUT(EBACK,X,ATHETA)
      SIGMA(1,ITER) =  EQOUT
      X      =  XX
      LAYER  =  LSAVE
      SIGMA(2,ITER) = (SIGMA(1,ITER-1) - SIGMA(1,ITER))/DX
      IF(SIGMA(1,ITER).LT.EQUIT)  GO TO 998
      IF(LAYER.GT.NLAYER)            GO TO 998
      IF(X.GT.T10)                   GO TO 999
C
C
C         SIGMA(1,I) = ENERGY AT THE DETECTOR AS A FUNCTION OF DEPTH
C            IN STEPS OF DX  AS SPECIFIED PREVIOUSLY
C
C         SIGMA(2,I) = D(SIGMA(1,I))/DX IN STEPS OF DX IN WIDTH
C
C
      GO TO 299
C
C         WHEN THE BACKSCATTERED ENERGY HAS FALLEN BELOW EQUIT,
C            BRANCH OUT OF THE LOOP

  998 IT     =  ITER
      EQUIT  =  DMAX1( EQUIT, EQOUT  )
C
C         IF THE LOOP IS BEING LEFT BECAUSE T10 HAS BEEN EXCEEDED,
C            REDEFINE EQUIT TO BE THE BACKSCATTERED ENERGY FROM THE
C            DEEPEST PART OF THE SAMPLE
```

```
C
  999  EQUIT  =  DMAX1( EQUIT, EQOUT  )
C
C        BRANCH OUT OF THE LOOP
C
       IIER  =  IT + 1
  299  CONTINUE
       EQUIT  =  DMAX1( EQUIT, EQOUT  )
C
C        THE FOLLOWING PERFORMS A LINEAR FIT TO FIND A BEST VALUE OF
C           SIGMA(2,1)
C
       SIGMA(2,1)  =  2.0D0 * SIGMA(2,2) - SIGMA(2,3)
       BEAM(1)     =  EIN
       WRITE (6,601)
  601  FORMAT (10X,'DEPTH',13X,'EOUT',15X,'SIGMA',15X,'EBEAM'//)
       ITT    =  IT + 1
       DO  298  L= 1,ITT
       EL     =  L - 1
       R      =  EL * DX
       WRITE(6,602) R,SIGMA(1,L),SIGMA(2,L)  ,BEAM(L)
  602  FORMAT( 8X, F7.0,10X,F10.4,10X,F10.7,10X,F10.4)
  298  CONTINUE
C
C        FRONT IS THE NORMALIZING VALUE FOR THE SPECTRUM HEIGHT
C
       FRONT  =  1.0D8

C        MINCHN IS THE LOWEST CHANNEL TO BE FILLED WITH BACKSCATTERED
C        COUNTS
C
       MINCHN =  EQUIT/ECHAN + 1.0D0
C
C        MXCHN IS THE HIGHEST CHANNEL TO BE FILLED WITH COUNTS
C
       MAXCHN =  EIN/ECHAN + 1.0D0
       MXCHN  =  MIN0( 2000,MAXCHN )
       CHNMX  =  MXCHN
       NCHAN  =  MXCHN - MINCHN
C
C        EMXCHN IS THE ENERGY OF THE HIGHEST CHANNEL
C
       EMXCHN =  CHNMX * ECHAN
       IF(EMXCHN - EIN )  840, 850, 850
  840  WRITE ( 6,841 )  EIN, EMXCHN
  841  FORMAT( '1',10X,'ERROR,  THE BEAM ENERGY IS ',F10.4,' KEV WHILE
     1THE ENERGY OF THE HIGHEST CHANNEL IS ', F10.4, ' KEV, ' / '1' )
C
C        EMAX IS THE MAXIMUM POSSIBLE BACKSCATTERED ENERGY
C
  850  EMAX   =  EIN * ALPHA
C
C        EBEAM IS THE BEAM ENERGY AND WILL CHANGE WITH DEPTH

       EBEAM  =  EIN
C
C        MAXECN IS THE HIGHEST COMPLETELY FILLED CHANNEL
C
       MAXECN =  EMAX / ECHAN
       CNMAXE =  MAXECN
```

```
C
C         MAXE IS THE CHANNEL JUST ABOVE MAXECN AND WILL CONTAIN SOME
C            SPILLOVER SINCE K**2  * EIN IS NOT NECESSARILY GOING TO
C            FALL AT THE EDGE OF A CHANNEL
C
          MAXE   =  MAXECN + 1
C
C         ESTEP1 AND DEX1 ARE USED TO CALCULATE THE COUNT RATE INTO
C            CHANNEL MAXE
C
          ESTEP1 =  EMAX - CNMAXE * ECHAN
          DEX1   =  ESTEP1/ SIGMA(2,1)
C
C         X AND EXX ARE THE PENETRATION DEPTH OF THE BEAM INTO THE TARGET
C
          X      =  DEX1
C
C         DEN1 IS THE ENERGY LOSS OF THE BEAM IN GOING THROUGH DEX1
C
          DEN1   =  DEX1*ELOSS(EBEAM,1)*RHO(1)*1.0D-05
C
C         AREA IS THE NORMALIZED CROSSSECTION FACTOR  THAT CORRECTS FOR
C            THE CHANGE FROM CM FRAME TO LAB FRAME
C
          AREA   =  CROSS( HEMASS, AMASS, ATHETA )
C
C         THE FOLLOWING SECTION LOADS THE OTHERWISE UNUSED CHANNELS
C            WITH ZEROES
C
          DO  159     ICHAN  =  1, MXCHN
          BEAM(ICHAN)    =  0.0D0
  159     CONTINUE
C
C         THIS SECTION IS TO CALCULATE THE RATE INTO CHANNEL MAXECN
C
          EBEAM  =  EBEAM - DEN1
          BEAM(MAXE)     =  EBEAM
          DEEP(MAXE)  =  DEX1
          IX     =  X / DX + 2.0D0
          DEX    =  ECHAN / SIGMA( 2, IX )
          RATE(MAXECN) = DEX*PRHO(1)* ZT*ZT *AREA*FRONT/(AMASS*EBEAM*EBEAM)
C
C         THE PROPER NORMALIZATION FOR THE RATE IS NOW DETERMINED FROM
C            THE ENTERED VALUE OF NORM
C
C         RECALL THAT IF NORM < 0 , THE  SPECTRUM IS NOT TO BE NORMALIZED
C            BUT FOR NORM = 0 , THE NORMALIZATION VALUE IS PREDETERMINED
C            AND IF NORM > 0 , THE NORMALIZATION VALUE MUST BE CALCULATED
C
          IF( NORM )   559, 555, 551
  551     FRONT  =  ANORM * 1.0D8 / RATE(MAXECN)
          RATE(MAXECN) = ANORM
          GO TO 559
  555     FRONT  =  ANORM
          RATE(MAXECN) = FRONT * RATE(MAXECN) / 1.0D8
C
C         FACTOR IS A COMMON FACTOR THAT IS ALWAYS USED
C
  559     FACTOR =  ZT * ZT * AREA * FRONT / AMASS
C
```

```
C         THE FOLLOWING CALCULATES THE RATE INTO CHANNEL MAXE,
C            THE HIGHEST CHANNEL WITH DATA, BUT IT IS AN UNFILLED CHANNEL

      RATE(MAXE)  =  DEX1 * PRHO(1) * FACTOR / EIN / EIN
      LAYER  =  1
      LSAVE  =  LAYER
      EDET(MAXE)  =  EMAX - SIGMA(2,2) * DEX1
      EBEAM  =  EBEAM-DEX*ELOSS(EBEAM,1)*RHO(1)*1.0D-05
      BEAM(MAXECN)  =  EBEAM
      X      =  X + DEX
      DEEP(MAXECN)  =  X
      IX     =  X / DX + 2.0D0
      XMOD   =  DMOD( X, DX )
      IXY    =  IX-1
      EDET(MAXECN)  =  SIGMA(1,IXY)- SIGMA(2,IX) * XMOD
      IE     =  MAXECN
C
C         THE SECTION TO STATEMENT 579 CALCULATES THE RANDOM SPECTRUM
C            CONTRIBUTION FOR THIS PARTICULAR ELEMENT FOR CHANNELS
C            LOWER THAN MAXECN
C
  571 IE     =  IE - 1
      DEX    =  ECHAN / SIGMA( 2, IX )
      DEN    =  DEX * ELOSS(EBEAM,LAYER) * RHO(LAYER) * 1.0D-05
      RATE(IE)    =  DEX * PRHO(LAYER) * FACTOR / EBEAM / EBEAM
      EBEAM  =  EBEAM - DEN
      X      =  X + DEX
      IF(X.GE.T9 .AND.X.LE.T10)     LAYER = 10
      IF(X.GE.T8 .AND.X.LT.T9 )     LAYER = 9
      IF(X.GE.T7 .AND.X.LT.T8 )     LAYER = 8
      IF(X.GE.T6 .AND.X.LT.T7 )     LAYER = 7
      IF(X.GE.T5 .AND.X.LT.T6 )     LAYER = 6
      IF(X.GE.T4 .AND.X.LT.T5 )     LAYER = 5
      IF(X.GE.T3 .AND.X.LT.T4 )     LAYER = 4
      IF(X.GE.T2 .AND.X.LT.T3 )     LAYER = 3
      IF(X.GE.T1 .AND.X.LT.T2 )     LAYER = 2
      IF(X.GE.0.0.AND.X.LT.T1 )     LAYER = 1
C
C     THE FOLLOWING SECTION IS TO CALCULATE THE SPECTRUM WHEN
C        A STEP THAT CORRESPONDS TO AN ENERGY WIDTH OF ECHAN
C        SPANS AN INTERFACE BETWEEN LAYERS.
C
C     DO NOT EXECUTE IF THERE IS NO INTERFACE
C
      IF(LAYER.EQ.LSAVE)  GO TO 573
C
C     RESTORE THE VALUES BEFORE CROSSING THE INTERFACE
C
      X      =  X - DEX
      EBEAM  =  EBEAM + DEN
C
C     CALCULATE THE EFFECT OF THE PART BEFORE CROSSING THE INTERFACE
C
      DEX1   =  TN(LSAVE) - X
      DEN1   =  DEX1*ELOSS(EBEAM,LSAVE)*RHO(LSAVE)*1.0D-05
      PRATE1 =  DEX1*PRHO(LSAVE)/(EBEAM*EBEAM)
      EBEAM  =  EBEAM - DEN1
      X      =  X + DEX1
      DOUT   =  DEX1 * SIGMA(2,IX-1)
      IX     =  X/DX + 2.0D0
```

```
C
C       CALCULATE THE CONTRIBUTION AFTER CROSSING THE INTERFACE
C
        IF(SIGMA(2,IX+1).EQ.0.0)   DEX2   =  (ECHAN-DOUT)/SIGMA(2,IX)
        IF(SIGMA(2,IX+1).NE.0.0)   DEX2   =  (ECHAN-DOUT)/SIGMA(2,IX+1)
        DEN2   =  DEX2*ELOSS(EBEAM,LAYER)*RHO(LAYER)*1.0D-05
        PRATE2 =  DEX2*PRHO(LAYER)/(EBEAM*EBEAM)
C
C       LOAD THE 'NORMAL' VARIABLES WITH THE VALUES CALCULATED BY THIS
C          INTERFACE-SPANNING ROUTINE
C
        RATE(IE)  =  (PRATE1 + PRATE2)*FACTOR
        EBEAM  =  EBEAM-DEN2
        X      =  X + DEX2
        DEN    =  DEN1 + DEN2
        DEX    =  DEX1 + DEX2
  573   CONTINUE
        LSAVE  =  LAYER
        IX     =  X / DX + 2.0D0
        XMOD   =  DMOD( X, DX )
        IXY    =  IX-1
        EDET(IE)    =  SIGMA(1,IXY)- SIGMA(2,IX) * XMOD
        BEAM(IE)    =  EBEAM
        DEEP(IE)    =  X
        IF(X.GT.TN(NLAYER)      )     GO TO 579
        IF(LAYER.GT.NLAYER)           GO TO 579
        IF(EDET(IE).LT.EQUIT)         GO TO 579
        IF( IE - MINCHN )  579, 579, 571
  579   CONTINUE
        WRITE(6,590)  FRONT, NORM
  590   FORMAT('1', '  THE NORMALIZING FACTOR USED IN THIS SPECTRUM WAS',
     1  2X,F15.4,' FOR A VALUE OF NORM = ', I4, ',' , /// )
        ANORM  =  FRONT
        NORM   =  0
        WRITE( 6, 580 )
  580   FORMAT(13X,'CHANNEL',21X,'EDET',24X,'RATE',19X,'EBEAM',18X,
     1    'DEPTH'//)
        KMINC  =  MXCHN  - MAXE - 10
        KMAXC  =  NCHAN + 5
        DO  650   KA  =  KMINC,KMAXC
        M      =  MXCHN - KA
        WRITE(6,581) M, EDET(M), RATE(M), BEAM(M), DEEP(M)
  581   FORMAT( 15X, I4, 2( 14X, F15.6 ) ,2(9X,F15.6))
  650   CONTINUE
        WRITE(6,800)
        MINX   =  EQUIT/ECHAN
        MINXX  =  MINX + 2
        MAXX   =  EMAX/ECHAN + 0.999
        NX     =  MAXX - MINX + 3
        DO  698   NR  =  MINXX, MAXX
        MR     =  NR - MINX + 2
        XRATE(MR)    =  EDET(NR)
        YRATE(MR)    =  RATE(NR)
  698   CONTINUE
        XRATE(3)  =  EDET(MINXX) -   ECHAN
        YRATE(3)  =  RATE(MINX+1)
        XRATE(2)  =  EDET(MINXX) - 2*ECHAN
        YRATE(2)  =  RATE(MINX)
        XRATE(1)  =  EDET(MINXX) - 3*ECHAN
        YRATE(1)  =  0.0
```

```
      MR      =  MR + 1
      XRATE(MR) =  EDET(MAXX) + ECHAN
      YRATE(MR) =  0.0
      WORDS(3)  =  73.0
C
C       BYPASS IF PLOTTING IS TO BE SUPPRESSED
C
      IF(IPFLG.LT.0) GO TO 389
      CALL  LABEL( 0.0, 0.0,XMIN,XMAX,XLONG,IDIVX,XLABEL,40,0)
      CALL  LABEL( 0.0, 0.0,YMIN,YMAX,YLONG,IDIVY,YLABEL,40,1)
      CALL  XYPLOT(NX,XRATE,YRATE,XMIN,XMAX,YMIN,YMAX,WORDS,5)
  389 CONTINUE
      WRITE(6,800)
      DO  440   I  =  NLAY, 10
      TN(I)  =  TSAVE(I)
  440 CONTINUE
      RETURN
      END
```

```
      FUNCTION  ALF(AT,AM,AI)
      IMPLICIT  REAL*8(A-H,O-$),INTEGER(I-N)

C        ALF IS A FUNCTION THAT CALCULATES THE RATIO OF INCOMING ENERGY
C           TO OUTGOING ENERGY FOR ELASTIC SCATTERING ASSUMING THE
C           INCIDENT PARTICLE HAS A MASS OF 4
C
C        AT IS THE LABORATORY ANGLE BETWEEN THE INCIDENT DIRECTION OF
C           THE PARTICLE AND THE OUTGOING DIRECTION OF THE PARTICLE
C
C
C        AI IS THE MASS OF THE INCIDENT PARTICLE, PREFERABLY IN AMU.
C
C        AM IS THE MASS OF THE TARGET PARTICLE IN THE SAME UNITS AS
C           THE INCIDENT PARTICLE.
C
      C     =  DCOS(AT)
      S     =  DSIN(AT)
      AM2   =  AM * AM
      AI2   =  AI * AI
      AA    =  ( AM + AI ) * ( AM + AI )
      D     =  DSQRT( AM2 / AI2 - S * S )
      ALF   =  AI2 / AA * ( C + D ) * ( C + D )
      RETURN
      END
```

```
      FUNCTION  CROSS( AI, AT, THETA )
      IMPLICIT REAL*8(A-H,O-$),INTEGER(I-N)

C       CROSS CALCULATES THE CORRECTIONS TO THE CENTER OF MASS
C          RUTHERFORD CROSSSECTION DUE TO THE FINITE MASS OF THE
C          TARGET NUCLEUS AND THE EXIT ANGLE OF THE PROBE PARTICLE
C
C
C       IT SHOULD BE NOTED THAT THIS PROGRAM WILL NOT WORK FOR ANGLES
C          VERY CLOSE TO 0 DEGREES OR VERY CLOSE TO 180 DEGREES
C
C
C       THE FORMULA USED IN THE CALCULATION OF THE EXACT CROSSSECTION
C          CAN BE FOUND IN TUROS & WILHELMI AND IN ZIEGLER
C
C
C       ONE AND TWO ARE DEFINED AS DOUBLE PRECISION NUMBERS
C
      ONE    =  1.0
      TWO    =  2.0
      FOUR   =  4.0
C
C
C       AI   IS THE MASS OF THE INCIDENT PARTICLE IN NATURAL UNITS
C
C       AT IS THE MASS OF THE TARGET PARTICLE IN THE SAME UNITS AS AI
C


C       C, S AND HAFSIN SACRIFICE STORAGE EFFICIENCY TO MINIMIZE THE
C          CALLING OF THE SUBROUTINES FOR CALCULATING SINES AND COSINES
C
      C      =  DCOS(THETA)
      S      =  DSIN(THETA)
      HAFANG =  THETA / TWO
      HAFSIN =  DSIN(HAFANG)
C
C
C       SQ IS A FACTOR THAT APPEARS IN THE CROSSSECTION UNDER A
C          SQUARE ROOT AND INCLUDES MOST OF THE MASS CORRECTIONS
C
      SQ     =  AI * S / AT
      SQ     =  DSQRT( ONE - SQ * SQ )
C
C
C       ANUM IS THE NUMERATOR OF THE EXPRESSION FOR THE CROSSSECTION
C
      C      =  C + SQ
      ANUM   =  C * C
C
C
C       DEN IS THE DENOMINATOR IN THE EXPRESSION OF THE CROSSSECTION
C
      DEN    =  SQ * S*S*S*S
C
C
C       DSIG IS THE MASS AND ANGLE DEPENDENT PART OF THE DIFFERENTIAL
C          CROSSSECTION, AND DOES NOT INCLUDE THE DEPENDENCE ON THE
C          INCIDENT ENERGY OR THE CHARGE OF THE TARGET
C
```

```
      DSIG   =  FOUR * ANUM / DEN
C
C
C        CROSS NORMALIZES THE EXACT DIFFERENTIAL CROSSSECTION TO THE
C           CLASSICAL FORMULA FOR AN INFINITELY MASSIVE TARGET
C
      CROSS  =  DSIG * HAFSIN * HAFSIN * HAFSIN * HAFSIN
      RETURN
      END
```

```
      FUNCTION  ELOSS(E,L)
      IMPLICIT  REAL*8(A-H,O-$),INTEGER(I-N)

C       THE FUNCTION ELOSS USES THE POLYNOMIAL FIT TO EXPERIMENTAL
C          DATA TO GENERATE A VALUE OF DE/DX AT A GIVEN ENERGY.
C
C       IN THIS CASE,  THE POLYNOMIAL IS TRANSMITTED BY THE COMMON
C          STATEMENT.
C
C       L INDEXES THE LAYER BEING CONSIDERED AND SELECTS THE PROPER
C          POLYNOMIAL OF THE SEVERAL AVAILABLE FOR THIS PROGRAM
C
C       E IS THE ENERGY AT WHICH THE POLYNOMIAL IS TO BE EVALUATED
C
      COMMON /R/A(5,10),RHO(10),DX
      ELOSS=A(1,L)+A(2,L)*E+A(3,L)*E**2+A(4,L)*E**3+A(5,L)*E**4
      RETURN
      END
```

```
      FUNCTION  EOUT(E,X,THETA)
      IMPLICIT  REAL*8(A-H,O-$),INTEGER(I-N)
C
C     THE PROGRAM EOUT IS USED TO CALCULATE THE EXIT ENERGY OF THE
C        PARTICLE BEING BACKSCATTERED FROM A GIVEN DEPTH
C
C     E IS THE ENERGY OF THE PARTICLE AFTER BACKSCATTERING
C
C     X IS THE DEPTH FROM WHICH THE PARTICLE IS BEING BACKSCATTERED
C
C     THETA IS THE SCATTERING ANGLE OF THE PARTICLE TO ALLOW FOR THE
C        INCREASED PATH LENGTH WHEN THE BACKSCATTERING DIRECTION IS
C        NOT PARALLEL TO THE INCIDENT DIRECTION
C
C     THE FUNCTION CALCULATES THE EXIT ENERGY BY MARCHING THE
C        PARTICLE OUT OF THE TARGET IN SMALL STEPS AND CALCULATING
C        THE ENERGY LOST IN EACH STEP UNTIL THE PARTICLE HAS EMERGED
C        FROM THE TARGET
C
C
      COMMON /R/A(5,10),RHO(10),DX
      COMMON /T/ T1,T2,T3,T4,T5,T6,T7,T8,T9,T10
      DIMENSION  TN(10)
      EQUIVALENCE  (TN(1),T1),(TN(2),T2),(TN(3),T3),(TN(4),T4),
     1   (TN(5),T5),(TN(6),T6),(TN(7),T7),(TN(8),T8),(TN(9),T9),
     2   (TN(10),T10)
      C      =  -DCOS(THETA)
      IF(X.GE.T9 .AND.X.LT.T10)     LAYER = 10
      IF(X.GE.T8 .AND.X.LT.T9 )     LAYER = 9
      IF(X.GE.T7 .AND.X.LT.T8 )     LAYER = 8
      IF(X.GE.T6 .AND.X.LT.T7 )     LAYER = 7
      IF(X.GE.T5 .AND.X.LT.T6 )     LAYER = 6
      IF(X.GE.T4 .AND.X.LT.T5 )     LAYER = 5
      IF(X.GE.T3 .AND.X.LT.T4 )     LAYER = 4
      IF(X.GE.T2 .AND.X.LT.T3 )     LAYER = 3
      IF(X.GE.T1 .AND.X.LT.T2 )     LAYER = 2
      IF(X.GE.0.0.AND.X.LT.T1 )     LAYER = 1
      LSAVE  =  LAYER
    1 CONTINUE
      DE     =  DX*ELOSS(E,LAYER)*RHO(LAYER)*1.0D-05
      D      =  DE/C
      E      =  E - D
      X = X - DX
      IF(X.GE.T9 .AND.X.LT.T10)     LAYER = 10
      IF(X.GE.T8 .AND.X.LT.T9 )     LAYER = 9
      IF(X.GE.T7 .AND.X.LT.T8 )     LAYER = 8
      IF(X.GE.T6 .AND.X.LT.T7 )     LAYER = 7
      IF(X.GE.T5 .AND.X.LT.T6 )     LAYER = 6
      IF(X.GE.T4 .AND.X.LT.T5 )     LAYER = 5
      IF(X.GE.T3 .AND.X.LT.T4 )     LAYER = 4
      IF(X.GE.T2 .AND.X.LT.T3 )     LAYER = 3
      IF(X.GE.T1 .AND.X.LT.T2 )     LAYER = 2
      IF(X.GE.0.0.AND.X.LT.T1 )     LAYER = 1
      IF(X.LT.0.0)                  LAYER = 0
      IF(LAYER.EQ.LSAVE)            GO TO 49
      E      =  E + D
      X      =  X + DX
      IF(LAYER.LE.0)                DX1  =  X
      IF(LAYER.GE.1)                DX1  =  X - TN(LAYER)
      DE1    =  DX1*ELOSS(E,LSAVE)*RHO(LSAVE)*1.0D-05
```

```
      E      =  E - DE1 / C
      X      =  X - DX1
      IF(LAYER,LE,0)  GO TO 99
      DX2    =  DX - DX1
      DE2    =  DX2*ELOSS(E,LAYER)*RHO(LAYER)*1.0D-05
      E      =  E - DE2 / C
      X      =  X - DX2
   49 LSAVE  =  LAYER
      IF(X,LE,0,0)                        GO TO 99
      GO TO 1
   99 EOUT = E
      RETURN
      END
```

A.4 Example of a DATA deck.

In order to make the section on using this program(A.2) seem more meaningful, a listing of the DATA deck for a real case is included. The example that has been chosen is the deck used to generate the middle spectrum in Figure 3.7. This is a sample of α-Fe_2O_3 on Fe on a thermally oxidized substrate. The spectrum was taken using an incident beam energy of 1508 keV and a laboratory scattering angle of 168°.

In the first card, the program is told that the calculations will be performed for a three-layer sample(Fe_2O_3/Fe/SiO_2) and that the signals from three target elements will be calculated. The beam energy of 1508 keV is specified as the next parameter, as is the quitting energy of 200 keV(this is the same as the default value). The scattering angle is set at 168°. The channel width to be used in calculating the backscattered particle yields is set at 2.00 keV. The size of the step the program is to take in the first pass, when it sets up its internal table of incoming and detected particle energies as a function of depth, is set at 20 Å. The normalization value is 6100; since the normalization flag is positive, the program adjusts the yield of the highest energy channel completely representing the interior of the target to be 6100 counts per channel.

The plotter label on the second card gives the letters to be written on the composite calculated plot in the upper right hand corner of the plot. The left edge of the horizontal axis is set at 100 keV and it is guaranteed that 1500 keV will appear inside the right edge of the abscissa. The maximum value to be plotted on the ordinate is set at 20000 counts per channel. Since the Experimental Data flag

is over 100, the program will plot the final synthesized spectrum twice. It will then look for some experimental data to superimpose over the calculated spectrum. Since the last flag(plot?) is not negative, all of the spectral signals will be plotted by the program.

The third card gives the label for the horizontal axis as " FE203 ON FE AT 1.50 MEV" and there is no vertical axis label. This label will appear on the final synthesized spectrum.

Since the first card specified three layers, there must be three cards in the next set, one for each layer. The first entry on the first card specifies the density of the Fe_2O_3 layer as 5.24 grams/cm^3. The next five entries give the polynomial coefficients for the energy loss in the layer(if the program is changed to accept either the polynomials of Ziegler and Chu or the parameters of Brice, this must be changed). The name of the layer is "HEM+00" and this will be written in the table headings when the program informs the user of the total depth into the target for each layer. The thickness of this Fe_2O_3 layer is specified as 1100 $\mathring{A}$.

The next two cards give the same type of information for the 1900 $\mathring{A}$ Fe layer and the 3000 $\mathring{A}$ SiO_2 layer "thickness"(this was set at this value for economic considerations).

Since the first card also stated that there are three elemental signals to be calculated, there must be nine more data cards, three for each layer. In card #7, the mass of this element and its atomic number are given. The name of the element is included so the

card will be a little meaningful to the casual observer. In addition, the name of the element is also written in the upper right hand corner of the plot of the signal from this first element. Card #8 gives the concentration of this element in each layer in gm/cm^3; the program is smart enough to stop its calculations for this element after layer #2 even though there is a layer #3 in this sample; this was included as a money saving feature. The last card in this set(#9) gives the horizontal and vertical axies labels for the plot of the signal from this element. Note that even if the Plot? flag is set negative so this plot will be suppressed, this card must still be included; it can be left blank.

Cards#10-12 give the same specifications for the second element(oxygen) while cards # 13-15 give the same types of parameters for the third and final element(silicon).

Since the second card told the program to expect some experimental data, the next card set must be included. This card tells the program that there are 512 channels of experimental data and that the energy of the lowest channel is 295.6 keV with the energy of the highest channel at 1437.1 keV. Since the program was told that there are 512 channels of data, the next 52 cards must contain that data(the program figures out by itself that it must read 52 data cards). The next card("31-24-2", Card #69) gives the information to be written in the upper right hand corner of the plot containing both the calculated and experimental spectra, while the last card gives the labels for the horizontal and vertical axes in that final plot.

CARD #1

Number of layers	Number of target elements	Beam energy (keV)	Quitting energy (keV)	laboratory angle	Channel width (keV)	step size Å	Normalization value	Normalization flag
3	3	1508.0	200.0	168.0	2.00	20.0	6100.0	10

CARD #2

Plotter label	Energy Axis(Hor) (keV) min	Energy Axis(Hor) (keV) max	Vertical Axis maximum (counts/chan)	Experimental data?	Plot?
HEM-FE+0	100.0	1500.0	20000.0	512	512

CARD #3

Horizontal Axis Label(in plot)

Vertical Axis Label(in plotted output) (for synthesized spectrum)

FE2O3 ON FE AT 1.50 MEV

CARDS 4-6(the number of cards MUST match the number of layers in Card #1)

Layer 1 Density	[Card #4] Polynomial coefficients for layer dE/pdx				Layer name	Layer thickness(Å)
5.24	6.2859E 02	1.9750E 00	-2.0524E-03	8.0201E-07-1.1319E-10	HEM+00	1100.0

Layer 2 Density gm/cm^3	[Card #5]					
7.86	0.5396E 03	0.1388E 01	-0.1328E-02	0.4651E-06-0.5719E-10	FE+00	1900.0

Layer 3	[Card #6]					
2.660	0.6860E 02	0.4361E 01	-0.3561E-02	0.7603E-06 0.5799E-10	SI02	3000.0

CARDS 7-15: Three sets of 3 cards each. There MUST be one set of three cards for each target element; the number of target elements is specified as the second parameter in CARD #1

There must be three cards for the first element. [Card #7]

Mass (amu)	Atomic number	Name of the Element
55.847	26.00	IRON

Partial density of this element(iron) in each layer in gm/cm^3 [Card #8]

1	2	3	4	5	6	7	8	9	10
3.67	7.86	0.0	0.0	0.0	0.0	0.0	0.0	0.0	0.0

Labels for the axes of the plots of the calculated signal for the first element(iron)

Horizontal Axis Label	Vertical Axis Label
FE IN FE2O3-FE AT 1508 KEV	COUNTS PER CHANNEL

[Card #9]

There must also be three cards for the second element.

Information about the second element [Card #10]

16.00	8.00	OXYGEN

Partial densities of this second element in each layer. [Card #11]

1.57	0.0	1.42	0.0	0.0	0.0	0.0	0.0	0.0	0.0

Labels for the axes [Card # 12]

OXYGEN IN FE2O3-FE AT 1508.0 KEV	COUNTS PER CHANNEL

There must also be three cards to specify the data on the third element.

[Card #13]

```
          28.086    14.00      SILICON
```

Partial densities of the third element in each layer. [Card #14]

```
  0.0       0.0       1.24      0.0       0.0       0.0       0.0       0.0       0.0       0.0
```

Label for the axes

[Card #15]

```
SILICON UNDER FE2O3-FE AT 1.508 MEV      COUNTS PER CHANNEL
```

-157-

CARD # 16

512 number of channels · 295.6 Energy in keV of lowest channel · 1437.1 Energy in keV of highest channel

CARDS 17-68

These cards contain the experimental to be plotted (as requested by "Experimental Data?" in card #2. The number of data cards to be read is determined by the number of channels specified in Card #16.

17	839,	117,	6833,	8787,	8748,	8389,	7872,	7693,	7217,	6968,
18	6460,	6321,	5923,	5689,	5426,	5265,	5007,	4997,	4713,	4601,
19	4481,	4521,	4304,	4258,	4124,	4078,	3984,	3875,	3952,	3826,
20	3912,	3747,	3776,	3858,	3714,	3644,	3764,	3611,	3721,	3646,
	3635,	3500,	3501,	3647,	3603,	3604,	3457,	3488,	3468,	3427,
	3419,	3429,	3411,	3376,	3284,	3374,	3312,	3303,	3272,	3322,
	3306,	3389,	3331,	3286,	3212,	3290,	3202,	3318,	3314,	3358,
	3396,	3344,	3539,	3573,	3457,	3711,	3757,	3790,	3960,	3838,
25	3896,	3935,	3943,	3844,	3867,	3730,	3771,	3911,	3748,	3704,
	3616,	3672,	3548,	3395,	3404,	3299,	3308,	3191,	3084,	2935,
	2751,	2705,	2631,	2444,	2183,	2107,	2005,	1870,	1843,	1704,
	1558,	1464,	1366,	1298,	1061,	870,	754,	582,	551,	441,
	325,	288,	283,	255,	223,	221,	218,	228,	233,	231,
30	210,	219,	185,	223,	227,	202,	207,	225,	199,	210,
	210,	220,	217,	227,	214,	216,	195,	234,	205,	187,
	226,	228,	226,	175,	190,	205,	200,	222,	216,	187,
	220,	193,	190,	212,	218,	196,	210,	200,	197,	214,
	218,	241,	208,	222,	230,	233,	246,	254,	276,	296,
35	310,	300,	404,	383,	423,	478,	491,	565,	658,	717,
	825,	920,	1104,	1307,	1430,	1695,	1966,	2204,	2690,	3034,
	3420,	3741,	4229,	4854,	5449,	5921,	6473,	7130,	7638,	8170,
	8668,	9076,	9743,	10132,	10603,	10905,	11159,	11902,	11627,	12109,
	12578,	12526,	12875,	13039,	12686,	12912,	13074,	13217,	13231,	13291,
40	13042,	13201,	13063,	13075,	13284,	12925,	13110,	13270,	13051,	13131,
	13124,	12847,	12909,	12857,	12960,	12941,	12853,	12616,	12746,	12666,
	12794,	12722,	12509,	12745,	12512,	12678,	12702,	12668,	12729,	12446,
	12416,	12605,	12635,	12454,	12380,	12579,	12452,	12437,	12356,	12498,
	12363,	12139,	12294,	12257,	12105,	12240,	12197,	12322,	12283,	12252,
45	12044,	12076,	12096,	12052,	11987,	11908,	12039,	11943,	12042,	11965,
	11890,	11929,	11955,	11798,	11579,	11689,	11679,	11850,	11664,	11605,
	11698,	11663,	11581,	11577,	11498,	11326,	11255,	11077,	11130,	10774,
	10608,	10677,	10530,	10289,	10162,	9798,	9644,	9466,	9125,	8729,
	8579,	8347,	7916,	7985,	7636,	7445,	7371,	7098,	6953,	6750,
50	6879,	6788,	6699,	6547,	6591,	6551,	6825,	6532,	6417,	6478,
	6424,	6321,	6328,	6452,	6403,	6378,	6363,	6345,	6297,	6460,
	6195,	6342,	6333,	6252,	6268,	6133,	6219,	6297,	6197,	6233,
	5959,	6019,	6035,	5935,	6010,	5833,	5810,	5531,	5483,	5169,
	4928,	4561,	4176,	3518,	2911,	2248,	1685,	1140,	780,	455,
55	296,	166,	104,	56,	38,	35,	26,	20,	15,	23,
	19,	10,	11,	16,	8,	6,	9,	12,	7,	7,
	6,	8,	10,	7,	6,	7,	8,	6,	7,	9,
	5,	7,	6,	8,	3,	10,	7,	7,	2,	8,
	3,	5,	4,	9,	6,	3,	6,	8,	5,	6,
60	6,	5,	5,	6,	2,	2,	6,	5,	6,	2,
	1,	4,	1,	3,	4,	4,	5,	2,	7,	4,
	3,	3,	1,	1,	1,	3,	3,	1,	4,	2,
	3,	4,	0,	2,	6,	1,	2,	2,	0,	4,
	2,	0,	2,	1,	6,	2,	2,	3,	4,	2,
65	1,	5,	3,	5,	3,	7,	4,	4,	3,	1,
	1,	7,	0,	1,	0,	1,	4,	2,	9,	0,
	2,	2,	4,	4,	2,	4,	6,	3,	6,	4,
68	5,	2,								

31-24-2 (label for upper right hand corner of plot with the experimental data) CARD#69.

FF203 ON TE AT 1.50 MEV — Horizontal Label

COUNTS PER CHANNEL — Vertical Label

CARD #70

Labels for plot of calculated and experimental spectra superimposed.

Appendix B

MEASUREMENTS OF THE ABSOLUTE ENERGY LOSS IN Fe AND Al

B.1 Thickness Measurements

The aluminum samples were prepared on polished, thermally oxidized silicon substrates. A thin gold layer with an average coverage of less than 20 Å was deposited first. The aluminum was then deposited by vacuum evaporation from a tungsten filament. Part of the sample was masked by a thin tungsten wire during this evaporation to permit a measurement of the thickness by multiple beam interferometry. A second thin gold layer was then deposited onto the Al film. A second Al film, about 2000 Å thick, was deposited over a small portion of the sample that included the area masked by the tungsten wire in the first Al deposition.

The thickness of the aluminum film was determined by measuring the step height in the area masked by the tungsten wire in the first deposition. The second aluminum layer over this region allows the use of optical interferometry since this guarantees identical phase shifts in the reflection of the light from both levels of the step. The thickness of the films were measured by Tolansky interferometry using a 5350 Å Tl source and Nomarski interferometry using the sodium-D doublet. The errors were estimated at ±1% from the reproducibility of the thickness measurements. The areal density was calculated by assuming bulk density(2.70 gm/cm^3).

The iron samples were prepared on Corning 0211 glass substrates with gold markers similar to those described above. The iron was

deposited by vacuum evaporation from an iron source in an alundum crucible heated by radio frequency induction heating.

The thickness of the iron films were inferred from the total magnetic moment of the film. This was measured by a hysteresis loop tracer measurement(Humphrey, 1967), which had been calibrated by the optical interferometric methods described above. These values were confirmed by x-ray fluorescence yield measurements that had also been calibrated by optical measurements. The areal density was again calculated by assuming bulk density(7.86 gm/cm^3).

The only obvious source of systematic errors would be due to errors in the calculated areal densities produced by assuming that thin films are of bulk density. Any serious errors would most plausibly be the result of voids in the film. The apparent stopping power of a porous film could then be lower than the true value. However, we believe that the density of our films is probably very close to bulk density(K. N. Tu, 1972, private communication).

B. 2 Results and Discussion

Measurements were performed with the incoming beam at normal incidence and detected at a laboratory scattering angle of 168°. Incident particle energies of 0.5-2.25 MeV were used at current levels of 50-150 nA. The scattered particles were detected by a silicon surface barrier detector and analyzed using standard electronics.

The energy loss was determined from the energies of the two gold marker signals. The analytical procedure for determining the mean energy and the net energy loss was described by Moorhead(1965).

The results of the measurements performed on four Al samples of different thicknesses are shown in Figure B.1. Also included for comparison are the values reported by Porat and Ramavataram(1961), Chu and Powers(1969), and Harris and Nicolet(1974). In addition, the semi-empirical values of Ziegler and Chu(1973) are also shown. The present values are in good agreement with those of Porat and Ramavataram(1961). The largest departure from the values of Chu and Powers(1969) is the ~10% difference near 0.75 MeV. If the films were porous, as discussed above, the present values should be systematically low. Since the present values are not systematically too low, the films probably do not contain a large volume of voids.

The results of the measurements performed on three Fe samples of different thicknesses are shown in Figure B.2. Also included for comparison are the values of Chu and Powers(1969). Although there is a large amount of scatter in the present measurements, they are clearly systematically slightly lower than the values of Chu and Powers(1969). Since the measurement of the total magnetic moment or the x-ray fluorescence yield is a direct measurement of the areal density, the source of these discrepancies are not obvious unless all iron films are less dense than bulk iron.

The present measurements were motivated in part by the apparent discrepancies in the Al-Si and Al-Fe yield measurements(Table 3.3) when compared with the reported stopping cross sections. Since the Si stopping cross section had been recently measured by three groups with reasonable agreement(see the discussion in 3.5.3), it was felt that these discrepancies might originate in the Al stopping power values.

Figure B.1 Energy Loss of ^{4}He in Aluminum. The present values(•) are compared with those of Chu and Powers(1969)(X), Porat and Ramavataram(1961)(+) and Harris and Nicolet(1974)(◇). Also shown as a solid line are the semi-empirical values of Ziegler and Chu(1973).

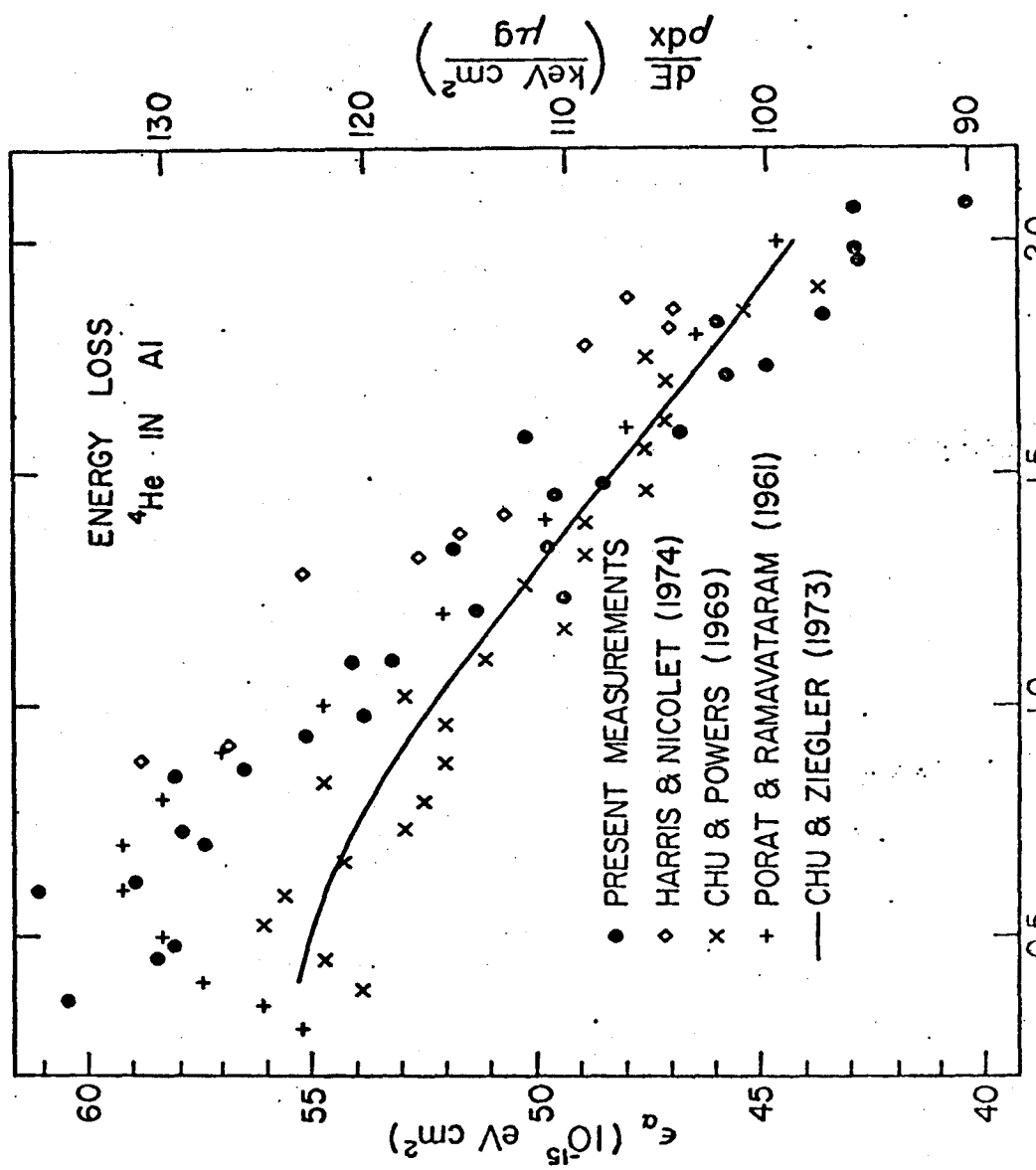
ENERGY LOSS
^{4}He IN Al
PRESENT MEASUREMENTS
HARRIS & NICOLET (1974)
CHU & POWERS (1969)
PORAT & RAMAVATARAM (1961)
CHU & ZIEGLER (1973)
ϵ_a (10^{-15} eV cm^2)
$\frac{dE}{\rho dx}$ $\left(\frac{keV\ cm^2}{\mu g}\right)$
ENERGY (MeV)
60
55
50
45
40
130
120
110
100
90
0.5
1.0
1.5
2.0

Figure B.1

Figure B.2 Energy Loss of ^{4}He in Iron. The present values(solid symbols) are compared with those of Chu and Powers (1969)(°).

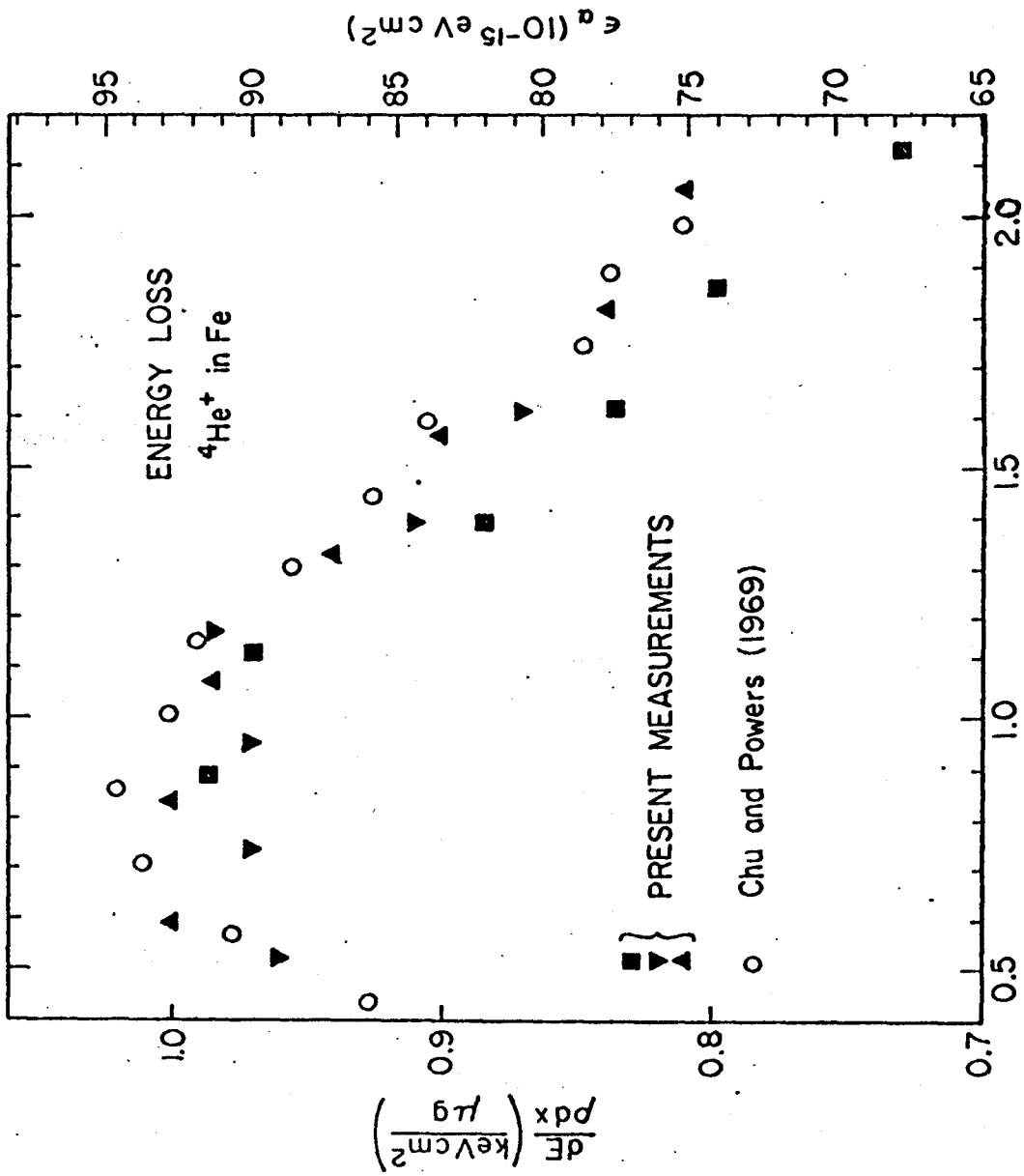
ENERGY LOSS
$^4He^+$ in Fe
PRESENT MEASUREMENTS
Chu and Powers (1969)
$\frac{dE}{\rho dx}\left(\frac{keV cm^2}{\mu g}\right)$
$\epsilon_a (10^{-15} eV cm^2)$
ENERGY (MeV)
0.7
0.8
0.9
1.0
0.5
1.0
1.5
2.0
95
90
85
80
75
70
65

Figure B.2

Using the present results for Al rather than those of Chu and Powers(1969) would reduce the calculated Al thick target yield by 3-5%. Similarly, the present values would increase the calculated Fe thick target yield by 2-10%. Together they would reduce the discrepancy in the Fe-Al yield ratio shown in Table 3.3. However, it would not significantly affect the Al-Si yield ratio discrepancy and it would introduce a statistically significant Fe-Si yield ratio discrepancy. Unless all of the reported Si stopping cross sections are systematically too high, it is difficult to reconcile the present results with the observed Al-Si yield ratio.

REFERENCES

Appendix B

W. K. Chu and D. Powers, 1969, Phys. Rev., vol. 187, p.478.

J. M. Harris and M-A. Nicolet, 1974, unpublished.

F. B. Humphrey, 1967, J. Appl. Phys., vol. 38, p. 1520.

R. Dale Moorhead, 1965, J. Appl. Phys., vol. 36, p. 391.

D. I. Porat and K. Ramavataram, 1961, Proc. Phys. Soc.(London), vol. 78, p. 1135.

K. N. Tu, 1972, private communication.

J. F. Ziegler and W. K. Chu, 1973, IBM Res. Rept. RC4288(#19193).

PART II

MAGNETITE THIN FILMS:

FABRICATION AND ELECTRICAL PROPERTIES

Chapter I

INTRODUCTION

Once upon a time, in far away Thessaly, an unknown shepherd found his sandals clinging to the side of a rock. Because this part of Greece was known as Magnesia, this lodestone was called magnetite and it was said to have magnetic properties. Since that time over 2500 years ago, studies of the behavior of this material have been instrumental in understanding the phenomena associated with ferromagnetism.

Magnetite has been a preferred material for these investigations because of its availability in natural single crystals. At room temperature, these crystals have cubic, inverse spinel structure in which the unit cell contains thirty-two oxygen atoms and twenty-four metal atoms. Eight of these metal atoms are bivalent while the remaining sixteen are trivalent. Eight of these cation sites are each surrounded by a tetrahedron of oxygen atoms while the other sixteen are each in the midst of an oxygen octahedron. In spinel($MgAl_2O_4$), the tetrahedral sites are occupied by the eight divalent Mg^{2+} ions and the octahedral sites are occupied by the sixteen trivalent Al^{3+} ions. In Verwey and Heilmann's (1947) inverse spinel structure for magnetite, shown in Figure I.1, the eight tetrahedral sites are occupied by trivalent Fe^{3+}. The remaining eight trivalent Fe^{3+} ions and the eight divalent Fe^{2+} ions are randomly distributed over the sixteen available octahedral sites.

The electrical properties have been particularly illuminating because they led directly to this model for the structure. At room temperature, magnetite has the lowest resistivity of all the ferrites,

Figure I.1 Four views of the spinel structure:

(a) the stacking pattern of the A and B sub-cells in a unit cell;

(b) the unit cell, with the oxygen atoms shown as open circles, the octahedral cations shown as solid circles, and the tetrahedral sites shown as circled dots;

(c) a view showing the fcc ordering of the oxygen atoms(white spheres) and the tetrahedral symmetry of these around the solid black atoms(right side of figure) and the octahedral symmetry of the oxygen around the shaded atom on the left half(the black spheres in (b) and (c) do not correspond);

(d) a view of the repeating A and B sections of the unit cell that stack according to (a).

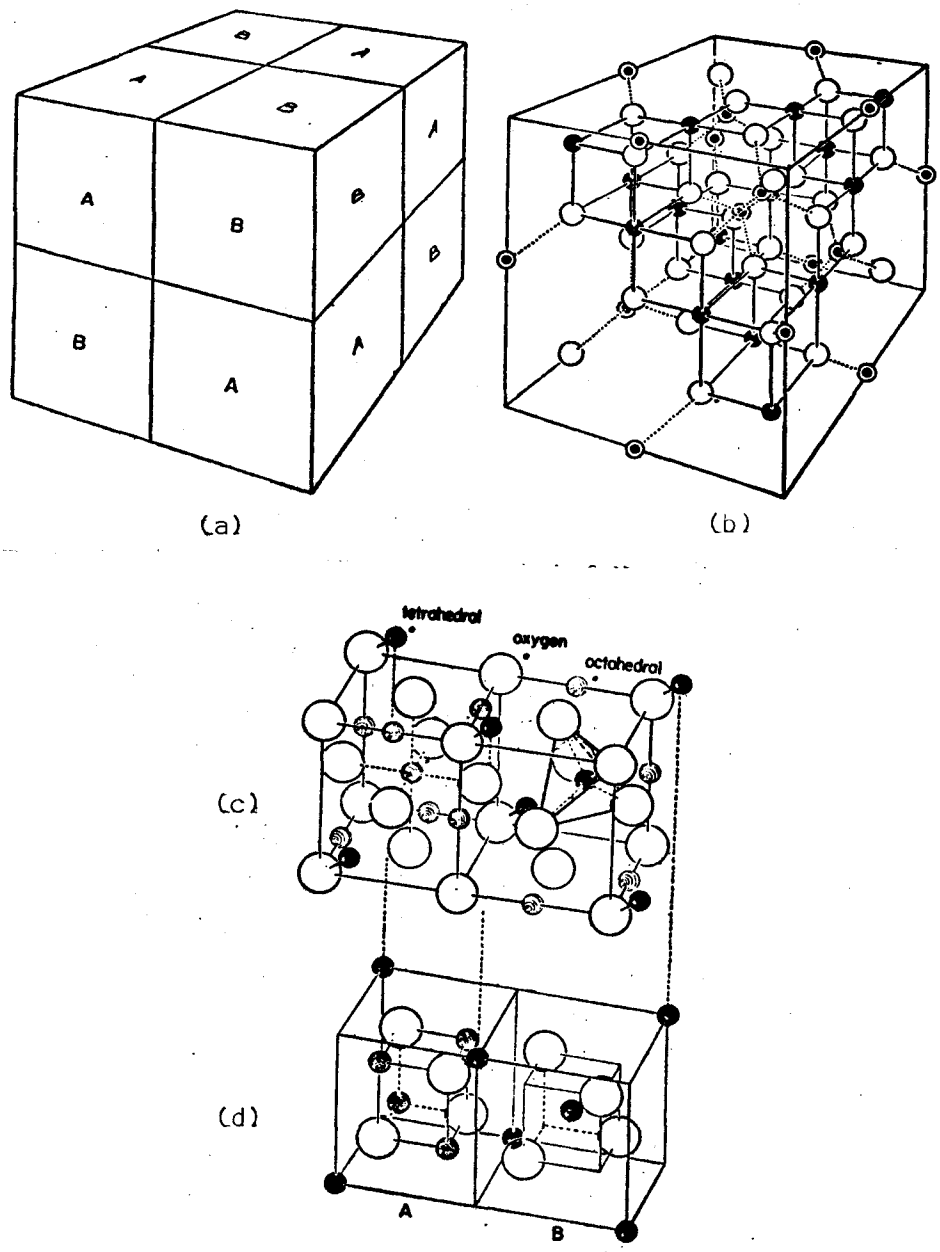

Figure 1.1

From Miles et al(1957) and used with the permission of A. von Hippel.

about 10^{-2} Ωcm(Smit and Wijn, 1959). Above room temperature, the resistivity has the positive temperature coefficient that is characteristic of metallic conductivity. Below room temperature, it behaves as a semiconductor with a negative temperature coefficient. Magnetite was the first oxide in which a conductivity transition was observed(Weiss, 1896). The conductivity in stoichiometric, bulk magnetite changes abruptly by two orders of magnitude at 119°K(Calhoun, 1954). This was eventually correlated with changes in the crystalline magnetic anisotropies(Li, 1932) and a specific heat anomaly(Millar, 1929). On this basis, Verwey et al proposed that the conductivity in the high temperature form of magnetite was due to dynamic disorder of the divalent and trivalent ions on the octahedral sites. They further proposed that the phase transition was also accompanied by an orthorhombic distortion of the cubic lattice which would destroy the equivalence of the octahedral sites to produce an ordering of the divalent and trivalent ions. The lattice distortion was later verified by strain gauge dilatometry(Bickford,1953) and by high resolution x-ray diffractometry(Abrahams and Calhoun, 1953). The electronic disorder-order transformation has been observed by neutron diffractometry(Hamilton, 1958), Mössbauer spectroscopy(Romanov et al, 1969) and nuclear magnetic resonance(Westrum and Grønvold, 1969). The details in the results of some of the more recent experiments using these techniques have suggested that the Verwey model may not be correct in all of its details. However, they are also unable to confirm enough of the predictions of any of the competing models to displace the Verwey model(a discussion of some alternative models is in Verble, 1974).

This model of the electronic ordering led directly to the con-

cept of ferrimagnetic ordering(Néel, 1948). The saturation magnetization of Fe_3O_4 corresponds to four Bohr magnetons per molecule, while ferromagnetically ordered Fe_3O_4 would be expected to have fourteen Bohr magnetons, with four from each of the divalent ions and five from each of the trivalent ions. The low magnetization was explained on the basis of anti-ferromagnetic coupling between the octahedral and tetrahedral sublattices, producing a net cancellation of the contributions from the trivalent ions.

Ferrites, of course, are a class of materials that are of great technological importance. In addition to their obvious uses as non-volatile memory medium, ferrites are also used for permanent magnets, high-permeability cores for transformers and inductors, and microwave devices. Its utility is enhanced by its chemical stability and its mechanical hardness, while its potentially high coercivity makes it attractive as a permanent storage medium. Since all ferrites and garnets can be derived from magnetite by metal ion substitution, magnetite is the prototypical ferrimagnetic compound and an understanding of its properties facilitates the understanding of the other ferrites.

Thin film geometries for magnetic materials are advantageous for both investigative and technological reasons. The macroscopic shape-induced anisotropies allow several simplifying assumptions in which the errors in the approximation are of the order of the film thickness divided by one of the macroscopic dimensions(Soohoo, 1965). In magnetic recording applications, these anisotropies dictate that very thin layers are required to achieve a high information density.

The present investigations were initiated by the recognition that there exists a simple manufacturing process for producing thin films of magnetite. A simple modification of this process will also produce several other ferrites over a modest composition range. The initial phase of this work was to unambiguously identify the material formed by this process as magnetite. Investigations into the galvanomagnetic properties were performed as a matter of opportunity since the technology for these measurements in thin layers already existed as part of an ion implantation program. The final phase of this work was to characterize certain anomalies in the Verwey transition behavior of these films that are observable only in thin film samples. These have been written for publication as:

"Magnetite Thin Films," J. S.-Y. Feng, C. H. Bajorek and M-A. Nicolet, IEEE Transactions on Magnetics, Volume MAG-8, p. 277(1972).

"Magnetoelectric Properties of Magnetite Thin Films," J. S.-Y. Feng, R. D. Pashley and M-A. Nicolet, to be published in the Journal of Physics C.

"Substrate Effects on Magnetite Thin Films," J. S.-Y. Feng and M-A. Nicolet, submitted to the Journal of the Physics and Chemistry of Solids.

The last work was also presented at the International Magnetics Conference(INTERMAG) on May 14-17, 1974 in Toronto, Ontario, Canada. In addition, there is currently pending a patent application describing the process for producing the magnetite films; this application embodies

the substantive new discoveries described in the first of the above publications.

REFERENCES

Chapter I

S. C. Abrahams and B. A. Calhoun, 1953, Acta Cryst., vol. 6, p. 105.

L. R. Bickford, Jr., 1953, Rev. Mod. Phys., vol. 25, p. 75.

B. A. Calhoun, 1954, Phys. Rev., vol. 94, p. 1577.

W. C. Hamilton, 1958, Phys. Rev., vol. 110, p. 1050.

C. H. Li, 1932, Phys. Rev., vol. 40, p. 1002.

P. A. Miles, W. B. Westphal and A. von Hippel, 1957, Rev. Mod. Phys., vol. 29, p. 279.

R. W. Millar, 1929, J. Am. Chem. Soc., vol. 51, p. 115.

L. Néel, 1948, Ann. Phys. [12], vol. 3, p. 137.

V. P. Romanov, V. D. Checherskii and V. V. Ermenko, 1969, phys. stat. sol., vol. 31, p. K 153.

J. Smit and H. P. J. Wijn, 1959, Ferrites(Wiley), p. 229.

R. F. Soohoo, 1965, Magnetic Thin Films(Harper and Row), p. 56.

J. Larry Verble, 1974, Phys. Rev. B, vol. 9, p. 5236.

E. J. W. Verwey and P. W. Haayman, 1941, Physica(Utrecht), vol. 8, p. 979.

E. J. W. Verwey, P. W. Haayman and F. C. Romeijn, 1947, J. Chem. Phys., vol. 15, p. 181.

E. J. W. Verwey and E. L. Heilmann, 1947, J. Chem. Phys., vol. 15, p. 174.

P. Weiss, 1896, thesis, Paris(unpublished).

E. F. Westrum and F. Grønvold, 1969, J. Chem. Thermo., vol. 1, p. 543.

Chapter 2

MAKING THE FILMS

2.1 Introduction

From the phase diagram of the iron-oxygen system, shown in figure 2.0, there are three possible iron oxide compositions. However, below 560°C, anti-ferromagnetic wüstite(FeO) is not stable and the only equilibrium compositions are Fe_3O_4 and Fe_2O_3(Hansen and Anderko, 1958). The only known allotropic form of Fe_3O_4 is ferrimagnetic magnetite, while some of the more common forms of Fe_2O_3 include anti-ferromagnetic hematite(α-Fe_2O_3), ferrimagnetic maghemite(γ-Fe_2O_3), and ferrimagnetic δ-Fe_2O_3.

The high temperature oxidation of bulk iron produces successive layers of α-Fe_2O_3, Fe_3O_4 and FeO on the pure iron. This is interpreted as evidence that α-Fe_2O_3 is permeable to oxygen, while iron passes through FeO, and both elements are mobile in Fe_3O_4(Hauffe, 1965). Because of the different relative rates for the competing processes, only α-Fe_2O_3 is produced in significant quantities at low temperatures ($\lesssim$ 400°C), although some Fe_3O_4 is almost certainly also produced after long oxidations at moderate oxidation temperatures(Vernon et al, 1953; Caule and Cohen, 1955). As a result, a completely oxidized iron film consists entirely of α-Fe_2O_3.

Since there are only two stable oxides below 560°C, in the presence of excess iron the more iron-rich of the oxides should be the stable phase. This suggests that hematite can be converted to magnetite by providing additional iron in an oxygen-free ambient. In common with

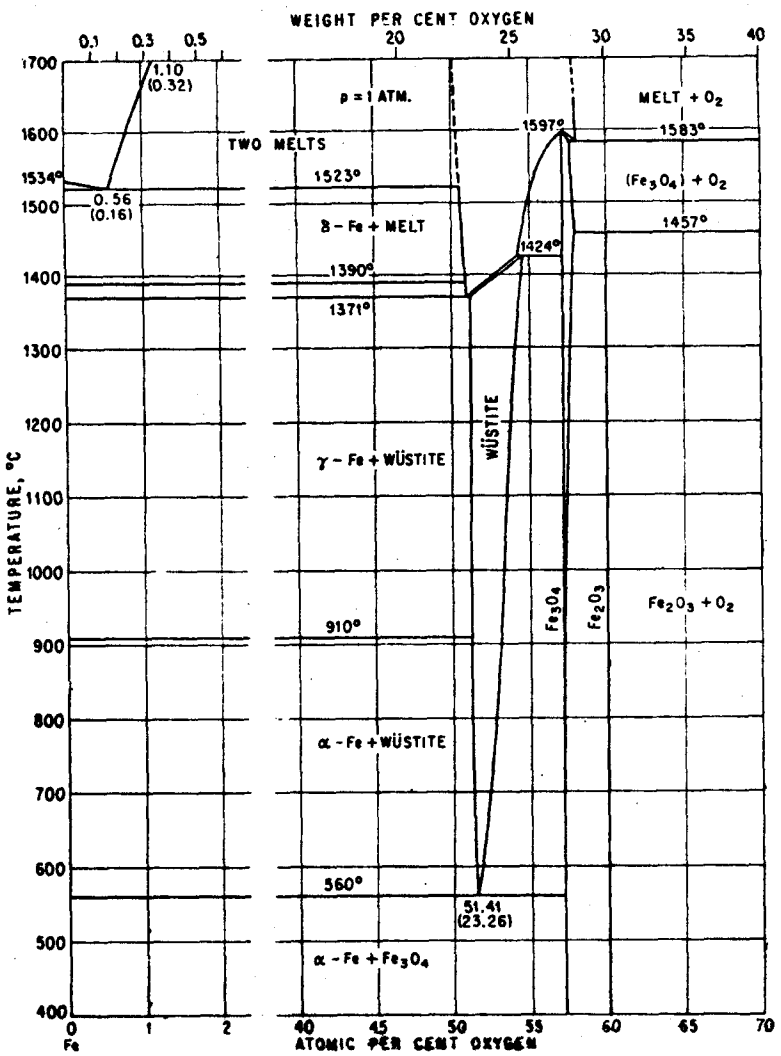

Figure 2.0 The iron-oxygen phase diagram. This shows the allowed compositions of iron oxide at various temperatures. Note that only Fe_3O_4 and Fe_2O_3 are stable below 560°C. "From The Constitution of Binary Alloys, Second Edition, by M. Hansen and K. Anderko. Copyright 1958 by the McGraw-Hill Book Company. Used with permission of McGraw-Hill Book Company."

other thin film systems, it was expected that this reaction would take place at relatively low temperatures and that the transformation would occur rapidly. This concept was successfully applied to produce magnetite thin films in the sub-micron range.

2.2 The Manufacturing Process

After acquiring a suitable substrate, the first step is to deposit a thin film of pure iron. Any control on the thickness of the final product must be exercised at this point since, assuming bulk properties, the magnetite film eventually produced by this process will be about 2.34 times as thick as this iron film. A typical method would be by evaporation in a vacuum of better than 10^{-6} Torr with the deposition rate monitored by a quartz crystal resonator. It is recommended that any photolithography be performed at this step since this not only gives better lateral definition than etching the last pure metal film, but also because pure iron is more easily etched than any of the iron oxides.

The pure iron film is then oxidized at 450-550°C in air or O_2 at 1 atm until a clear red oxide film is formed. The time required for this step depends on the oxidation temperature and the thickness of the iron film. Although this film has not been extensively characterized, it is believed to be anti-ferromagnetic hematite. Some of the circumstantial evidence include series resistance measurements, which indicate a bulk resistivity of over 10^6 Ωcm; α-Fe_2O_3 is the only insulator among the commonly occuring iron oxides. Measurements on a 1 kOe peak field hysteresis loop tracer show no evidence of a detectable magnetic

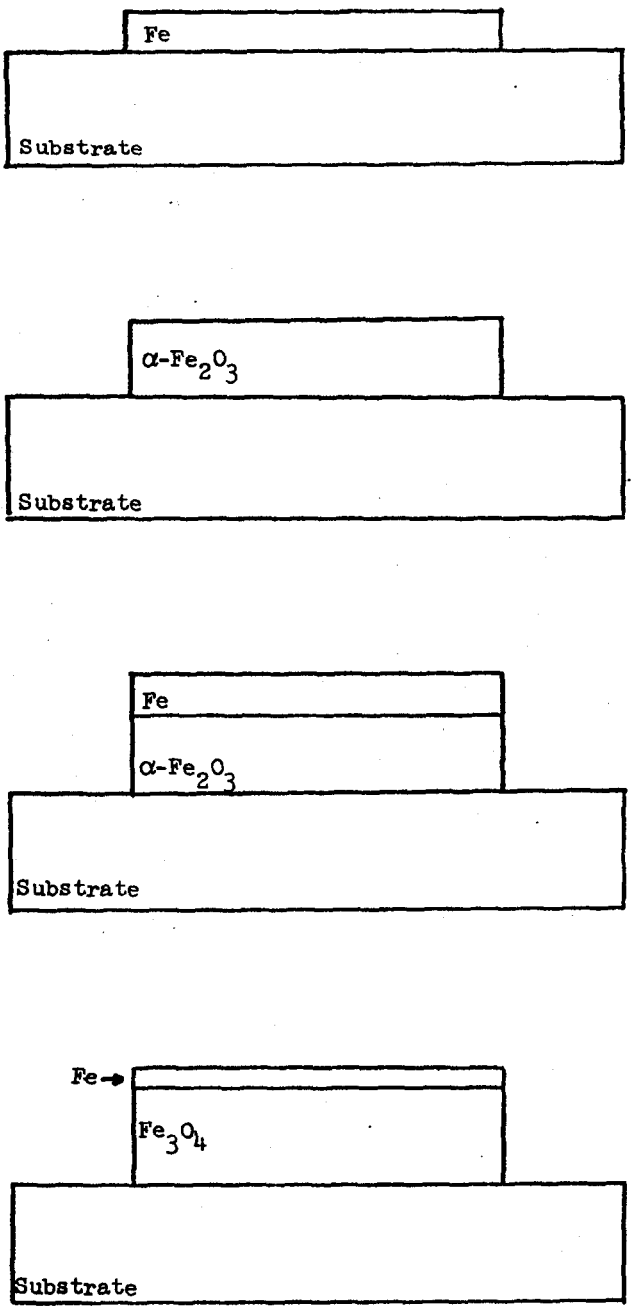

1. Deposit pure Fe onto chemically inert substrate

2. Photolithography (optional)

3. Oxidize Fe film in air or O_2 at 400-600°C to produce α-Fe_2O_3 (anti-ferro-magnetic)

4. Deposit pure Fe* on α-Fe_2O_3 film

   * Other metals M can be used to make other ferrites $M_{0.33}Fe_{2.67}O_4$

5. Anneal in an inert ambient, e.g., vacuum, at 400-500°C to convert α-Fe_2O_3 to Fe_3O_4

6. Remove excess pure Fe

Figure 2.1 Illustrating the manufacturing process for making thin films of magnetite(see section 2.2)

moment, as expected for an anti-ferromagnet. No attempts were made to observe either the Morin transition or anti-ferromagnetic resonance in these films. However, since hematite is the only stable iron oxide in an oxygen-rich ambient, it is reasonable to assume that the available evidence is sufficient to identify this film as α-Fe_2O_3. Furthermore, a comparison of the composition with a film that is believed to be magnetite makes this conclusion inescapable. Further discussion of the nature of this film is beyond the scope of this work.

The hematite film is then provided with the excess iron needed to form magnetite. The amount required is only about 12% of the amount deposited in the original iron film, but this second film is usually made to be over 50% as thick as the first iron film. Not only does this guarantee that there is sufficient iron to complete the conversion, but the surplus iron also protects the oxide layer from possible undesired reactions with the annealing ambient.

At this point, the process can be modified to produce other ferrites. For example, the ferrite film could be doped with nickel by using a permalloy(Fe-Ni) film of a selected composition. Using a pure nickel film, for example, would result in a ferrite film with a composition of $Ni_{0.33}Fe_{2.67}O_4$.

The conversion to magnetite is then completed by annealing this two-layered structure. These have normally been performed at 350-450°C in a vacuum of better than 10^{-7} Torr because it was available. In principle, it could also be performed in any other inert ambient such as dry argon or nitrogen. The time required for the completion of the conversion is not known, but the process has provided 100% yield for

anneals longer than eight hours. The lateral extent of the converted material after this anneal, as observed by optically inspecting the misaligned regions after the second iron deposition, is 5-10 μm. However, it is not known whether the conversion rate is diffusion limited or reaction rate limited.

The surplus iron remaining after the conversion can be removed in either dilute HNO_3 or a solution of one part volumetric bromine in five parts methyl acetate. The nitric acid is the recommended solution.

This process has been used successfully to produce magnetite films 200-8000 Å thick on a large variety of substrates. These have included fused quartz, thermally oxidized silicon, AT-cut quartz, silicon, alumina, sapphire, spinel, magnesium oxide, gadolinium gallium garnet, pyrex, Corning 0211 glass, Corning 7059 glass and ordinary window glass. Films thicker than 8000 Å tend to develop large internal stresses that eventually exceed the yield strength of the film-substrate bond, eventually resulting in separation of the film from the substrate. Optical microscopy with 300X magnification showed no evidence of pinholes, although there were sometimes scratches that represent evidence of careless handling. Transmission electron microscopy of a carbon replica and scanning electron microscopy both showed evidence of about 700 Å surface roughness on samples 2000-3000 Å thick. An electron micrograph of a carbon replica is shown in the reprint in Chapter 3.

In theory, one additional step can be included in this process to produce γ-Fe_2O_3. A well-known step in the manufacture of γ-Fe_2O_3 for magnetic recording tape involves oxidizing powdered Fe_3O_4 in moist oxygen at 300-350°C(Bate and Alstad, 1969). There is every reason to

believe that this should be just as successful when applied to making maghemite thin films from magnetite thin films.

2.3 Evidence for Magnetite Formation

The change in the composition produced by the conversion step was first verified by Rutherford backscattering spectrometry. Figure 2.2 shows a comparison of the iron signals from an iron-on-hematite sample and an iron-on-magnetite sample. Although these spectra were not taken on the same sample, the two samples were prepared simultaneously to be identical in every way except for the execution of the final annealing step to convert the hematite to magnetite. The iron was left on to guarantee a valid comparison between the two oxide signals because the reproducibility of the ion dose is not always sufficiently precise. Note that the match between the two iron signals is very good. The data clearly show that after the conversion step, the amount of iron in the oxide has increased at the expense of the pure iron film. The ratio of the two signals as evaluated under the dashed areas is almost exactly equal to the value predicted by Bragg's rule. Of course, since there are only two iron oxides at any of the processing temperatures, the inescapable conclusion is that the chemical formulas for these oxides are Fe_2O_3 and Fe_3O_4.

(Speaking of Bragg's rule, the method used to take the ratios was selected because it is relatively insensitive to errors in the absolute stopping cross sections used in the calculations. Since the change in the iron-to-oxygen ratio is about 12%, and since the iron contributes only about one-half of the total stopping, there is only

Figure 2.2 Top: The iron signals of 2.0 MeV $^{4}He^{+}$ ions backscattered from hematite films covered with iron on sapphire substrates before(○) and after(●) conversion to magnetite.

Bottom: Decomposition of the spectra into step signals. The pure iron on the surface generates the higher step shown at higher energies. The lower step is due to the iron in the underlying oxide film.

The results show that after conversion, the pure iron film is thinner while the iron content of the oxide film has increased correspondingly.

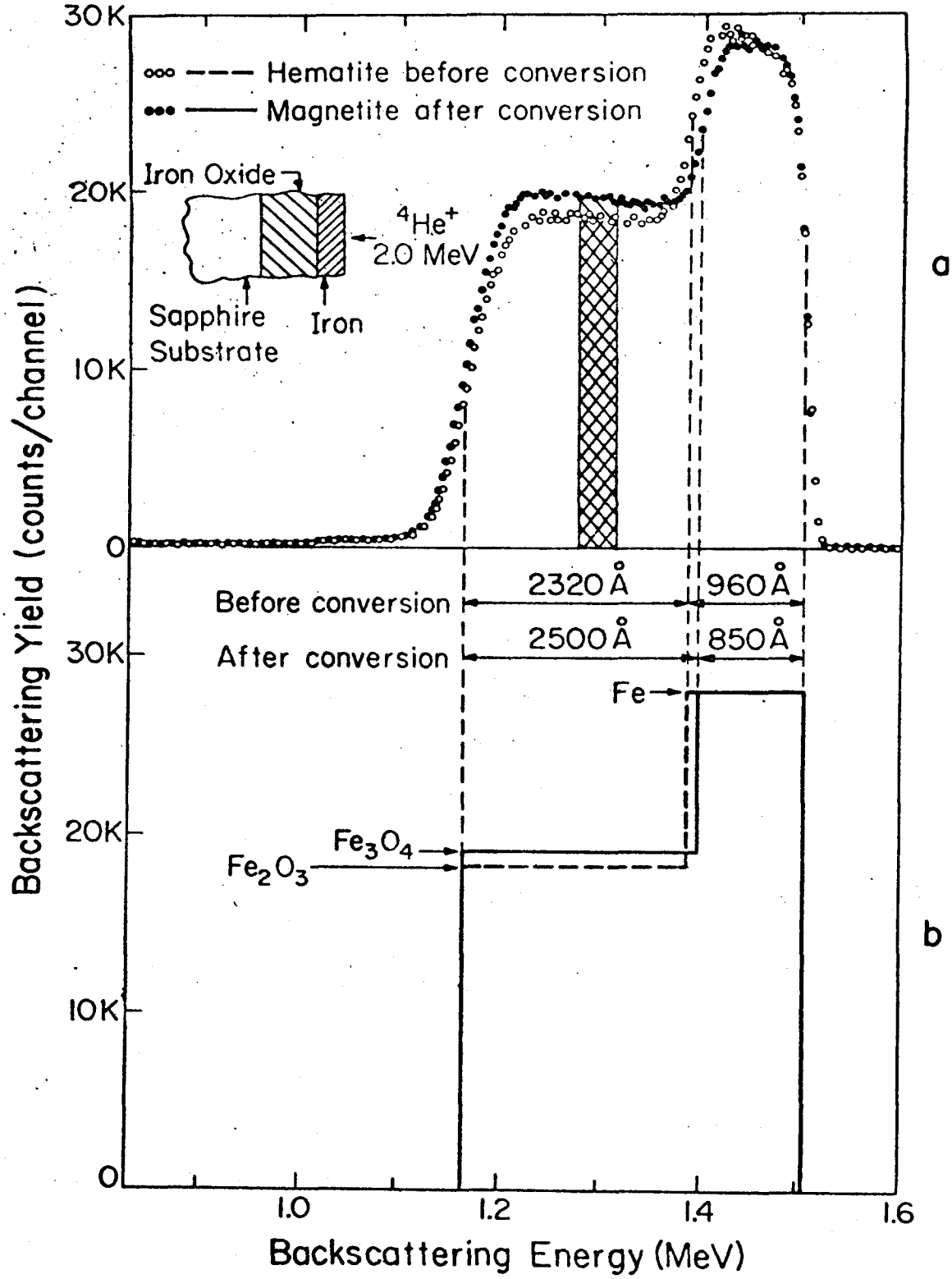
Hematite before conversion
Magnetite after conversion
Iron Oxide
$^4He^+$
2.0 MeV
Sapphire Substrate
Iron
a
b
Before conversion
2320 Å
960 Å
After conversion
2500 Å
850 Å
Fe
Fe_3O_4
Fe_2O_3
Backscattering Yield (counts/channel)
Backscattering Energy (MeV)
30K
20K
10K
0
1.0
1.2
1.4
1.6

Figure 2.2

about a 6% sensitivity to errors in the relative stopping powers. Also, we take this opportunity to point out the excellent reporducibility in the energy widths of the iron signals before and after the conversion step(see Part I, Chapter 2).)

More convincing evidence that the converted iron oxide is indeed magnetite can be found in figure 2.3. X-ray powder diffractometry using Cu-K_α radiation was used to verify that the structure of a converted 2400 Å film on Corning 0211 glass is identical to bulk magnetite. The gaps in the background signal are the angles over which no measurements were performed. The principal powder diffraction lines for several iron oxides are shown below the diffractometer data, with the heights indicating the approximate relative amplitudes. The observed lines are consistent with a polycrystalline film with cubic spinel structure. The measured lattice parameter is 8.391±0.003 Å while the value for bulk magnetite is 8.394±0.004 Å. The correlation of the observed lines to those of magnetite excludes the possibility of significant amounts of wüstite(FeO) or most forms of Fe_2O_3. Although the structure and lattice parameter(8.34 Å) of maghemite(γ-Fe_2O_3) are very close to those of magnetite, this phase is obviously eliminated by the increased iron content evident in the backscattering data. The peak identified with the (311) planes is detailed in the inset. The narrow half-width indicates that the grains are relatively free of strains and defects. Muret(1974) reports that in 2000-6000 Å films, these grains are 200-1000 Å.

Measurements of some of the magnetic properties were performed on a 60 Hz 1 kOe peak field hysteresis loop tracer, a 20 kOe force balance magnetometer, and a 1-8 GHz perpendicular ferromagnetic reso-

Figure 2.3 X-ray powder diffraction pattern from a converted 2400 Å film on a Corning 0211 glass substrate using Cu-K_α radiation. A comparison with the principal powder diffraction lines of various oxides, shown below the data, shows that the structure is identical to Fe_3O_4. The detail of the (311) peak shown in the inset shows that the grains are relatively large and unstrained.

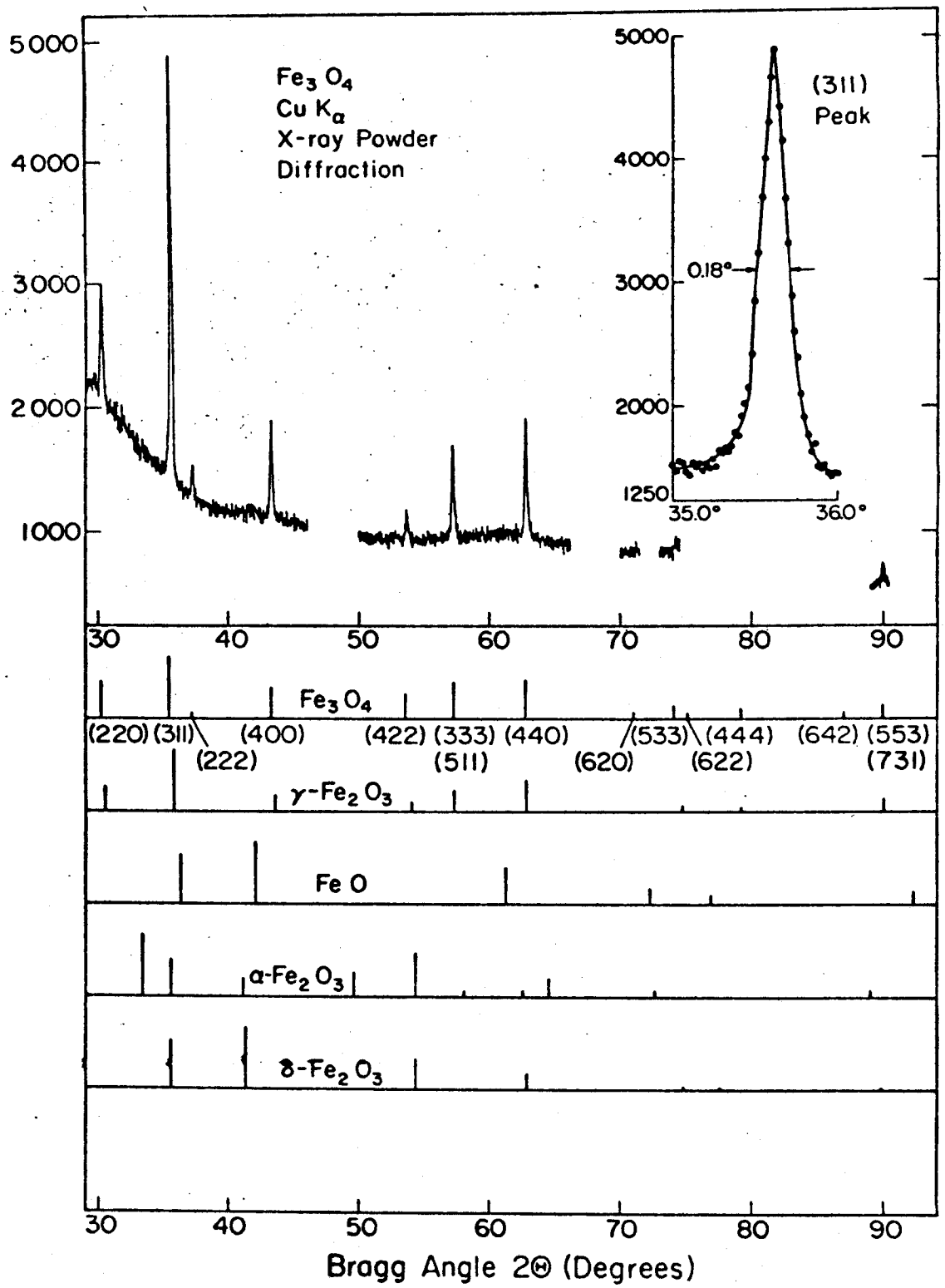
5000
4000
3000
2000
1000
Fe3 O4
Cu Kα
X-ray Powder
Diffraction
(311)
Peak
0.18°
1250
35.0°
36.0°
30
40
50
60
70
80
90
Fe3 O4
(220) (311) (400) (422) (333) (440) (533) (444) (642) (553)
(222) (511) (620) (622) (731)
γ-Fe2 O3
Fe O
α-Fe2 O3
δ-Fe2 O3
Bragg Angle 2Θ (Degrees)

Figure 2.3

nance(FMR) spectrometer. The coercivity and remanence of 2000-3000 Å films range from 150-400 Oe and 40-60%, respectively, and there appears to be some correlation of these properties with the choice of the substrate. The films showed no measurable planar uniaxial anisotropy. The saturation magnetization of these films as determined by force balance magnetometry is $4\pi M_S$ = 5.2±0.2 kG, while the value for bulk magnetite is 6.0 kG(Kittel, 1966). The value of $4\pi M_S - H_{k\perp}$ as measured by FMR is 5.0±0.2 kG, suggesting that there are no significant and measurable perpendicular anisotropies. The gyromagnetic ratio as determined from FMR is $\gamma/2\pi$ = 1.95±0.10 MHz/Oe, corresponding to $g \approx 3$. All FMR linewidths were less than 100 Oe, much sharper than any values reported for bulk magnetite(Banks et al, 1961; Bickford, 1950).

Since the electrical properties will be discussed at greater length in the next two chapters, only the most cursory summary of the early measurements will be given here. The room temperature resistivity is 8.5 mΩcm, compared to reported values of 4-7 mΩcm for bulk magnetite (Smit and Wijn, 1959; Calhoun, 1954). The temperature dependence of the resistivity does exhibit a conductivity transition, but it is not identical in detail to the Verwey transition observed in bulk magnetite.

The most obvious evidence that this process results in the conversion of hematite to magnetite is the color change in the films. The hematite films are clear and red. The conversion step changes the color to a nearly opaque black-brown. These colors are, of course, consistent with those of bulk hematite and bulk magnetite.

REFERENCES

Chapter 2

E. Banks, N. H. Riederman, H. W. Schleuning and L. M. Silber, 1961, J. Appl. Phys., vol. 32, p. 44S.

G. Bate and J. K. Alstad, 1969, IEEE Transactions on Magnetics, vol. MAG-5, p. 821.

L. R. Bickford, Jr., 1950, Phys. Rev., vol. 78, p. 449.

B. A. Calhoun, 1954, Phys. Rev., vol. 94, p. 1577.

E. J. Caule and M. Cohen, 1955, Can. J. Chem., vol. 3, p. 298.

M. Hansen and K. Anderko, 1958, Constitution of Binary Alloys(McGraw-Hill), second edition, p. 686.

K. Hauffe, 1965, Oxidation of Metals(Plenum Press), p. 273.

C. Kittel, 1966, Introduction to Solid State Physics(Wiley and Sons), third edition, p. 461(also second edition, p. 407 and fourth edition, p. 536).

P. Muret, 1974, Sol. St. Comm., vol. 14, p. 1119.

J. Smit and H. P. J. Wijn, 1959, Ferrites(Wiley and Sons), p. 229.

W. H. J. Vernon, E. A. Calnon, C. J. B. Clews, and T. J. Nurse, 1953, Proc. Roy. Soc. A, vol. 216, p. 375.

Chapter 3

GALVANOMAGNETIC PROPERTIES

3.1 Introduction

Despite the importance of the transport properties and their impact on the understanding of the phenomena observed in magnetite, there have been few comprehensive studies of the galvanomagnetic properties of Fe_3O_4. While this work does not constitute that definitive study, it is the most extensive set of measurements ever reported in presumably stoichiometric samples. Most experiments have been limited to only one or two of these galvanomagnetic properties.

There have not been very many reports of the Hall effect in bulk magnetite. As with all other ferromagnetic materials, magnetite exhibits both the ordinary and extraordinary Hall effects. Although the measurements of the ordinary Hall coefficient have been published by Siemons(1970), Lavine(1959), and Kostopoulos and Theodossiou(1970), Siemons is the only one who reports any numerical values for the ordinary Hall coefficient over a range of temperatures. The extraordinary Hall effect has also been observed by Lavine(1961) and Kostopoulos and Theodossiou(1970). Lavine(1961) is the only one who reports any numerical values; Kostopoulos and Theodossiou reported some anomalous sign changes in the extraordinary Hall coefficient below the Verwey transition temperature.

Reports of the magnetoresistance have been even more scarce than the Hall effect measurements. Domenicali(1950) gives only very rough approximate values of the magnetoresistance at room temperature

and at 77°K. Zalesskii(1961) reported crystalline anisotropies in the room temperature field dependence of the magnetoresistance. The electric and magnetic field dependence at 77°K was measured in a synthetic single crystal by Balberg(1970) in an attempt to explain some switching phenomena that had been observed in magnetite(these were eventually attributed to Joule heating to induce transitions to the cubic phase in some high conductivity filaments in the magnetite samples). Some of the most extensive measurements were performed by Kostopoulos(1972) up to 10 kOe from 77°K to room temperature.

A hidden and heretofore unmentioned pitfall that may ensnare the unwary experimenter is the effects of the presence of a small amount of impurities in the sample. This may have been the reason why there have been so few reports of extensive investigations into the electrical transport properties of magnetite. It is known, for example, that the effects of these impurities vary depending on whether the impurities are on tetrahedral or octahedral sites. The anomalies in the field dependence of the extraordinary Hall effect observed by Kostopoulos and Theodossiou(1970) and the anisotropies in the magnetoresistance reported by Zalesskii(1961) can be attributed to the impurities in their natural magnetite samples, which could have exceeded 2% in some cases.

The present measurements were undertaken, in part, because we believed that the process described in the previous chapter resulted in stoichiometric magnetite. With the advice of several persons more knowledgeable in the properties of magnetic thin films, we also almost immediately recognized the advantages of the thin film configuration for these galvanomagnetic measurements. Some of the less obvious

problems created by this geometry will be discussed in the next chapter.

3.2 Results

The results of the galvanomagnetic measurements are presented in the enclosed preprint. This is the manuscript of a paper to be published in the Journal of Physics C, and it has been accepted for publication in that journal.

MAGNETOELECTRIC PROPERTIES OF MAGNETITE THIN FILMS*

by

J. S.-Y. Feng, R. D. Pashley†, and M-A. Nicolet
California Institute of Technology
Pasadena, California 91109

ABSTRACT

Resistivity, dc Hall effect and transverse magnetoresistance measurements were made on polycrystalline thin films of magnetite (Fe_3O_4) from 104°K to room temperature. The Verwey transition is observed at T_V = 123°K, about 4°K higher than reported for bulk magnetite. The ordinary and extraordinary Hall coefficients are negative over the entire temperature range, consistent with negatively charged carriers. The extraordinary Hall coefficient exhibits a $\rho^{1/3}$ dependence on the resistivity above T_V and a $\rho^{2/3}$ dependence below T_V. The magnetoresistance is negative at all temperatures and for all magnetic field strengths. The planar Hall effect signal was below the sensitivity of the present experiment.

---

*Supported in parts by the Office of Naval Research (L. Cooper) and the Hoegsted Phim Memorial Fund.

†Present Address: Intel Corporation, Santa Clara, California

I. INTRODUCTION

Since the discovery of the first lodestone in ancient Greece, magnetite has been an important magnetic material. Because all ferrites and garnets can be derived from magnetite by metal ion substitution, it is the prototypical ferrimagnetic compound. The electrical properties have been particularly illuminating since they led to the initial understanding of the ordering and exchange mechanisms in ferrites (Verwey et al., 1947) and because magnetite was one of the first examples of an oxide in which a conductivity transition was observed (Weiss, 1896).

Associated with the conductivity transition is a structural transformation (Bickford, 1953), a specific heat anomaly (Miller, 1929), and a change in the crystalline magnetic anisotropy (Li, 1932). The conductivity above the transition temperature is a low mobility, high carrier density process and is believed to be due to localized electron states hopping to vacant sites (Heikes et al., 1959).

Previous measurements of the electrical properties have been performed on crystalline or ceramic samples (Bickford, 1953; Lavine, 1959, 1961; Kostopoulos and Theodossiou, 1970; Kostopoulos, 1972; Siemons, 1970; Drabble et al., 1971; Calhoun, 1954 and Domenicali, 1950). The conductivity has been measured from below 4°K to above the Curie temperature of 858°K. The extraordinary Hall effect has been measured on bulk samples from 77°K to over 200°K (Lavine, 1961; Kostopoulos and Theodossiou, 1970). The ordinary Hall coefficient has been reported by three experimenters with conflicting results. Siemons (1970) reported a positive Hall coefficient, implying hole conductivity. On the other hand, Lavine (1959) and Kostopoulos and Theodossiou (1970) both report negative Hall coefficients

for other ferrites. Further evidence of electron conduction is given by the negative Seebeck coefficients reported by Lavine (1959) and Constantin and Rosenberg (1972).

We present the results of resistivity, dc Hall effect and magnetoresistance measurements on polycrystalline thin film samples of magnetite. The advantages and disadvantages of performing measurements on thin films are discussed. Some of the differences from bulk are known to be due to the mechanical interaction between the sample film and the substrate.

2. GENERAL CONSIDERATIONS

2.1 Extraordinary Hall Effect

The Hall voltage V_H in a ferromagnetic material depends separately on the magnetization and the external field. The Hall voltage has been found to follow

$$V_H = (R_o H_\perp + R_1 M_\perp) \cdot I/t$$

where t is the sample dimension parallel to the applied magnetic field, I is the current, $H_\perp$ is the component of the magnetic field perpendicular to the current and $M_\perp$ is the component of the magnetization perpendicular to the current. Note that V_H depends only on the perpendicular components of $\vec{H}$ and $\vec{M}$. R_o is the ordinary Hall coefficient and R_1 is the extraordinary Hall coefficient. Experimentally, R_1 has been observed to be one to two orders of magnitude larger than R_o (Pugh and Rostoker, 1953).

Calculations have predicted that the extraordinary Hall coefficient should have a power law dependence on the resistivity

$$R_1 \propto \rho^n$$

When the conductivity is due to non-localized d-band electrons, as in ferromagnetic metals, R_1 is proportional to ρ^2 (Karplus and Luttinger, 1954). Measurements on ferromagnetic metals have shown that the actual dependence is very close to the predicted square law (Berger, 1972).

2.2 Magnetoresistance

Semiclassical models predict that the apparent resistivity of a conductor should increase in the presence of a transverse magnetic field and it should be unchanged by a longitudinal field. Most materials have a positive transverse magnetoresistance and a much smaller longitudinal magnetoresistance (Putley, 1968). Magnetite has been reported to have both positive and negative transverse magnetoresistance, depending on the magnitude of the applied field, the crystallographic orientation, the temperature, and the origin of the sample (Domenicali, 1950; Zalesskii, 1961; and Kostopoulos, 1970). The reported longitudinal magnetoresistance is of comparable magnitude (Domenicali, 1950).

2.3 Magnetostatic Considerations

2.3.1 Shape Anisotropy in Thin Films

If the thickness of the film is small compared to any planar dimension, a shape induced anisotropy maintains the magnetization in the plane of the film (Maxwell, 1891; Soohoo, 1965). When an external field $H < 4\pi M_s$ is applied perpendicular to the plane of the film, the perpendicular component of the magnetization $4\pi M_\perp$ will acquire a value which is almost equal to H since the demagnetizing factor is nearly unity, and the magnetic induction inside the film is almost exactly equal to the external field.

The use of thin film samples constrains the current flow to the plane of the film. The magnetic properties of thin films therefore guarantee that the perpendicular components of the magnetic vectors are simply determined by knowing the applied field.

2.3.2 Other Anisotropies

The presence of additional anisotropies due to strain or crystalline effects could dominate the shape induced anisotropy and move the equilibrium position of the magnetization out of the plane of the film. A series of magnetic measurements revealed no evidence of measurable uniaxial, crystalline, or strain-induced anisotropies at room temperature.

Below the Verwey temperature, the c-axis of the orthorhombic lattice is the easy-axis. The application of a large magnetic field can align the c-axis parallel to the external magnetic field (Bickford, 1953]. Assuming the highest reported value of the crystalline anisotropy for orthorhombic magnetite, $K = 12 \times 10^6$ erg/cm^3 (Palmer, 1963), the crystalline anisotropy would be greater than the shape induced anisotropy and could thus change the equilibrium position of the magnetization. We found no evidence of such anomalous effects below the Verwey temperature in our samples.

2.4 Summary

The advantage of thin film samples is that the perpendicular components of the magnetic vectors are simply determined by the externally applied field and the current flow is guaranteed to be in the plane of the film. The orientation of the planar component of the magnetization is the only unknown parameter in the experiment and the Hall effect is by definition independent of the planar component of the magnetic field.

The magnetoresistance will be shown to be relatively insensitive to the magnetization.

3. EXPERIMENTAL METHOD

3.1 Sample Preparation

Magnetite samples were prepared by oxidation and reduction of iron thin films. Iron with greater than 99.96% purity was evaporated from alundum crucibles by RF induction heating in a vacuum of better than 10^{-6} Torr. The Corning 0211 glass substrates were outgassed and heated to 200°C during the deposition of the iron. The film thickness was determined from hysteresis loop tracer measurements (Humphrey, 1967] with an estimated accuracy of 3%. The thickness of this first iron film determines the thickness of the final Fe_3O_4 films.

Standard samples were 1 cm circular films. Photolithographic and etching techniques were used after the first iron deposition to define the shapes of other samples. The remaining iron was then oxidized at 400°C in O_2 at 1 atm. for 30 minutes to produce antiferromagnetic α-Fe_2O_3. A second iron film was deposited at room temperature onto the α-Fe_2O_3 and the samples were annealed in a vacuum of better than 10^{-7} Torr at 400°C for 10 hours to complete the formation of Fe_3O_4. The excess pure iron from the second deposition was removed by etching in dilute HNO_3.

Films produced this way have been shown to be polycrystalline and strain-free at room temperature (Feng et al., 1972). Any deviations from stoichiometry should result in films that are slightly iron-rich. In contrast, bulk samples could be iron-deficient because they require

sintering or annealing at over 1000°C (Turner, 1972; Smiltens, 1952), and must usually be inspected for α-Fe_2O_3 or γ-Fe_2O_3 content (Smiltens, 1952).

Samples with three different shapes were used in these experiments. Two-point and four-point resistivity measurements were performed on the standard circular samples. A linear sample with contacts at the ends to supply current and a separate pair of contacts to sense the voltage was used for resistivity and magnetoresistance measurements. This sample was 0.5 mm x 7 mm with 0.1 mm voltage sensing arms separated by about 3 mm. A circular sample with four nearly equally spaced peripheral contacts was used for resistivity, magnetoresistance and Hall effect measurements using the method described by van der Pauw (1958, 1959). This sample was 2 mm in diameter with contact pads connected by 0.15 mm segments.

Typical samples are shown in the top of Fig. 1. Also shown in the inset is a transmission electron micrograph of a carbon replica showing the smoothness of a typical 2500 Å film. (The thickness was determined by measuring the areal density of iron and assuming bulk density.) The pits revealed by the shadows are typically 500-800 Å deep with evidence of shallower, longer range unevenness.

Since the films were about 2500 Å thick, the samples closely approximate ideal two-dimensional configurations. The two-dimensional solutions to the electrical current distributions were used without corrections for the finite thickness of the samples.

3.2 Measurements

The measurements were made at dc as a function of temperature in

a gas flow cryostat (Bilger, 1970). Temperatures were accurate to within ±0.5°K and stable within ±0.15°K. Magnetoelectric effects were measured in fields of 0-23 kOe with the field direction perpendicular to the plane of the sample. The field strength was set with an accuracy of ±10 Oe.

Resistivity was measured on the linear sample by supplying current at the ends and measuring the voltage across the sensing arms. The resistivity of the "van der Pauw" sample was determined by supplying current through two adjacent contacts and measuring the voltage drop on the other pair; all eight possible current polarities and contact pairs were used to measure the resistivity and to determine the symmetry of the sample. The usual precautions were taken to minimize the effects of self-heating of the sample.

Hall effect measurements were performed on the "van der Pauw" sample by applying the current to opposite contacts and measuring the voltage on the other pair. All eight possible combinations of current polarity, contact pairs, and magnetic field direction were used. Prior to each measurement, the sample was saturated in a field of 23 kOe. Then the field was reduced to zero and reversed and measurements were performed at 10 Oe, 4 kOe, 10 kOe, 23 kOe, 10 kOe, and 4 kOe. Then the field was again reversed and the measurements were repeated. The data for increasing field and decreasing field were analyzed separately for evidence of magnetic hysteresis. More detailed measurements were performed at 104°K and 250°K.

The transverse magnetoresistance measurements were made on the linear sample by directly measuring the change in the voltage drop as a

function of the applied transverse magnetic field. The measurements were made in steps of 1 kOe and with only one field direction.

The effect of the planar orientation of the magnetization on the magnetoresistance, or the planar Hall effect, was investigated by two-point and four-point measurements on the 1 cm samples. First, the voltage drop was measured in zero-field conditions. Then a magnetic field of 200 Oe or 450 Oe, larger than the coercive force, was applied parallel to the plane of the film to align the magnetization. The voltage drop was measured as a function of the orientation of the external field with respect to the current flow.

4. RESULTS AND DISCUSSION

4.1 Resistivity

The results of the resistivity measurements are shown in Fig. 2. The room temperature resistivity is 8.5×10^{-3} Ωcm, or about 25% higher than the resistivity in bulk magnetite (Smit and Wijn, 1959). We attribute this difference to the nonuniformity in the thickness of the films as shown in the inset in Fig. 1. The cubic phase has an activation energy of about 62 meV while the orthorhombic phase has an activation energy of about 105 meV. Calhoun (1954) reported activation energies of 30 meV and 110 meV, respectively. The difference in the conductivity and activation energies is not believed to be due to impurities in our samples. Impurity concentrations of less than 4% are known to increase the resistivity, but this also lowers the temperature of the Verwey transition (Epstein, 1954).

The temperature of the Verwey transition was determined in our samples from more detailed resistivity measurements than shown in Fig. 2(Feng and Nicolet, 1974). The transition temperature was taken as the midpoint

between the two conductivity regions and was found to be T_V = 123 ± 1°K, or about 4°K higher than reported for bulk magnetite (Calhoun, 1954). We attribute these differences to stress imposed on the magnetite films by the substrate (Feng and Nicolet, 1974).

4.2 Hall Effect

The results of the Hall effect measurements are shown in Figs. 3, 4 and 5. The polarities of both the ordinary and extraordinary Hall coefficients are negative at all temperatures.

The results of measurements taken in 1 kOe steps at 250°K and 104°K are shown in Fig. 3. The data for increasing and decreasing field at 250°K were analyzed separately for evidence of magnetic hysteresis. Although there is a small systematic difference when the applied field is less than the saturation magnetization ($4\pi M_s$ = 6.0 kG at room temperature (Kittel, 1966)), the largest difference corresponds to a difference in $4\pi M_\perp$ of about 200 G. The differences for $H \geq 4\pi M_s$ are due to the errors of measurement. The data for increasing and decreasing field at 104°K were averaged together since the uncertainties in the measurements were too large to resolve any hysteresis.

The results clearly indicate the presence of two distinct regimes. The low field signal ($H < 4\pi M_s$) is due primarily to the extraordinary Hall effect while the non-zero slope in the high field region is due solely to the ordinary Hall effect. The intersection of the asymptotes to these two sections is at about 5-6 kOe as expected from the saturation magnetization and the demagnetization factor of nearly unity.[1]

At other temperatures, the extraordinary Hall coefficient was determined from the Hall voltages measured at 10 Oe and ±4 kOe and the

[1] It has been shown(p. 188) that there are no significant perpendicular anisotropies.

ordinary Hall coefficient was determined from the difference of the Hall voltages at 10 kOe and 23 kOe. These were chosen as a compromise between signal amplitudes and errors. The small departure at 4 kOe from the asymptote corrects, in part, for the fact that the Hall voltage below technical saturation is due to both the ordinary and extraordinary Hall coefficients.

4.2.1 Extraordinary Hall Effect

The results of the extraordinary Hall effect measurements as a function of temperature are shown in Fig. 4. The X is the room temperature value reported by Lavine (1959). It is in reasonable agreement with the present results. The activation energies are about 26 meV in the cubic phase and 95 meV in the orthorhombic phase.

As stated in Part 2.1, calculations predict that the extraordinary Hall coefficient should have a square law dependence on the resistivity for metallic d-band conduction. The extraordinary Hall coefficient in Fig. 4 as a function of the resistivity (Fig. 2) is shown in Fig. 5. The best power law fit to the data is a $\rho^{1/3}$ dependence above T_V and $\rho^{2/3}$ below T_V. A re-examination of Lavine's (1961) data also produces a $\rho^{1/3}$ dependence over the same temperature range.

4.2.2 Ordinary Hall Effect

The ordinary Hall coefficient as a function of temperature is also shown in Fig. 4. Note that there is almost a factor of 100 difference in the two ordinates. The activation energies of about 22 meV above T_V and about 100 meV below T_V are consistent with the results of Siemons (1970). However, an important difference is that our results indicate a negative Hall coefficient while Siemons reported a positive Hall

coefficient. Siemons attributed part of the Hall voltage at high magnetic fields to the extraordinary Hall effect. The saturation magnetization in his sample varied by about 1% in an external field varying from 10 kOe to 15 kOe. This was claimed to have added an extraordinary Hall signal proportional to the change in the magnetization. After making the correction for this effect, Siemons calculated a net positive Hall coefficient. In our case, the observed ordinary Hall signal was about 10% of the extraordinary Hall voltage. Thus, even if this correction were applied, it would only reduce the ordinary Hall coefficient by 10-20%, but it would not change the sign of the observed ordinary Hall coefficient. Since the field dependence of $4\pi M_s$, if any, is not known in our samples, we did not apply this correction to our data.

One result of the present data is that the ratio of the ordinary and extraordinary Hall coefficients is approximately independent of the temperature and the ratio is only slightly different in the two phases.

4.2.3 Hall Mobility

The Hall mobility can be evaluated from the ordinary Hall effect and resistivity data using the formula

$$\mu_H = 10^8 \cdot \frac{R_o}{\rho}$$

where R_o is in Vcm/AOe, ρ is in Ωcm, and μ_H is in cm^2/Vs. The mobility as a function of temperature is shown in an Arrhenius plot in Fig. 6. Above T_V the mobility has a positive temperature coefficient with an activation energy of about 39 meV. Although the Hall mobility data shows no definite temperature dependence below T_V,

the measurements were confined to 104-120°K and cannot be considered conclusive. The best fit of a power law dependence to the present mobility measurements varies from about $T^{4\pm1}$ at low temperatures to about $T^{3\pm1}$ near room temperature.

4.3 Magnetoresistance

4.3.1 Dependence on the Orientation of the Magnetization

Magnetoresistance is an even function of both the transverse and longitudinal components of the magnetic field. If the magnetoresistance is a function of the magnetization, it must be measured with the magnetization both parallel and perpendicular to the current. Since the shape-induced planar anisotropies are small, the magnetization can be oriented in the plane with small bias fields. Any magnetoresistance observed as a function of the position of the magnetization in the plane, or planar Hall effect, will be due primarily to the magnetization since the required bias fields will be much smaller than the magnetization.

We have performed such measurements by two-point and four-point measurements on 1 cm diameter samples. The orientation of the magnetization in the plane of the film was established using planar bias fields of 200 Oe and 450 Oe. The apparent resistivity did not change measurably when the magnetization was rotated. We therefore conclude that the upper limit on the magnetoresistance due to the magnetization is $\leq$ 0.2% at room temperature.

4.3.2 Dependence on the Transverse Applied Field

The transverse magnetoresistance was measured as a function of both the applied field and the temperature. The change in the voltage

drop in the linear sample, normalized to the zero field voltage drop, is shown in Fig. 7 as a function of the applied field at 250°K. The magnetoresistance was also determined by analyzing the Hall effect data from the "van der Pauw" samples with the induced voltage normalized to the offset voltage caused by the asymmetry in the position of the contacts. These results are also shown in Fig. 7. A comparison shows that the two methods agree within 15-30%, but the magnitude of the results from the "van der Pauw" samples are systematically larger than those from the linear sample. The magnetoresistance is negative and quadratic at low magnetic fields. There is an inflection point in the field dependence near saturation and the magntiude increases monotonically to about 4% at a magnetic field of 23 kOe. This type of qualitative field dependence is typical for all temperatures investigated.

The results of the transverse magnetoresistance measurements at 4 kOe, 10 kOe, and 23 kOe are shown in Fig. 8, as a function of temperature. The error bars shown in the 23 kOe points in the "van der Pauw" samples are typical of the errors for all measurements made at that temperature on those samples. The estimated error in the data taken on the linear sample is about ± ½% for all points with the errors increasing slightly at lower temperature. The data shows that the high field magnetoresistance has an extremum in the temperature dependence near the Verwey temperature and that it is negative for all temperatures and field strengths. The magnetoresistance reaches 7-7½% at about 130°K and 23 kOe.

The present transverse magnetoresistance results differ significantly from those previously reported. The magnitude of the magnetoresistance in our measurements increases monotonically with the magnetic field at all temperatures. It is the largest ever observed in cubic magnetite. It does not exhibit any change in sign. It is quadratic at low magnetic fields and does not saturate with the magnetization. The magnetoresistance has its maximum magnitude at about 130°K and decreases at higher and lower temperatures.

The present measurements also separate the effects of the applied field and the spontaneous magnetization on the transverse magnetoresistance. At room temperature, it is apparently dominated by the externally applied field and almost unaffected by the magnetization. An alternative explanation is that the transverse and longitudinal magnetoresistances due to the magnetization could have the same magnitude. The differences in these interpretations cannot be tested experimentally.

We suspect that the general lack of agreement on the transverse magnetoresistance of the cubic phase (Domenicali, 1950; Zalesskii, 1961; and Kostopoulos, 1970) is due to impurities in the samples since most of the previously reported results were taken on natural magnetite crystals. The present measurements were performed on synthetic samples whose impurity content is believed to be low. We believe that the essential qualitative features of our result will be reproduced on synthetic, single crystal samples. Note however that our samples are polycrystalline and the results are therefore averages over all crystallographic directions.

The results below T_V agree qualitatively with those of Kostopoulos (1972) despite the differences in the results above T_V. This suggests that the low temperature magnetoresistance may be dominated by the structure and the change in the specific resistivity will be approximately independent of the sample.

5. CONCLUSIONS

The results are summarized in Table I.

The resistivity measurements demonstrate that the properties of thin films of magnetite are basically similar to those of bulk magnetite. Both forms exhibit a thermally activated conductivity and the conductivity transition is present in both cases. The different activation energies, higher Verwey transition temperature, and smaller resistivity change at the transition observed in the thin films are unique to thin film samples.

The extraordinary Hall coefficient R_1 has been shown to have a power law dependence on the resistivity. The best fit to the present results indicates that R_1 is proportional to $\rho^{1/3}$ in the cubic phase and $\rho^{2/3}$ in the orthorhombic phase.

The ordinary Hall coefficient is negative. This is usually interpreted as a result of electronic conductivity.

While the Hall effect, a first order phenomenon in the magnetic field, is dominated by the spontaneous magnetization, the magnetoresistance, a second order effect due to the magnetic field, is apparently insensitive to the magnetization.

The present measurements show that the transverse magnetoresistance due to an externally applied field is negative at all temperatures and field strengths. It is quadratic at low magnetic fields and it increases monotonically without saturating up to 23 kOe. The magnitude of the magnetoresistance is large in magnetite and is of the order of 2-4% at 10 kOe.

These results illustrate some of the advantages and disadvantages of performing galvanomagnetic measurements on thin films of ferromagnetic materials. Ferromagnetic films have demagnetizing factors of almost exactly unity. In the absence of crystalline or perpendicular anisotropies, the perpendicular components of the magnetic field are simply determined by knowing the applied field, and the effects of the applied field and the spontaneous magnetization can be easily separated. The electrical current and potential distributions are easily determined from the geometry and two-dimension potential theory with negligible corrections for the finite thickness of the samples. Since the samples are synthetic, the composition should be well established. The potential disadvantages are the polycrystallinity of the samples and the possibility of anomalous results due to the presence of a substrate. It may be possible to produce epitaxial single crystal films. However, measurements on polycrystalline samples obviously reflect averages over all possible crystallographic directions. The presence of a mechanical substrate-sample interaction can be minimized by a judicious choice of substrates. However, it can also be used advantageously to study the effect of large amounts of tensile stress on the properties of a material.

6. ACKNOWLEDGMENTS

This work would not have been possible without the cooperation of J. L. Beauchamp, who kindly allowed us to use his electromagnet. We are also indebted to F. B. Humphrey, T. M. Morris, and C. H. Wilts for the use of their facilities and for guidance. We thank C. H. Bajorek (IBM - Thomas J. Watson Research Center) for providing the electron micrograph and for helpful discussions. Thanks are also due to T. C. McGill for stimulating conversations on electronic transport in solids.

REFERENCES

Berger, L., 1972, Phys. Rev. B5, 1862-1870.

Bickford, L. R., 1953, Rev. Mod. Phys. 25, 75-79.

Bilger, H. R. and M-A. Nicolet, 1970, Rev. Sci. Inst. 41, 346-347.

Calhoun, B. A., 1954, Phys. Rev. 94, 1577-1585.

Constantin, C. and Rosenberg, M., 1972, Proc. 18th Conf. on Mag. Mat.

Domenicali, C. A., 1950, Phys. Rev. 78, 458-467.

Drabble, J. R., T. D. Whyte and R. M. Hooper, 1971, Sol. St. Comm. 9, 275-278.

Epstein, J. H., 1954 (thesis, MIT).

Feng, J.S.-Y., C. H. Bajorek, and M-A. Nicolet, 1972, IEEE Trans. Magnetics MAG-8, 277-278.

Feng, J. S.-Y. and M-A. Nicolet, 1974, (unpublished).

Heikes, R. R. and W. D. Johnston, 1959, J. Chem. Phys. 26, 582.

Humphrey, F. B., 1967, J. Appl. Phys. 38, 1520-1527.

Karplus, R. and J. M. Luttinger, 1954, Phys. Rev. 95, 1154-1160.

Kittel, C., 1966, Introduction of Solid State Physics, (New York, Wiley), 461.

Kostopoulos, D., 1972, Phys. Stat. Sol.(a) 9, 523-527.

Kostopoulos, D. and A. Theodossiou, 1970, Phys. Stat. Sol.(a) 2, 73-78.

Lavine, J. M., 1959, Phys. Rev. 114, 482-488.

Lavine, J. M., 1961, Phys. Rev. 123, 1273-1277.

Li, C. H., 1932, Phys. Rev. 40, 1002.

Maxwell, J. C., 1891, A Treatise on Electricity and Magnetism, 3rd Ed. (Oxford, Clarendon Press) Vol. 2, p. 66.

Miller, R. W., 1929, J. Amer. Chem. Soc. 51, 215.

Palmer, W., 1963, Phys. Rev. 131, 1057-1062.

Pugh, E. M. and Rostoker, N., 1953, Rev. Mod. Phys. 25, 151-157.

Putley, E. H., 1968, The Hall Effect and Semiconductor Physics, (New York, Dover Publications).

Siemons, W. J., 1970, IBM J. Res. Develop. 14, 245-247.

Smiltens, J., 1952, J. Chem. Phys. 20, 990-994.

Smit, J. and H. P. J. Wijn, 1959, Ferrites (New York, J. Wiley & Sons) 229.

Soohoo, R. F., 1965, Magnetic Thin Films (New York, Harper & Row) 56-59.

Turner, C. E., 1972, J. Phys. C5, 2859-2866.

van der Pauw, L. J., 1958, Philips Res. Repts. 13, 1-9.

van der Pauw, L. J., 1959, Philips Tech. Rev. 20, 220-224.

Verwey, E. J. W., P. W. Haaijman and F. C. Romeijn, 1947, J. Chem. Phys. 15, 181.

Weiss, P., 1896 (Paris, thesis).

Zalesskii, A.V., 1961, Sov. Phys. Cryst. 6, 180-185.

FIGURE CAPTIONS

Fig. 1 Macroscopic and microscopic views. Three typical 2500 Å samples on glass substrates are shown next to a scale. The samples, from left to right, are a standard 1 cm diameter film, a "van der Pauw" sample, and a linear sample. The inset shows a transmission electron micrograph of a carbon replica taken from a typical 2500 Å film. The sphere is 5000 Å in diameter.

Fig. 2 The resistivity of 2500 Å Fe_3O_4 on Corning 0211 glass as a function of temperature. The Verwey transition is clearly indicated but the change in the resistivity is not as large as in bulk samples. The transition also occurs at a slightly higher temperature than in bulk magnetite. These differences are due to substrate-induced stresses.

Fig. 3 Hall resistivity of 2500 Å Fe_3O_4 on Corning 0211 glass as a function of the applied magnetic field. The top figure shows the Hall resistivity at 250°K. The data for increasing and decreasing field was analyzed separately and they reveal the existence of a small magnetic hysteresis below technical saturation. The ordinary and extraordinary Hall coefficients are both negative. The bottom part shows the Hall resistivity at 104°K. There is no evidence of polarity reversal as reported by Kostopoulos and Theodossiou (1970). The scatter in the data points is due to temperature variations of about $\pm$ 0.1°K.

Fig. 4 The ordinary and extraordinary Hall coefficients as a function of temperature. Note that there is almost a factor of 100

difference in the two ordinates. Also shown for comparison is the value of R_1 reported by Lavine (1959). Note that the ratio of the ordinary and extraordinary Hall coefficients is approximately constant in both the cubic and orthorhombic phases. The error bars shown are estimates of the typical errors above and below T_V.

Fig. 5 The extraordinary Hall coefficient as a function of the resistivity. The best power law fits to these data are a $\rho^{1/3}$ dependence in the cubic phase and $\rho^{2/3}$ below T_V. The two error bars shown are estimates of the typical errors above and below T_V.

Fig. 6 Hall mobility as a function of temperature. The positive temperature coefficient in the cubic phase is evidence of hopping conductivity. The error bar shown above T_V is an estimate of the errors typical for the cubic phase. The error bars shown below T_V indicate that the present data are insufficient to clearly reveal a temperature dependence for the orthorhombic phase.

Fig. 7 Magnetoresistance as a function of the applied field at 250°K. The magnetoresistance is negative for all magnetic field strengths. The data for increasing and decreasing magnetic field on the "van der Pauw" sample (open symbols) are shown separately to reveal the hysteresis. The data from the linear samples (filled symbols) were taken with increasing field. The magnetoresistance is quadratic at low fields and

does not saturate or become linear at applied fields up to 23 kOe. This relative field dependence is typical for all temperatures investigated. Simultaneous Hall effect measurements (Fig. 3) give clear evidence of the saturation of the perpendicular component of the spontaneous magnetization.

Fig. 8 The magnetoresistance as a function of temperature. The magnetoresistance is negative at all temperatures and all magnetic field strengths investigated. The data shown are for both the linear sample (filled symbols) and the "van der Pauw" samples (open symbols) at 4 kOe (circles), 10 kOe (diamonds) and 23 kOe (triangles). The error bars shown on the 23 kOe data from the "van der Pauw" sample are also applicable to the data taken at the same temperature but at lower magnetic fields. The two error bars shown for the linear sample are estimates of the typical errors above and below T_V.

TABLE I

GALVANOMAGNETIC PROPERTIES OF MAGNETITE THIN FILMS

Verwey Transition Temperature	$T_V^{film} = 123°K > T_V^{bulk} = 119.4°K$ T_V elevated by substrate-induced stresses			
	$T > T_V$		$T < T_V$	
Property	Value at $T = 250°K$	Activation Energy (meV)	Value at $T = 100°K$	Activation Energy (meV)
Resistivity ρ (Ωcm)	$1.1 \pm 0.1 \times 10^{-2}$	62 ± 6	$6.5 \pm 0.5 \times 10^{0}$	105 ± 5
Ordinary Hall Coefficient R_0 (Vcm/AOe)	$-1.1 \pm 0.1 \times 10^{-10}$	22 ± 5	$-5.2 \pm 0.4 \times 10^{-9}$	100 ± 10
Extraordinary Hall Coefficient R_1 (Vcm/AG)	$-2.6 \pm 0.4 \times 10^{-8}$	26 ± 3	$8.5 \pm 0.9 \times 10^{-7}$	95 ± 10
Hall Mobility μ_H (cm^2/VS)	$1.0 \pm 0.2 \times 10^{0}$	39 ± 7	$7 \pm 3 \times 10^{-2}$	5 ± 12
Magneto-resistance $\left\lvert\frac{\Delta\rho(H)}{\rho(0)}\right\rvert$	negative temperature coefficient		positive temperature coefficient	
	Quadratic at low magnetic fields and increases monotonically without saturating to 23 kOe.			

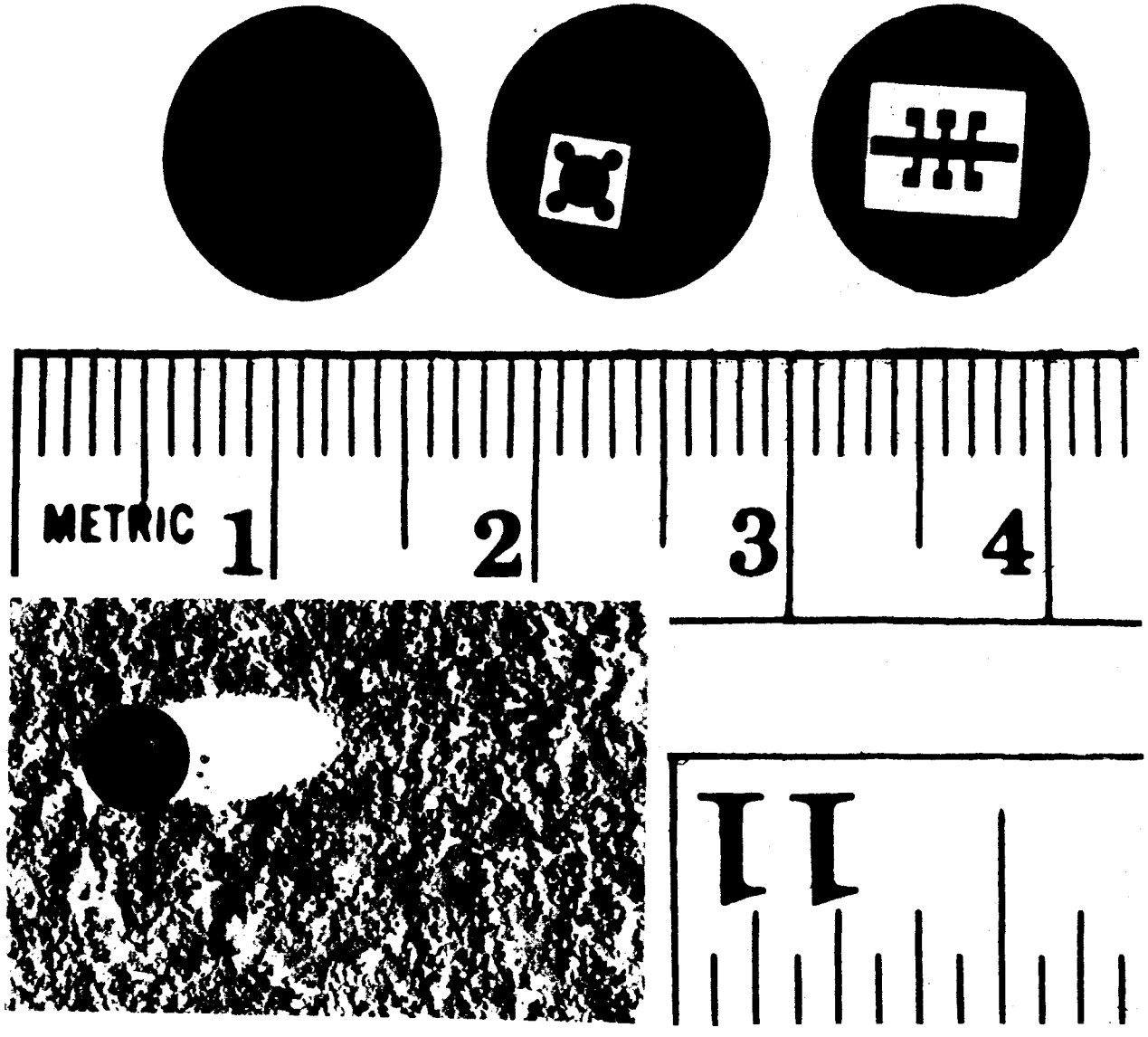
METRIC
1
2
3
4
11

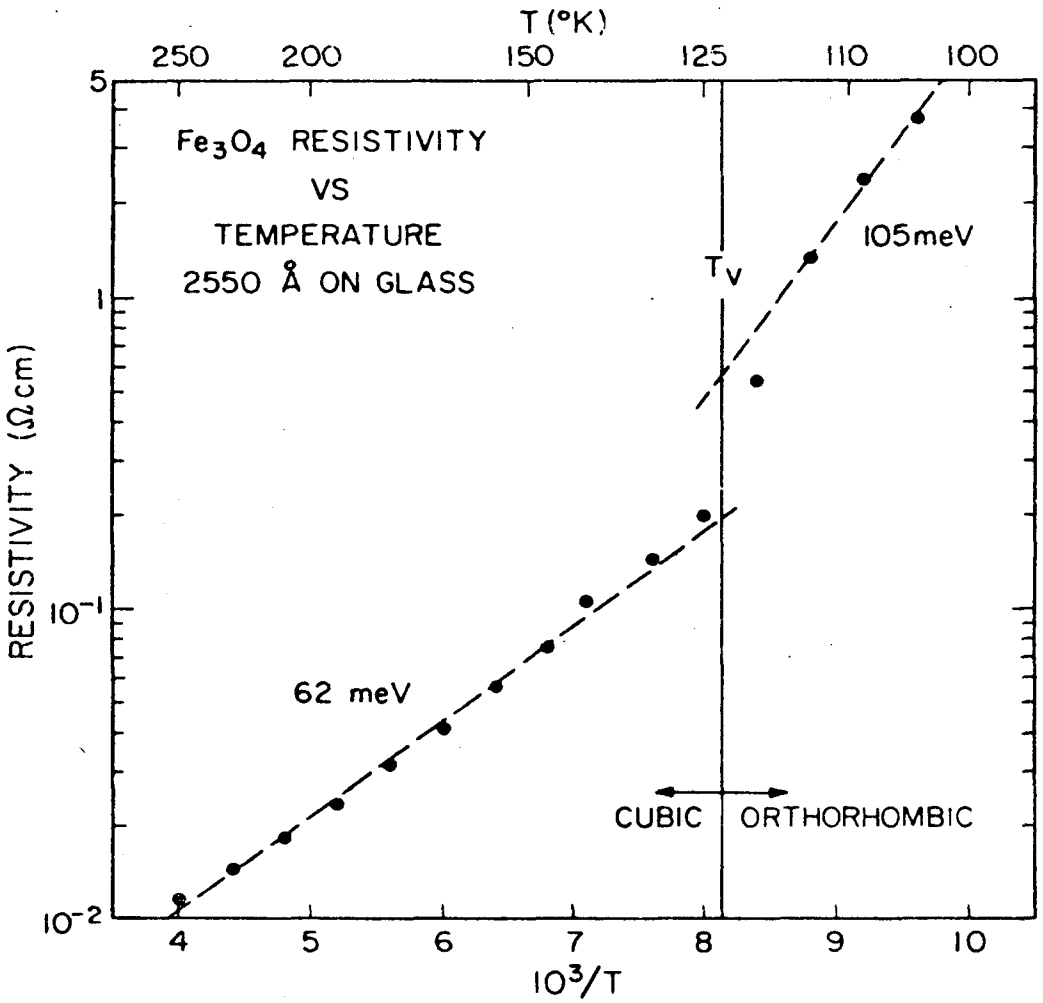
T (°K)
250
200
150
125
110
100
5
1
10^{-1}
10^{-2}
RESISTIVITY (Ω cm)
Fe_3O_4 RESISTIVITY
VS
TEMPERATURE
2550 Å ON GLASS
T_V
105meV
62 meV
CUBIC
ORTHORHOMBIC
4
5
6
7
8
9
10
$10^3/T$

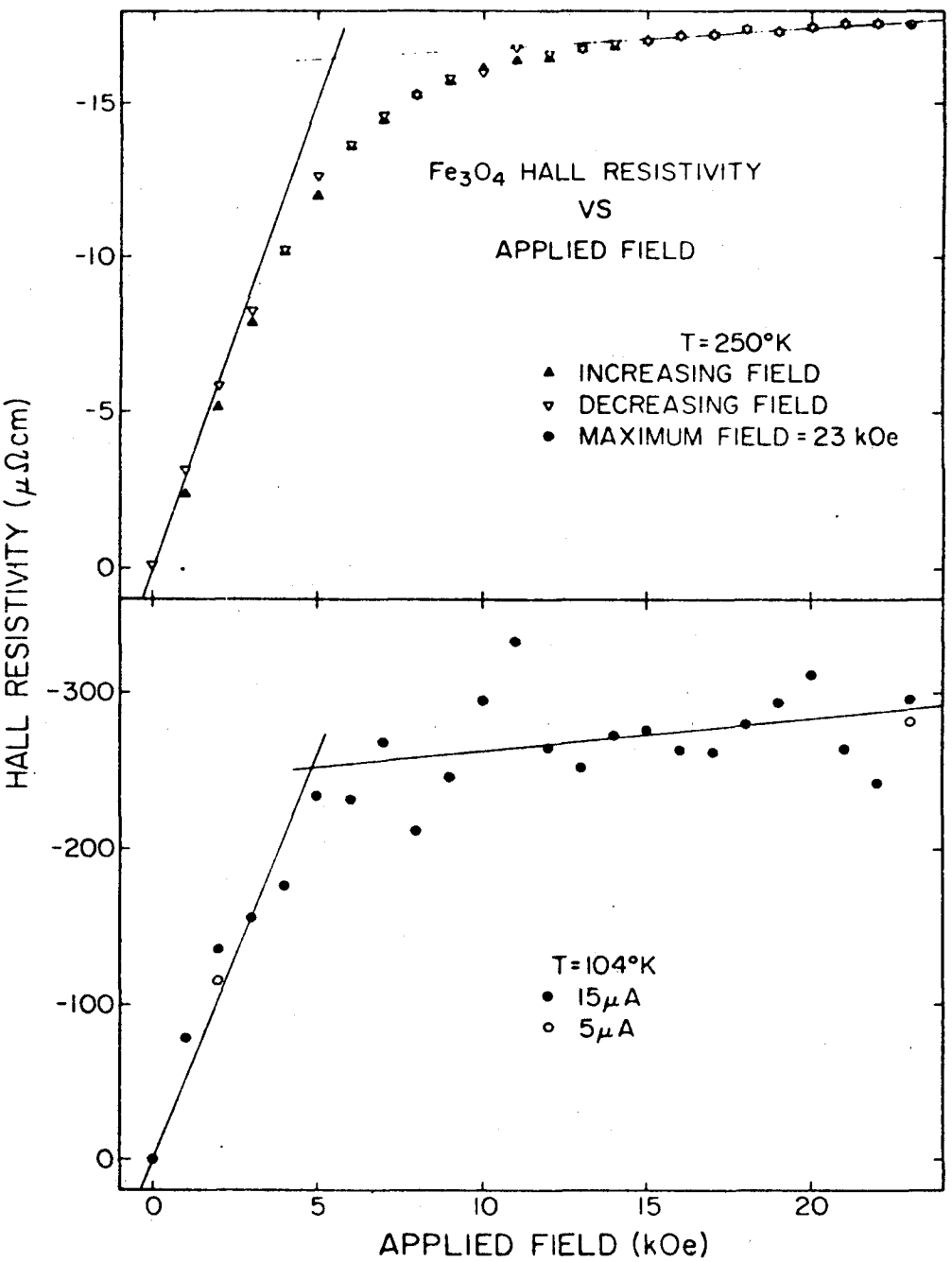
Fe_3O_4 HALL RESISTIVITY
VS
APPLIED FIELD
T=250°K
▲ INCREASING FIELD
▽ DECREASING FIELD
● MAXIMUM FIELD = 23 kOe
T=104°K
● 15μA
○ 5μA
HALL RESISTIVITY (μΩcm)
APPLIED FIELD (kOe)
-15
-10
-5
0
-300
-200
-100
0
0
5
10
15
20

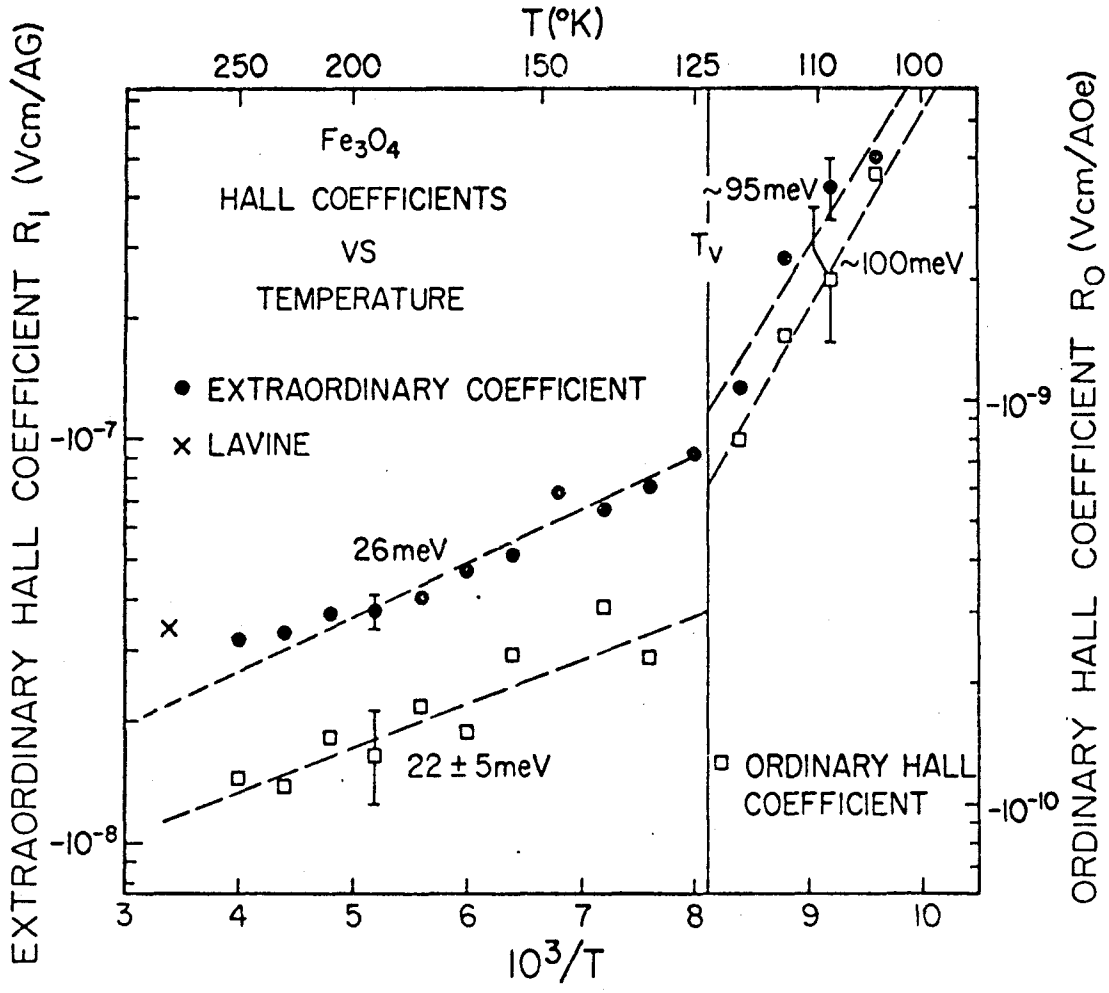
T(°K)
250
200
150
125
110
100
Fe_3O_4
HALL COEFFICIENTS
VS
TEMPERATURE
~95meV
T_V
~100meV
EXTRAORDINARY COEFFICIENT
LAVINE
26meV
22 ± 5meV
ORDINARY HALL
COEFFICIENT
EXTRAORDINARY HALL COEFFICIENT R_I (Vcm/AG)
ORDINARY HALL COEFFICIENT R_O (Vcm/AOe)
-10^{-7}
-10^{-8}
-10^{-9}
-10^{-10}
3
4
5
6
7
8
9
10
$10^3/T$

JSF RDP
MAN 4

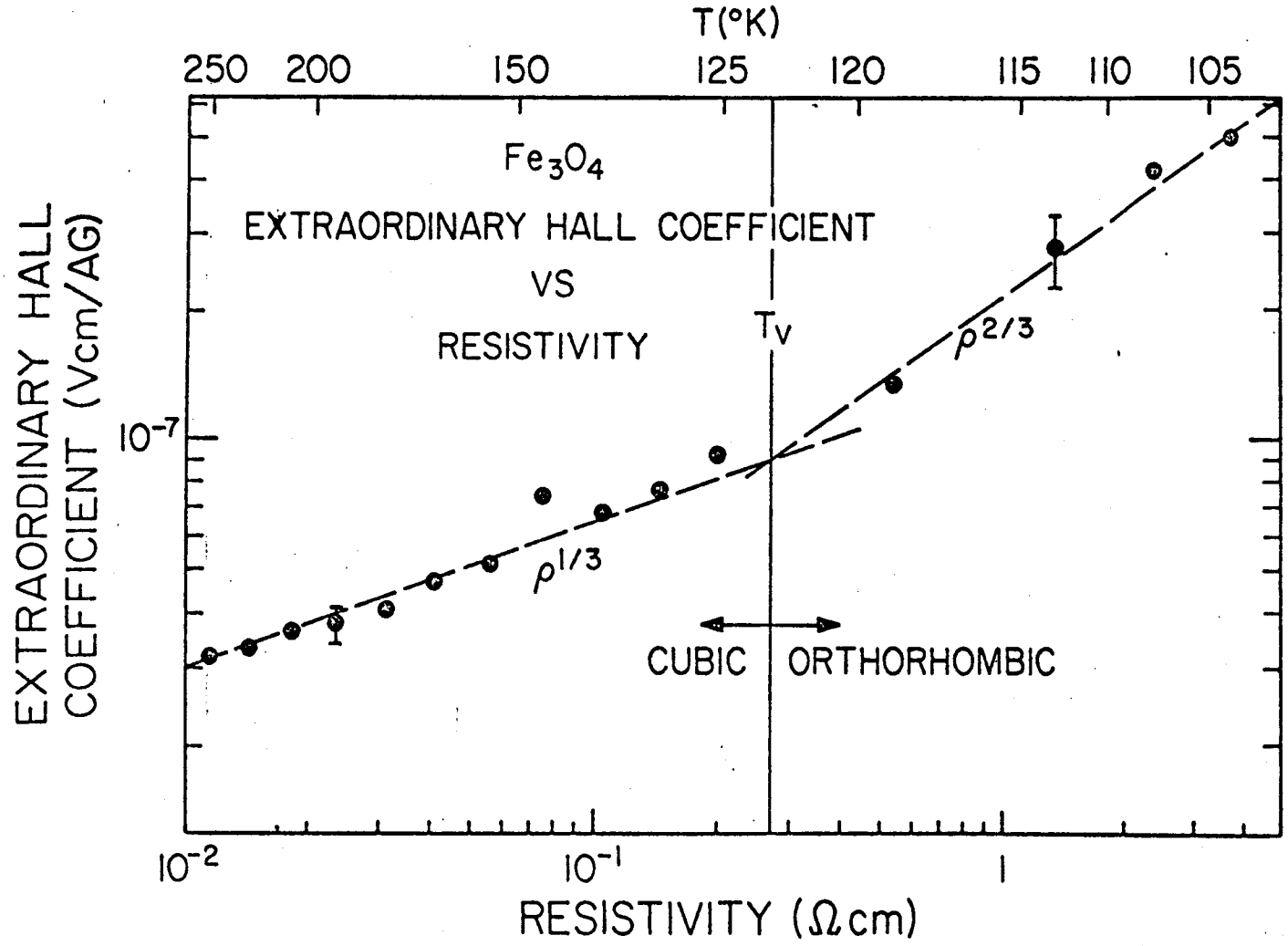
T(°K)
250
200
150
125
120
115
110
105
Fe_3O_4
EXTRAORDINARY HALL COEFFICIENT
VS
RESISTIVITY
T_V
$\rho^{2/3}$
$\rho^{1/3}$
CUBIC
ORTHORHOMBIC
EXTRAORDINARY HALL COEFFICIENT (Vcm/AG)
10^{-7}
10^{-2}
10^{-1}
1
RESISTIVITY (Ωcm)

JSF RDP
MAN 5

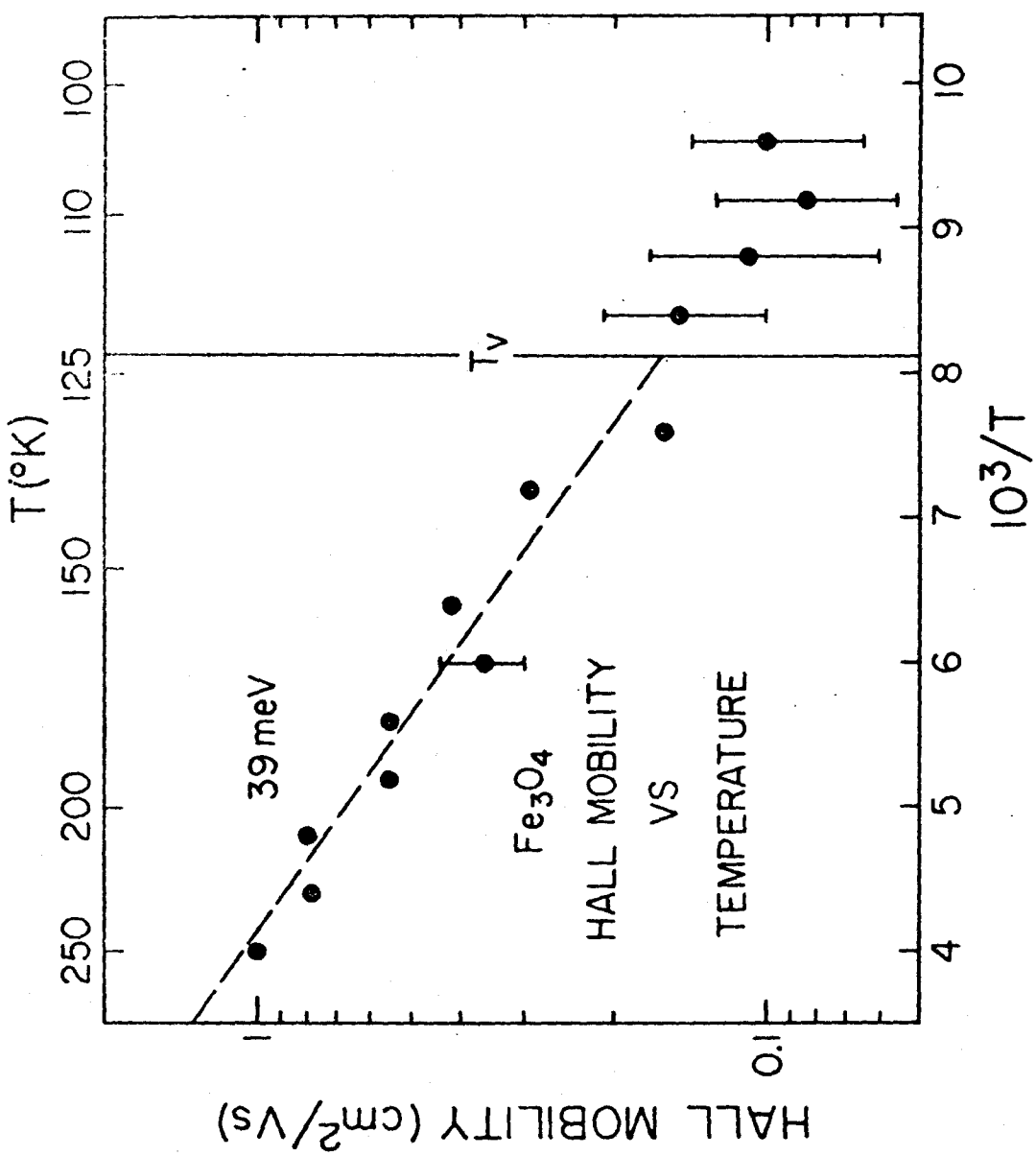
HALL MOBILITY (cm²/Vs)
1
0.1
T (°K)
250
200
150
125
110
100
10³/T
4
5
6
7
8
9
10
Tv
39 meV
Fe3O4
HALL MOBILITY
VS
TEMPERATURE

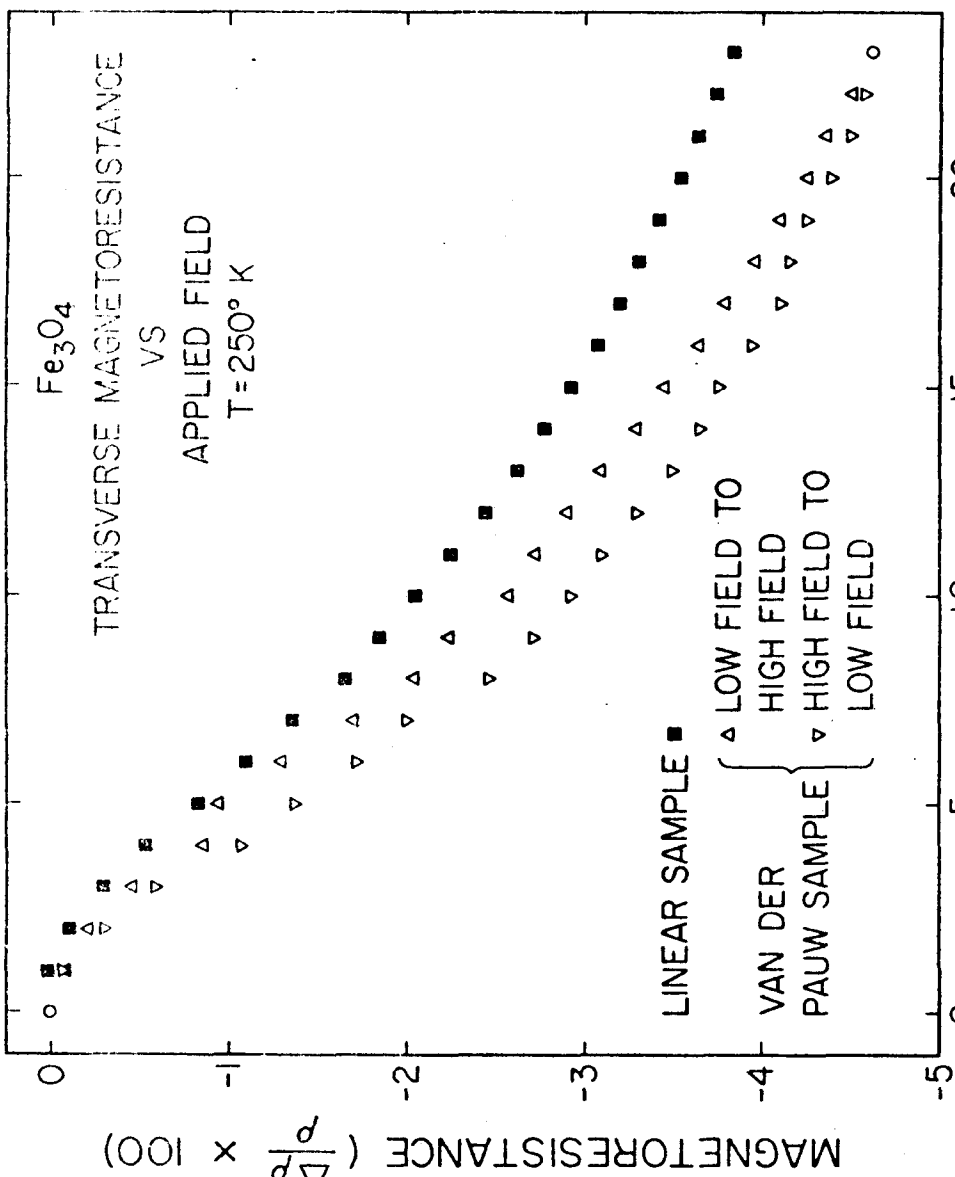
Fe_3O_4
TRANSVERSE MAGNETORESISTANCE
VS
APPLIED FIELD
T=250° K
LINEAR SAMPLE
VAN DER PAUW SAMPLE
LOW FIELD TO HIGH FIELD
HIGH FIELD TO LOW FIELD
MAGNETORESISTANCE ($\frac{\Delta\rho}{\rho}$ x 100)
APPLIED FIELD (kOe)
0
-1
-2
-3
-4
-5
5
10
15
20

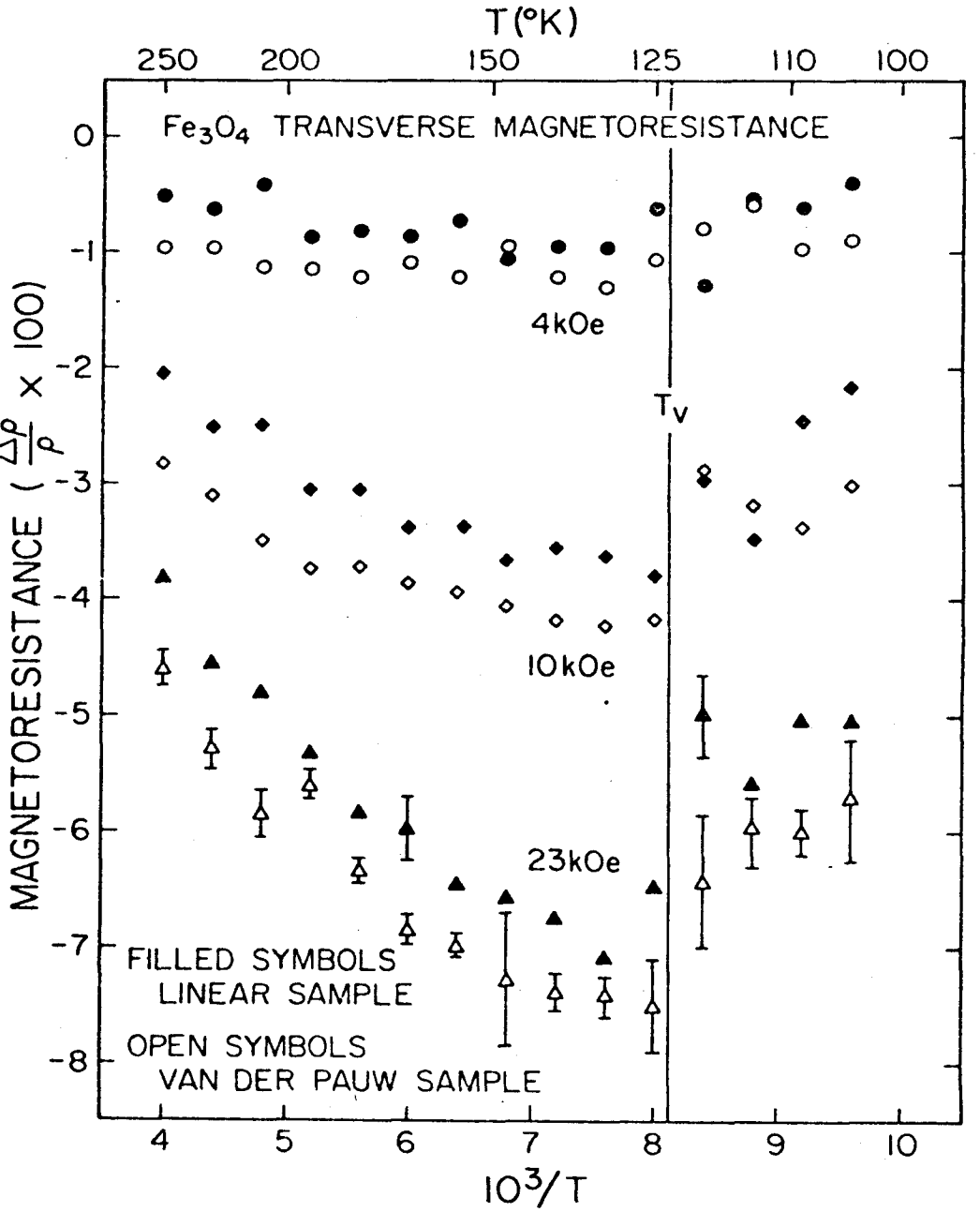
T(°K)
250
200
150
125
110
100
Fe_3O_4 TRANSVERSE MAGNETORESISTANCE
4kOe
T_V
10kOe
23kOe
FILLED SYMBOLS
LINEAR SAMPLE
OPEN SYMBOLS
VAN DER PAUW SAMPLE
MAGNETORESISTANCE ($\frac{\Delta\rho}{\rho}$ X 100)
0
-1
-2
-3
-4
-5
-6
-7
-8
4
5
6
7
8
9
10
$10^3/T$

3.3 Additional Discussion to "Magnetoelectric Properties of Magnetite Thin Films"

It has been proposed, as a refinement on the Verwey model for the high temperature form of magnetite, that the conductivity in Fe_3O_4 is due to a thermally activated hopping mechanism, and small polaronic conductivity in particular. Camphausen(1972) has given a criterion for the applicability of small polaron theory to the conductivity in magnetite that requires that

$$2J < \eta \hbar \omega / 2$$

where J is an electronic resonance integral that, according to his Eq. 8, is proportional to the square root of the mobility. Camphausen has evaluated the right hand side of the inequality and gives a value of 240 meV for $\eta\hbar\omega/2$. Using Siemon's value of the Hall mobility(1970) at room temperature of about $0.1\ cm^2/Vs$, Camphausen has estimated the upper limit of J as about 65 meV, a value that satisfies his criterion. Scaling new values of J according to the square root of the mobility, as suggested by Camphausen's Eq. 8, gives an upper limit of about 300 meV when the present value of μ_H is used and an upper limit of about 160 meV when Lavine's value(1959) is used. Neither of these values satisfies Camphausen's criterion for small polaronic conductivity.

It should be noted that Camphausen's criterion probably applies to the drift mobility, so all of the above has assumed that the Hall and drift mobilities are approximately equal. Holstein(1961) and Friedman and Holstein(1963) have predicted that the Hall and drift mobilities in small polaronic conductivity may differ by over an order of magnitude,

depending on the details of the hopping mechanism. If these theories are correct and applicable, the use of the Hall mobility in Camphausen's test may not be valid.

In the magnetoresistance measurements, a comparison of the present results and those previously published suggests that the magnetoresistance is strongly affected by the quantity and lattice location of the impurities in the sample. For example, if an impurity were on an octahedral site, it could interrupt the "helical" path of the conduction electron, while an impurity on a tetrahedral site would probably have a much smaller effect on the conductivity properties. An ordering of the impurities on particular lattice sites could thus explain some of the anisotropies reported by Zalesskii(1961). The positive magnetoresistance observed in the natural samples at low fields also appears to be a consequence of the impurities. However, the microscopic origin of a positive magnetoresistance in a magnetic semiconductor is clearly beyond the scope of this work.

In the magnetoresistance measurements below the Verwey transition temperature, not only is there qualitative agreement, as stated in the preprint, but there is also rough quantitative agreement as well. In the present measurements, the change in the specific resistivity at 105°K from zero applied field to 10 kOe is 88±40 mΩcm or 124±20 mΩcm, depending on the sample. Assuming that Kostopoulos(1972) took his magnetoresistance data using the same sample as he used for the Hall effect measurements(Kostopoulos and Theodossiou, 1970), the total resistivity change in his sample at 100°K and from low field to 10 kOe is about 140 mΩcm. Although this is not sufficient evidence to prove

conclusively that the magnetoresistance in the orthorhombic phase is independent of the impurity concentration at low impurity levels, it does support the possibility that this is true.

ADDITIONAL REFERENCES

Chapter 3

I. Balberg, 1970, Phys. Rev. Lett. vol. 25, p. 1294.

D. L. Camphausen, 1972, Sol. St. Comm., vol. 11, p. 99.

C. A. Domenicali, 1950, Phys. Rev., vol. 78, p. 458.

L. Friedman and T. Holstein, 1963, Annals of Physics, vol. 21, p. 494.

T. Holstein, 1961, Phys. Rev., vol. 124, p. 1329.

D. Kostopoulos, 1972, phys. stat. sol.(a), vol. 9, p. 523.

D. Kostopoulos and A. Theodossiou, 1970, phys. stat. sol.(a), vol. 2, p. 73.

J. M. Lavine, 1959, Phys. Rev., vol. 114, p. 482.

J. M. Lavine, 1961, Phys. Rev., vol. 123, p. 1273.

W. J. Siemons, 1970, IBM J. Res. Develop., vol. 14, p. 245.

A. V. Zalesskii, 1961, Sov. Phys. Cryst., vol. 6, p. 180.

Chapter 4

THE VERWEY TRANSITION IN THIN FILMS

4.1 Introduction

Ever since Weiss(1896) first observed the conductivity transition now associated with the Verwey transition, the temperature dependence of the resistivity in magnetite has been investigated ad nauseam. To list all of the available literature on this subject would be both boring and not very instructive. Among those experiments that have clearly proven illuminating have been the doping dependence(Epstein, 1954), the pressure dependence(Samara, 1968), and the effects of including γ-Fe_2O_3 in the sample(presumably in solid solution)(Verwey and Haayman, 1941) on the electrical conductivity and the Verwey transition in particular. Hopefully, the present work will eventually be remembered among the latter rather than become lost among the former.

In the investigations of the galvanomagnetic properties described in the previous chapter, the Verwey transition was observed at about 123±1°K. This is higher than any previously reported value for the transition temperature. In the three experiments cited in the previous paragraph, every change in the sample reduced the observed transition temperature. This is such a well-known effect that the depression of the Verwey transition temperature is sometimes used as a simple test of the purity of a magnetite sample(see Kostopoulos and Theodossiou, 1970, for their discussion of their sample). The other anomaly in the present results is the small conductivity change observed in the transition. Pure magnetite has the largest conductivity change at the transition of

all the ferrites, and impurities are known to reduce this conductivity change while simultaneously depressing the transition temperature (Epstein, 1954). Simultaneously observing a decrease in the change in the conductivity and an increase in the transition temperature is inexplicable on the basis of previously reported experiments.

The present measurements were initiated to identify the origins of this anomalous behavior in the thin films. There are only two obvious parameters that can affect the properties of a thin film. The first is the effect of the substrate on the thin film either through a chemical of mechanical interaction. The second is the effect of the film thickness on its macroscopic properties; these are usually attributed to scattering of the electrons from the surfaces or some collective property that might be thickness dependent. Since the mean free path of an electron in magnetite is estimated to be about 5-10 Å, and since the grain size is about 200-1000 Å(Muret, 1974), neither of these two thickness effects are likely to affect the Verwey transition. The possibility of chemical and mechanical interactions were separated by including some substrates that were chemically similar(identical composition) but with different mechanical properties. Electrical measurements were used because these were the most convenient of the available techniques for investigating the Verwey transition and also the most relevant in the present context. Some of the results obtained in these experiments suggest other experiments that could verify or disprove our interpretations. Unfortunately, these experiments are at best very difficult.

4.2 Results

The results of the investigations of the substrate effects on the Verwey transition are presented in the enclosed preprint. This is the manuscript of a paper that has been submitted to the Journal of the Physics and Chemistry of Solids. At the present time, it is still being considered by the editor and referee(s) for publication in that journal.

SUBSTRATE EFFECTS ON MAGNETITE THIN FILMS*

by

J. S.-Y. Feng and M-A. Nicolet

California Institute of Technology
Pasadena, California 91106

ABSTRACT

The Verwey transition in magnetite thin films has been investigated by measuring the temperature dependence of the sheet resistivity. Substrate-induced stresses raise the transition temperature above the 119.4°K reported for bulk magnetite. The ratio of the resistances of the two phases at the transition temperature is independent of the substrate and proportional to the thickness of the sample, suggesting that a 600-1200 Å surface layer remains in the high conductivity phase at all temperatures.

*Supported in part by the Office of Naval Research (L. Cooper).

Magnetite exhibits the so-called Verwey transition at 119.4°K (T_V). Associated with this first order phase transition are a specific heat anomaly, changes in the magnetic properties, a conductivity transition from a semiconducting to an insulating state, and a structural transformation from cubic inverse spinel to orthorhombic symmetry.[1] The conductivity in the high temperature, cubic phase is believed to be due to the electrons on the randomly half-filled octahedral sites; the change to the orthorhombic structure destroys the equivalence of these sites, resulting in an ordering of the divalent and trivalent iron ions and producing a reduction in the conductivity.[2]

At the Verwey temperature, the bulk conductivity changes by about two orders of magnitude. Deviations from stoichiometry reduce both the transition temperature and the relative conductivity change at the transition.[3]

Samara has shown that the application of hydrostatic pressure also reduces the temperature of the Verwey transition.[4] This pressure dependence has been cited as evidence that the conductivity transition is of the Mott-Wigner type, where an increase in the density delocalizes the electronic wavefunctions to produce a high-conductivity state.[4] It follows that the transition to the low conductivity state can be induced by applying tensile stress to increase the interatomic spacing.

Our measurements were performed on 700 - 6000Å thick magnetite films on chemically inert and insulating substrates.

The details of the sample fabrication procedure have been described elsewhere.[5] The film thicknesses were determined by measuring the areal density of the iron and assuming bulk density for the Fe_3O_4. The measurements were performed over the temperature range of 100 - 300°K in a gas flow cryostat[6] using the four-terminal procedures described by van der Pauw.[7]

The substrates used in this study were fused quartz, pyrex, thermally oxidized silicon, Corning 7059 glass, Corning 0211 glass, $(11\bar{2}0)$ α-Al_2O_3, $Gd_3Ga_2O_{12}$, At-cut quartz and (100)MgO. These materials have a range of tabulated thermal expansion coefficients (β) of $0.5\times10^{-6}/°C$ to $11.7\times10^{-6}/°C$, with applicable temperatures in the range 0-300°C, depending on the material. Néel has reported that for 0-1000°C, $\beta(Fe_3O_4)$ is about $16\times10^{-6}/°C$.[8] In this experiment, we need to know the expansion coefficients for 100-300°K. Since these are not readily available, we have assumed that the relative temperature dependent is about the same for all substrates. Thus, since $\beta(MgO)>\beta(Al_2O_3)$ above room temperature, we assume that $\beta(MgO)$ will be larger than $\beta(Al_2O_3)$ for all applicable temperatures above 100°K.

The results of the resistance measurements for 4700Å films on various substrates are shown in Fig. 1. The resistivity transition is evident in all the samples except the ones on fused quartz and pyrex, the two substrates with the lowest expansion coefficients. The results show that, except for these two special cases, the films all have similar temperature dependences. The only systematic change is the shift in the transition temperature.

The present results differ significantly from those of

bulk magnetite. The activation energy of the cubic phase is about 60 meV in the thin film samples compared to the 39 meV reported for bulk Fe_3O_4.[9] The resistance change at the transition is only a factor of four, which is much smaller than the factor of 90 observed in bulk samples.[10] The activation energy in the orthorhombic phase is about 90 meV, while the value reported for bulk magnetite is over 100 meV.[10]

These three parameters and the Verwey transition temperature have been plotted as a function of the tabulated expansion coefficients in Fig. 2. The expansion coefficients are not exact for the reasons given above, and we estimate the error in the relative expansion coefficients at about 15%. Excluding the samples on fused quartz and pyrex, the only parameter that has a significant systematic dependence on the expansion coefficients of the substrates is the Verwey transition temperature (the expansion coefficient and T_V for bulk Fe_3O_4 are also included in Fig. 2 for comparison). A comparison of the results on fused quartz, thermally oxidized silicon and AT-cut quartz--three different forms of SiO_2--shows no obvious dependence on the chemical composition of the substrates.

According to Samara, hydrostatic pressure reduces the transition temperature by about $0.5^{\circ}K$/kbar.[4] Since the transition on Corning 0211 glass is elevated by about $3^{\circ}K$, applying Samara's value gives an estimated tensile stress of about 6 kbar. The tensile stress on the sample can also be very crudely estimated by assuming that the films are un-

stressed at the processing temperature of about 400°C. Taking β as temperature independent, the difference in the total thermal expansion between magnetite and Corning 0211 glass at T_V is about 4×10^{-3}. Assuming a Young's modulus of infinity for the substrate and choosing 2×10^{12} dynes/cm^2 as a likely value for the magnetite film, the tensile stress produced by the mismatch is about 8 kbar. This agreement, which need not have been better than within a factor of ten, supports the validity of our interpretation.

When the mismatch is sufficiently large, as in the cases of fused quartz and pyrex substrates, there is apparently no conductivity transition. The reversibility of the measurements implies that this is not due to any detachment of the film from the substrate. However, the mismatch may be large enough to separate the grains of the polycrystalline films, reducing the conduction paths to small bridges between the grains. The resistance would then be dominated by the resistance of these bridges and the localized heating caused by the increased current densities would then inhibit the Verwey transition in the magnetite in these connecting links.

The effect of the sample thickness was investigated by varying the thickness of the magnetite films on Corning 0211 glass substrates. The results shown in Fig. 3 are also shown in Fig. 4 as the thickness dependence of the Verwey transition temperature, the change in the resistance at the transition, and the activation energies of the two phases. The activation energy of the cubic phase and the Verwey transition temperature

are both approximately independent of the film thickness while the resistance change at the transition and the activation energy of the low temperature phase both increase with the thickness of the film. The 700Å film shows no evidence of undergoing a conductivity transition down to below 115°K.

The thickness dependence of the resistance change and the low temperature activation energy can be explained on the basis of a model that assumes that part of the film remains in the cubic, high-conductivity phase at all temperatures. If a film of thickness D has a sublayer of thickness d that always remains in the high-conductivity phase, the resistance above the transition temperature will be

$$R_{\square} = \frac{(\text{Area})}{D \cdot \sigma_{\square}} \qquad \text{for } T > T_V$$

where $R_{\square}$ is the resistance and $\sigma_{\square}$ is the conductivity of the high temperature phase. When the thickness D is greater than the sublayer thickness d, a layer of thickness (D-d) goes into the low-conductivity phase at low temperatures while the sublayer remains in the high-conductivity phase. The total resistance will then be

$$R_{\diamond} = \frac{(\text{Area})}{(D-d) \cdot \sigma_{\diamond} + d \cdot \sigma_{\square}} \quad \text{for } T < T_V$$

where $\sigma_{\diamond}$ is the conductivity of the low temperature phase. The ratio of the measured resistances F is

$$F = \frac{R_{\Diamond}}{R_{\square}} = \left(\frac{D-d}{D} \cdot \frac{\sigma_{\Diamond}}{\sigma_{\square}} + \frac{d}{D}\right)^{-1} \quad .$$

When the majority of the current in the low temperature state is in the sublayer, i.e., for $\sigma_{\square}/\sigma_{\Diamond} >> D/d$, this resistance ratio can be approximated by

$$F = \frac{R_{\Diamond}}{R_{\square}} \approx \frac{D}{d} \quad .$$

When the thickness D is smaller than d, all of the film will stay in the high-conductivity phase and the ratio F will be unity, as observed in the 700Å sample.

The best fit of this model to the present data is shown as the solid line drawn in the top part of Fig. 4. If the model is correct, the results indicate that the thickness of the untransformed sublayer is about 600 - 1200Å. As shown in Fig. 2, for a fixed film thickness, F is apparently independent of the constraint imposed on the film by the substrate. This suggests that the sublayer is probably at the free surface of the sample. Although this model agrees with the present results, there exists no other evidence for its validity.

The samples used in this study had been exposed to the atmosphere at room temperature for periods ranging from a few hours to over a year. There is no apparent correlation between the exposure time and the measured value of F, implying that oxidation of the samples probably does not contribute to

the formation of this sublayer. In addition, Rutherford backscattering yields no evidence of any Fe_2O_3 formation on magnetite films of any age. Thus, it is not very probable that the untransformed layer consists of γ-Fe_2O_3, which is electrically, magnetically and crystallographically similar to cubic Fe_3O_4. X-ray diffractometry was used to eliminate the possibility of other phases such as FeO or any of the other forms of Fe_2O_3 as the material in this untransformed sublayer.

Measurements of the magnetic properties of some other magnetite films 460 - 7500Å thick were performed on a 60 Hz, 2.5 kOe peak field hysteresis loop tracer at room temperature. The results clearly indicate that the saturation magnetization is independent of the film thickness. This suggests that if there is an anomalous sublayer, it is Fe_3O_4 or γ-Fe_2O_3. The saturation magnetizations of these two oxides differ by less than 20%, so it is difficult to exclude the presence of γ-Fe_2O_3 by means of magnetometry.

Figures 2 and 4 show that the films have a slight thermal hysteresis in the Verwey transition of about 0.5°K. The measurements were made in steps of about 0.6°K and the temperatures were regulated to better than 0.1°K. The thermal hysteresis was present even after stablizing the sample temperature for up to ten minutes.

We have reported the first example of a Verwey transition at temperatures above the 119.4°K reported for bulk magnetite. The results show that the Verwey transition temperature is raised by the tensile stress produced by the

differences in the thermal expansion coefficients of the substrate and the magnetite film. The method used to raise the transition temperature provides further confirmation that the Verwey transition is of the Mott-Wigner type. The present measurements also show that the change in the sheet resistivity at the Verwey transition increases with the sample thickness, with no conductivity transition observed in a non-magnetic 700Å thick magnetite film. On this basis alone, we postulate the existence of a 600 - 1200Å layer that remains in the high-conductivity phase below the Verwey transition temperature. The substrate-independence of the resistance ratio suggests that if this anomalous high-conductivity layer exists, it is at the free surface of the sample.

We wish to thank C.H. Bajorek, IBM, Watson Research Center, for performing the hysteresis loop tracer measurements.

REFERENCES

1. L.R. Bickford, Rev. Mod. Phys. 25, 75 (1953).
2. E.J.W. Verwey, P.W. Haaijman and F.C. Romeijn, J. Chem. Phys. 15, 181 (1947).
3. J.H. Epstein, thesis, MIT (1954).
4. G.A. Samara, Phys. Rev. Lett. 21, 795 (1968).
5. J.S.-Y. Feng, C.H. Bajorek and M-A. Nicolet, IEEE Trans. Magnetics MAG-8, 277 (1972).
6. H.R. Bilger and M-A. Nicolet, Rev. Sci. Inst. 41, 346 (1970).
7. L.J. van der Pauw, Philips Res. Repts. 13, 1 (1958).
8. L. Néel, J. Phys. Radium 12, 258 (1951).
9. J.M. Lavine, Phys. Rev. 114, 482 (1959).
10. B.A. Calhoun, Phys. Rev. 94, 1577 (1954).

FIGURE CAPTIONS

Fig. 1 Sheet resistivity versus temperature for 4700Å Fe_3O_4 on various substrates. The procedure used to determine the transition temperature (T_V), the projected resistance ratio at the transition (F), and the activation energies (E_A) are illustrated for the sample on MgO. The transition temperatures are indicated by the vertical dashed lines, with the bulk T_V included for comparison. A thermal hysteresis of 0.5 - 1.0°K is present in all samples in which the Verwey transistion was observed. No evidence of either a Verwey transition or thermal hysteresis was observed on fused quartz or pyrex substrates.

Fig. 2 Substrate effects. The projected resistance ratio (F), (see Fig. 1), the activation energies (E_A) of the cubic (high temperature) and orthorhombic (low temperature) phases and the Verwey transition temperature have been plotted as a function of the estimated substrate expansion coefficient, with the estimated errors shown on the measurements made on the MgO substrate. The expansion coefficient and T_V for bulk magnetite are also shown for comparison. The lines drawn for E_A and F are linear least-squares fits, with the data from the pyrex and fused quartz substrates excluded from the calculation. These dependences are not statistically significant. The

linear fit to T_V is estimated.

Fig. 3 Thickness effects. The procedure for determining T_V, F and E_A are shown for the 5660Å sample on Corning 0211 glass (see the caption for Fig. 1). The vertical dashed lines indicate the transition temperature of the sample. No evidence of a Verwey transition was observed in a 725Å film.

Fig. 4 Thickness dependence. F, E_A and T_V are shown as a function of the film thickness, with the estimated errors shown of the results from the 5660Å sample. The thickness dependence of the low-temperature activation energy and F are believed to be significant. The lines are linear least-squares fits, with the line for F forced to intersect the origin (see text).

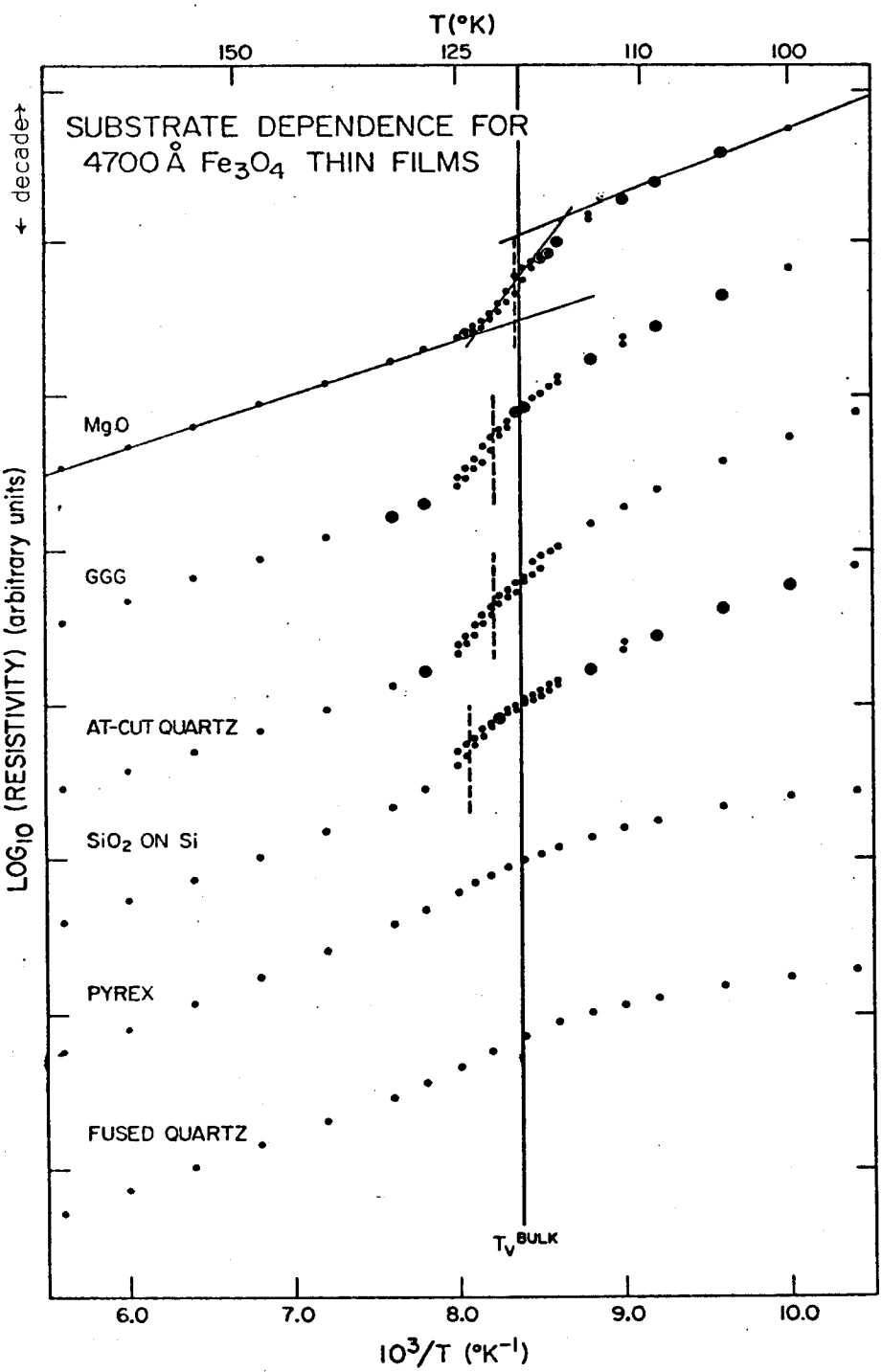

Feng + Nicolet
Figure 1

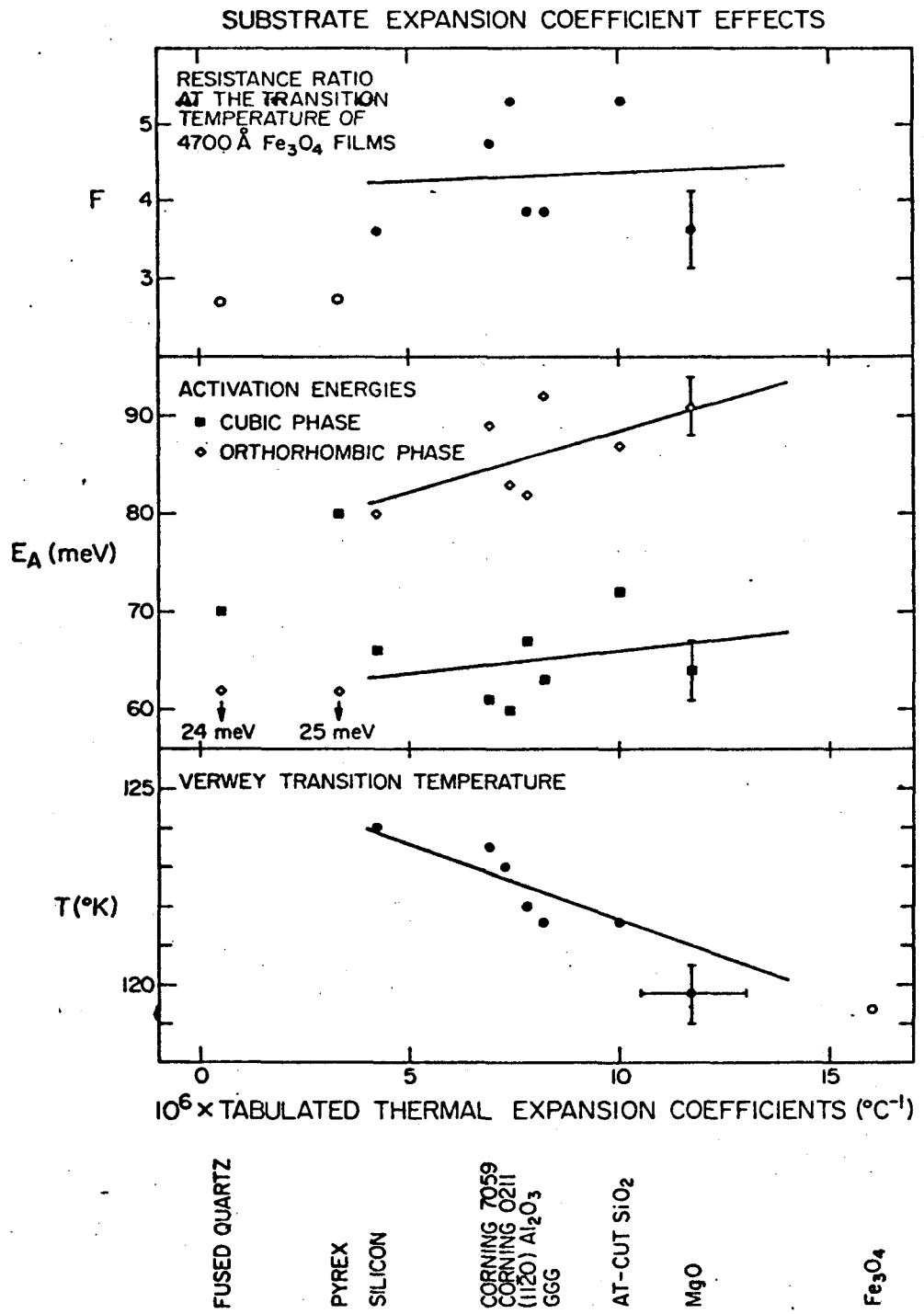

Feng + Nicolet

Figure 2

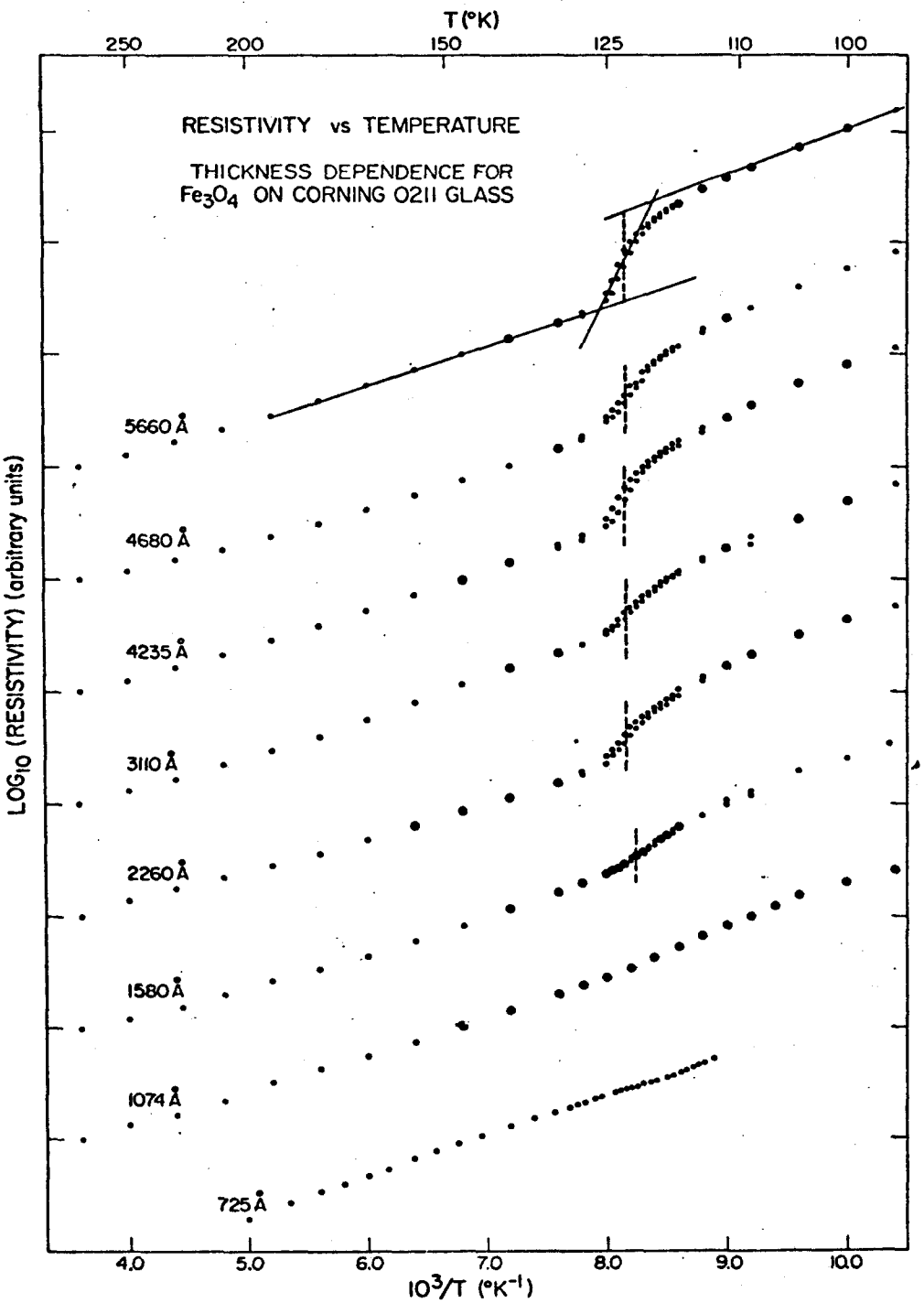

Feng + Nicolet
Figure 3

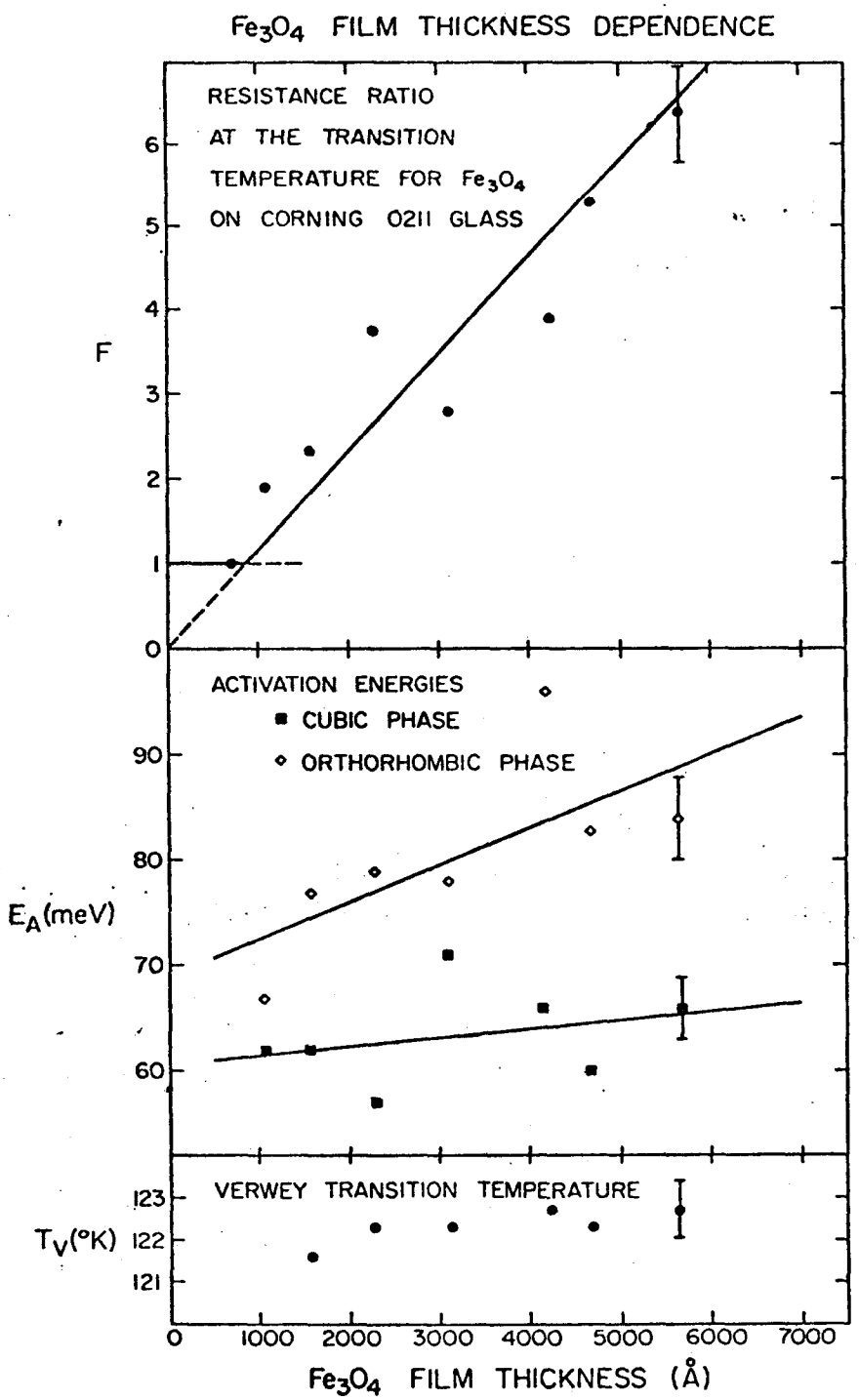

Feng + Nicolet
Figure 4

4.3 Additional Discussion

In the model for the present measurements, it is suggested that the resistivity change at the Verwey transition is proportional to the thickness of the film. Of course, when the film thickness is large enough to make the sheet resistivity of the low-conductivity layer comparable to the sheet resistivity of the anomalous surface layer, the approximations used to predict this linear dependence are no longer valid. In thick samples, the resistivity ratio should asymptotically approach the bulk value. We are unable to observe this because the process used for manufacturing the samples is not suitable for making films thicker than 1 μm.

If this anomalous layer does exist, it is not surprising that its existence has not been previously reported. In almost any measurement on bulk magnetite, the effect of an anomalous 1000 Å surface layer would be negligible compared to the changes in the rest of the sample. In addition, detection of this anomalous layer by x-ray diffractometry, neutron diffractometry, nuclear magnetic resonance or Mössbauer spectroscopy would be very difficult because of the very small amount of sample material that would be available for these measurements. Furthermore, this anomalous layer may not really exist. The present experiment is the only one which has even suggested that the magnetite surface does not experience the same Verwey transition as the bulk.

Since the mean free path of the conduction electrons is estimated to be about 5-10 Å, it is also not very plausible that this apparent anomalous layer is a fiction of the surface scattering of the conduction electrons. This short range nature of the conduction electrons also

implies that, if this anomalous layer does exist, it is probably due to some macroscopic phenomena that may be associated with its mechanical properties.

To the best of our knowledge, only one other experimenter has reported in the open literature of using our manufacturing process (Muret, 1974). Although he did not report in detail on the temperature dependence of the resistivity(his measurements concentrated on the optical transmission and absorption properties of the films), he does suggest that his cursory examination of the resistivity behavior gives results similar to ours.

The reader is cautioned that some of the results presented here depend on the judgment of the experimenter in analyzing the data. In particular, the determination of the activation energy of the low temperature phase requires estimating a straight line fit to data points that have a significant systematic curvature, and the criterion selected for making this estimate is crucial to the absolute value of the measured activation energy. However, it is believed that these have been done in a sufficiently consistent manner to justify the observed expansion coefficient dependence in the Verwey transition temperature. Although there is an apparent substrate dependence in the activation energies of the two states, it is not believed that the present data reveal any statistically significant dependence.

ADDITIONAL REFERENCES

Chapter 4

J. H. Epstein, 1954, thesis, Laboratory for Insulation Research, Massachusetts Institute of Technology(unpublished).

D. Kostopoulos and A. Theodossiou, 1970, phys. stat. sol. (a), vol. 2, p. 73.

P. Muret, 1974, Solid State Communications, vol. 14, p. 1119.

G. A. Samara, 1968, Physcial Review Letters, vol. 21, p. 795.

E. J. W. Verwey and P. W. Haayman, 1941, Physica(Utrecht), vol. 8, p. 979.

P. Weiss, 1896, thesis, Paris(unpublished).

Chapter 5

SUMMARY

We have reported on a method for manufacturing sub-micron films of Fe_3O_4 and we have performed detailed investigations into the dc galvanomagnetic properties of these films. The comparison of the properties of these films with the reported bulk properties has, in general, confirmed the identity of these films as magnetite.

The manufacturing process does not have any critical steps in the procedure and it can be readily modified to produce other ferrites over a modest composition range. The films are of interest because they have potential applications as high density data storage media and because the other processes that had been previously described almost invariably produce films with a high α-Fe_2O_3 content. The magnetic properties of these films do not differ significantly from the projections from the bulk magnetic properties.

The galvanomagnetic measurements probably only add to the confusion in trying to identify the more reliable of the reported measurements. In general, the temperature and magnetic field dependences reported by the various investigators do not agree either qualitatively or quantitatively. In our measurements, the observed qualitative behavior better approximates the expected behavior than some of those previously reported. However, the values found in these measurements sometimes differ significantly from the expected values.

The present measurements revealed, for the first time, a $\rho^{1/3}$ dependence for the extraordinary Hall coefficient in the cubic phase.

A careful re-examination of the previously published results confirmed the existence of this dependence in bulk magnetite and suggests that this is the asymptotic behavior for other ferrites.

Two unusual results of these measurements were the elevated Verwey transition temperature in these films and the smaller change in the conductivity at the transition. This motivated a detailed investigation into the effects of the thin film geometry on the Verwey transition. These showed that the elevated transition temperature was due to stresses on the film produced by the substrate. An interesting, and as yet unconfirmed, result of these measurements is that there may be a thin surface layer in these films that remains in the high-conductivity phase even below the Verwey transition temperature. If this layer does exist in our samples, it is probably also present on bulk magnetite.

It is sometimes said that brevity is the soul of wit.

It therefore follows...